

The University of Maine

DigitalCommons@UMaine

---

Electronic Theses and Dissertations

Fogler Library

---

Spring 5-2020

# Leak Detection and Localization in Pressurized Space Structures Using Bayesian Inference: Theory and Practice

Joel Castro  
joel.castro@maine.edu

Follow this and additional works at: <https://digitalcommons.library.umaine.edu/etd>



Part of the [Other Electrical and Computer Engineering Commons](#)

---

## Recommended Citation

Castro, Joel, "Leak Detection and Localization in Pressurized Space Structures Using Bayesian Inference: Theory and Practice" (2020). *Electronic Theses and Dissertations*. 3179.  
<https://digitalcommons.library.umaine.edu/etd/3179>

This Open-Access Thesis is brought to you for free and open access by DigitalCommons@UMaine. It has been accepted for inclusion in Electronic Theses and Dissertations by an authorized administrator of DigitalCommons@UMaine. For more information, please contact [um.library.technical.services@maine.edu](mailto:um.library.technical.services@maine.edu).

**LEAK DETECTION AND LOCALIZATION IN PRESSURIZED SPACE  
STRUCTURES USING BAYESIAN INFERENCE: THEORY AND  
PRACTICE**

By

Joel Matthew Castro

B.S. University of Maine, 2011

M.S. University of Maine, 2013

A DISSERTATION

Submitted in Partial Fulfillment of the

Requirements for the Degree of

Doctor of Philosophy

(in Electrical and Computer Engineering)

The Graduate School

The University of Maine

May 2020

Advisory Committee:

Dr. Ali Abedi, Professor of Electrical & Computer Engineering, Committee Chair

Dr. John Vetelino, Professor of Electrical & Computer Engineering

Dr. Mohamad Musavi, Professor of Electrical & Computer Engineering

Dr. Richard Eason, Associate Professor of Electrical & Computer Engineering

Dr. Silvia Nittel, Associate Professor of Spatial Informatics

© Joel Castro 2020  
All Rights Reserved

# **LEAK DETECTION AND LOCALIZATION IN PRESSURIZED SPACE STRUCTURES USING BAYESIAN INFERENCE: THEORY AND PRACTICE**

By Joel Matthew Castro

Dissertation Advisor: Dr. Ali Abedi

An Abstract of the Dissertation Presented  
in Partial Fulfillment of the Requirements for the  
Degree of Doctor of Philosophy  
(in Electrical and Computer Engineering)  
May 2020

Impact from micrometeoroids and orbital debris (MMOD) can cause severe damage to space vehicles. The crew habitat can begin to leak precious oxygen, critical systems can be punctured causing fatal failures, and an accumulation of impacts by MMOD can decrease the lifetime of any and all devices in space. Due to these and other potential dangers, MMODs have been considered the third largest threat to spacecraft after launch and re-entry. Many satellites and other spacecraft face this very problem inherent in all space travel on a daily basis, but often times they can be repaired. A major hurdle is to first be able to identify the presence of a leak. Many times an impact and subsequent leak is not discovered until it has caused a problem. A complete system is needed to detect and localize the impact to improve longevity of the habitat or other pressurized space structures.

In this work, a system for detection and localization of air leaks using air-borne acoustic waves is proposed. The system uses microelectromechanical systems (MEMS) microphone sensors to detect and record high frequency noise in an environment, angle of arrival (AOA) calculations to estimate possible leak locations, and a Bayesian tree-search filter to detect and more accurately localize a leak. This work includes proof of concept,



simulations, and physical prototypes as steps to creation of a complete system. Data from deployed flight test using said prototypes are analyzed. Modeling the effects of environmental reflections on the accuracy of localization is also studied.

## DEDICATION

In memoriam of my grandfathers:

**Mr. Armando Rodriguez** (1932-2012)

&

**Mr. Elliot Castro** (1939-2015)

For instilling the value of hard work and planting the seeds of interest in electronics.

## ACKNOWLEDGEMENTS

First and foremost, I'd like to express my deepest gratitude to my advisor and mentor, Dr. Ali Abedi. His continuous guidance, encouragement, and support were invaluable in my academic career, and his more than generous patience is the major reason I was able to complete this work. I'd also like to thank my advisory committee for their insight and suggestions over the years.

I also need to acknowledge members of the WiSe-Net lab that contributed to this work. Firstly, Dr. Hossein Roufarshbaf's experience in tracking and state estimation was essential in the early stages of this work. I must also thank Mr. Casey Clark for taking the lead in the construction and flight-readiness testing of the deployed prototypes as well as Dr. Lonnie Labonte for assisting in the endeavor.

I'd also like to thank other members of the lab, past and present, for their support and occasional needed distraction. Last but not least, I'd like to thank my family and friends: my parents, Steven and Sharon Castro, for their patience and education; my sisters, Angelina and Ileana, for their concern and support; and my friends, Joseph, Harold, Melissa, and everyone else for believing in me.

## TABLE OF CONTENTS

DEDICATION .....	iii
ACKNOWLEDGEMENTS .....	iv
LIST OF TABLES .....	ix
LIST OF FIGURES .....	x
LIST OF ACRONYMS .....	xiv
1. INTRODUCTION .....	1
1.1 Background .....	1
1.2 Literature Review .....	4
1.2.1 Leak Detection Methods .....	4
1.2.2 Localization Methods .....	6
1.3 Thesis Organization .....	9
1.4 Summary of Contributions .....	10
2. LEAK DETECTION USING BAYESIAN INFERENCE .....	12
2.1 Background .....	12
2.1.1 Problem Definition .....	12
2.1.2 Source Approximation .....	14

2.2	The Proposed Leak Detection Method .....	16
2.2.1	Reverse Beamforming .....	16
2.2.2	Tree Search.....	17
2.2.2.1	Path Metric.....	18
2.2.2.2	Detection .....	23
2.3	Experimental Setup.....	25
2.3.1	Sensor Array .....	25
2.3.2	Simulated Leak Source .....	26
2.3.3	Data Acquisition.....	28
2.4	Laboratory Setup .....	28
2.4.1	Simulations.....	29
2.5	Experiments.....	35
2.6	Summary of Contributions .....	36
3.	INTERNATIONAL SPACE STATION PAYLOAD .....	39
3.1	Sensor Array .....	40
3.2	Data Collection .....	41
3.2.1	Analog to Digital Converter .....	42
3.2.2	Processing Unit .....	42
3.3	Assembly .....	43
3.4	Laboratory Testing .....	44
3.5	Prototype Results.....	47
3.6	Field Test at JSC Mock ISS Module .....	47

3.7	ISS Testing and Analysis .....	49
3.7.1	ISS Test Setup .....	51
3.7.1.1	Deployment Locations .....	51
3.7.1.2	Test Setup .....	51
3.7.2	Data Analysis .....	53
3.7.2.1	Localization Results .....	53
3.7.3	Frequency Analysis .....	55
3.8	Summary of Contribution .....	58
4.	REFLECTION SIMULATION .....	63
4.1	Simulation Method .....	65
4.1.1	Path Finding .....	68
4.2	Spatial Simulation .....	69
4.2.1	Spatial Simulation Results .....	69
4.3	SNR Sensitivity .....	72
4.3.1	SNR Sensitivity Results .....	72
4.4	Reflection Coefficient .....	74
4.4.1	Reflection Coefficient Results .....	74
4.5	Reflection Analysis Conclusions .....	76
5.	CONCLUSION AND FUTURE WORK .....	79
5.1	Conclusions .....	79
5.2	Future Work .....	81
	REFERENCES .....	83

APPENDIX A – DERIVATION OF FORMAL DEFINITION .....	90
A.1 Attenuation Factor .....	91
APPENDIX B – PATHFINDING ALGORITHM .....	92
BIOGRAPHY OF THE AUTHOR .....	95

## LIST OF TABLES

Table 2.1	Comparison of the two ultrasonic components used in experiments. ....	26
Table 3.1	Measured accuracy of prototype during lab based testing. ....	48
Table 3.2	ACT deployment of Payloads. ....	53



## LIST OF FIGURES

Figure 1.1	Damage to multi-layer insulation of the Zarya module from an MMOD object in 2007 .....	2
Figure 1.2	Chart showing the number of debris particles being catalogued in orbit .....	2
Figure 1.3	Severe damage to radiator of the Endeavour (STS-118) .....	3
Figure 1.4	Source of 2018 leak located on the orbital compartment of the Soyuz MS-09 and created by a drill.....	4
Figure 1.5	Inflatable lunar habitat model at University of Maine. ....	7
Figure 2.1	Setup for determining the angle of arrival also known as the bearing angle. ....	14
Figure 2.2	An example of partial tree-search technique for one dimensional source localization is presented .....	19
Figure 2.3	The linear array of four MEMS ultrasonic sensors used for leak detection.....	26
Figure 2.4	Prototype of a circular array of ultrasonic transducers. ....	27
Figure 2.5	Tektronix MSO2014 oscilloscope used for more detailed data acquisition. ....	29
Figure 2.6	Generalized setup for experiments. ....	30
Figure 2.7	Completed setup for the data that was acquired .....	30

Figure 2.8	A realization of the simulated scenario; the true source location, the estimated source location using the proposed tree-search, and observations including contacts and false alarms from four sensor scans. ....	32
Figure 2.9	Effect of the false alarm rate on root mean square error (RMSE) of the estimated source location. ....	33
Figure 2.10	Effect of observation noise on root mean square error (RMSE) of the estimated source location. ....	34
Figure 2.11	Performance comparison of the proposed techniques with different probability of target detection and comparison with the particle filtering technique. ....	35
Figure 2.12	Comparing results from lab experiments with that of the simulated algorithm. ....	37
Figure 3.1	An exploded view of the ISS as of 2019.....	39
Figure 3.2	Block diagram of the WLD system.....	41
Figure 3.3	Deployed setup of ultrasonic sensor arrays.....	42
Figure 3.4	Schematic for bandpass filtering and amplification.....	43
Figure 3.5	Custom designed and printed enclosure.....	44
Figure 3.6	Custom designed PCB.....	45
Figure 3.7	Area of interest for testing deployed design.....	45
Figure 3.8	Custom pseudo-anechoic chamber used in testing.....	46
Figure 3.9	PSD of 40 kHz signal and ambient noise with and without anechoic chamber .....	46

Figure 3.10	Lab-test results with leak source at .25 x .25 m. ....	47
Figure 3.11	Error of Kalman filter and tree-search versus source distance.....	48
Figure 3.12	Power spectral density of received signal in mockups .....	49
Figure 3.13	Comparison of filtered and unfiltered received signals with source present.....	50
Figure 3.14	HTV-6 a.k.a. Kounotori 6 released from the ISS.....	50
Figure 3.15	Payload deployed on Node 1 Zenith Airlock footbridge.....	52
Figure 3.16	Payload deployed on Node 1 Nadir Airlock footbridge.....	52
Figure 3.17	Payload deployed on Node 2 Nadir Columbus footbridge.....	52
Figure 3.18	Raw guesses and calculated estimates for Node 1 Nadir location. ....	54
Figure 3.19	Raw guesses and calculated estimates for Node 2 Nadir location. ....	55
Figure 3.20	Raw guesses and calculated estimates for Test 1 at Node 1 Zenith location. ....	56
Figure 3.21	Raw guesses and calculated estimates for Test 2 at Node 1 Zenith location. ....	57
Figure 3.22	PSD of raw data for Box1 during ACT1 representative of both functioning boxes and tests. ....	59
Figure 3.23	Average PSD across runs using data from Box1 during ACT1. ....	60
Figure 3.24	Zoomed 40 kHz focus of filtered data from Box1 during ACT1. ....	60
Figure 3.25	Comparison of filtered PSD between data from Box1 during ACT1 and relative mockup location. ....	61
Figure 3.26	Spectrogram from surface-borne acoustic analysis.....	61

Figure 3.27	Spectrogram of the air-borne acoustics from ACT 1 and ACT 2.....	62
Figure 4.1	Example reflection scenario. ....	63
Figure 4.2	Sample setup for reflection simulations.....	66
Figure 4.3	Brief overview of the processes used in the simulation method.....	67
Figure 4.4	AOA error in area of interest for surface distance of 0.1 m. ....	70
Figure 4.5	AOA error in area of interest for surface distance of 1.5 m. ....	70
Figure 4.6	AOA error in area of interest for surface distance of 3.0 m. ....	71
Figure 4.7	AOA error over threshold across surface distances. ....	71
Figure 4.8	Rate of exceeding threshold relative to SNR without a reflecting surface. ....	73
Figure 4.9	Rate of exceeding threshold relative to SNR with a surface reflection coefficient of 1. ....	73
Figure 4.10	Rate of exceeding threshold relative to the reflection coefficient. ....	74
Figure 4.11	Error rate for single simulation with equal magnitude and variable phase.....	75
Figure 4.12	Standard deviation of error rate relative to the phase shift component of reflection coefficient. ....	76
Figure 4.13	Rate of exceeding threshold relative to the reflection coefficient magnitude. ....	77
Figure B.1	Example reflection scenario with labels. ....	92

## LIST OF ACRONYMS

<b>AE</b>	acoustic emission
<b>AOA</b>	angle of arrival
<b>AWGN</b>	additive white Guassian noise
<b>EVT</b>	extreme value theory
<b>GEO</b>	geosynchronous equatorial orbit
<b>IR</b>	infrared
<b>ISS</b>	International Space Station
<b>LEO</b>	low earth orbit
<b>LOS</b>	line of sight
<b>MAP</b>	maximum a posteriori
<b>MEMS</b>	microelectromechanical systems
<b>MMOD</b>	micrometeoroids and orbital debris
<b>PCB</b>	printed circuit board
<b>PDF</b>	probability density function
<b>PSD</b>	power spectral density
<b>PZT</b>	lead zirconate titanate
<b>RMSE</b>	root mean square error
<b>RSS</b>	received signal strength

**SNR**    signal to noise ratio

**STDEV**   standard deviation

**TDOA**   time difference of arrival

**TOA**    time of arrival

**WLD**    Wireless Leak Detector

# CHAPTER 1

## INTRODUCTION

### 1.1 Background

The danger of MMOD is very real both in low earth orbit and beyond. Hypervelocity impacts can very easily damage and penetrate commonly used materials in space vehicles. This is true even for some of the smallest objects (see Figure 1.1). The sheer number of cataloged objects in orbit around Earth is almost 20,000 as of January 2020 as seen in Figure 1.2. Of this large number of objects recorded, over half consist of object 10 cm in size or larger [2, 5]. There is an even larger quantity of debris that may be smaller but can still deal a significant amount of damage. A major increase in this number occurred with two collisions in 2007 and 2009 increasing the fragmentation debris count by 50%. Orbiting around the earth, the International Space Station (ISS) and other satellites are at risk of collisions with debris that reach altitudes of low earth orbit (LEO) or geosynchronous equatorial orbit (GEO). Even when leaving orbit for other space missions, this large collection of debris must be taken under consideration. On top of the orbital debris, micrometeoroids entering the vicinity of Earth can be extremely difficult to detect and avoid especially and are even more so when traveling beyond GEO.

Every impact on a pressurized structure from MMOD has the potential to puncture the shielding and create a leak. When a leak actually occurs, it can take a significant amount of time to find it, especially for small leaks due to environmental factors such as noise and reflections [10]. A leak between modules of the Mir space station was detected in October of 1999 but was not repaired until April 2000 due largely to the amount of time it took to find the leak [6]. Air continued to leak throughout the duration of the search and repair. Another serious matter was the damage to a radiator in the Endeavour shuttle seen in Fig 1.3. The damage to the cooling system would have caused an immediate return if the

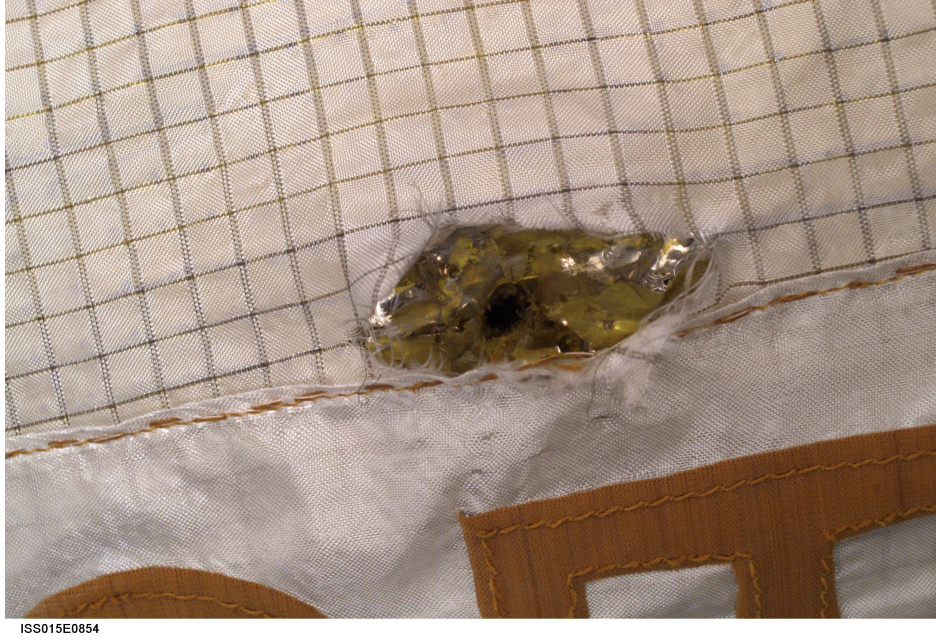


Figure 1.1. Damage to multi-layer insulation of the Zarya module from an MMOD object in 2007 [7].

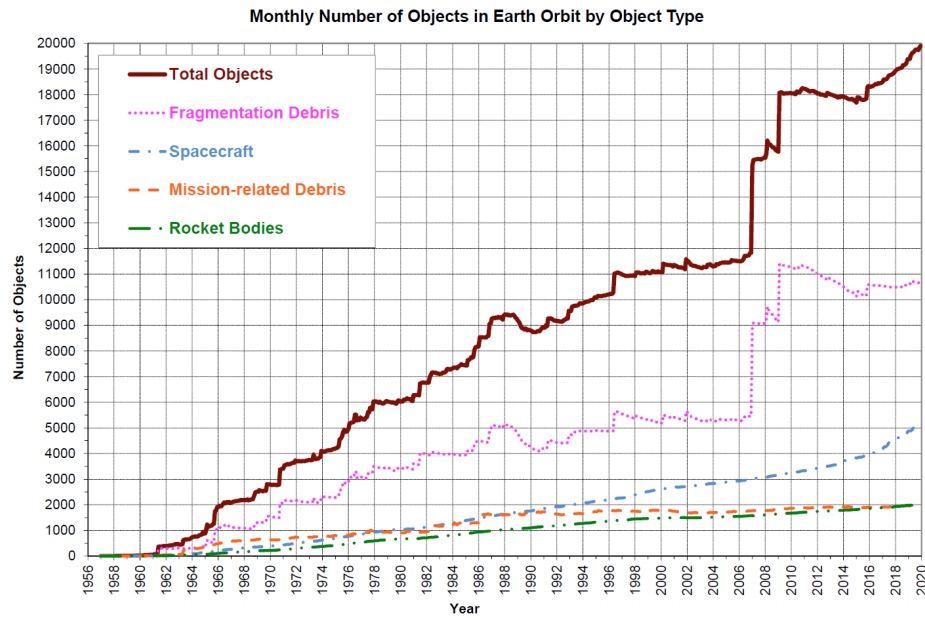


Figure 1.2. Chart showing the number of debris particles being catalogued in orbit [5].

impact had been in at a more critical component of the system [1]. Most recently in August 2018, a small pressure leak was detected and localized to the Soyuz spacecraft



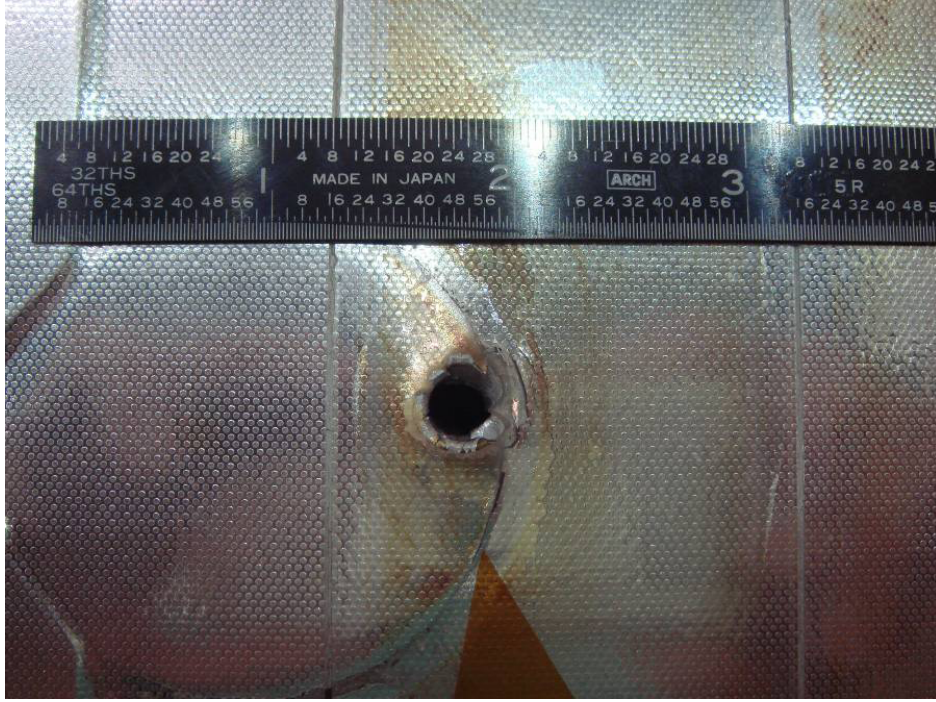


Figure 1.3. Severe damage to radiator of the Endeavour (STS-118) [3].

attached to the Rassvet Module. While the leak, caused by a hole of about 2 mm in diameter presented in Figure 1.4, was originally thought to be created by an MMOD impact, it has since been reported as man-made by means of a drill [8, 9]. Among the methods used to localize leaks after detection (currently through monitoring pressure) is listening for audible sound and using handheld ultrasonic detectors such as the ULD kit developed by CTRL Systems. This device simply serves as a narrowband filter for the 40 KHz region that produces an audible representation of the level of ultrasonic sound [28]. While these methods have worked in the past, there is a clear need for faster, reliable, and more accurate systems particularly in the case of inflatable structures, where the structural health is strongly affected by the presence of a leak.



Figure 1.4. Source of 2018 leak located on the orbital compartment of the Soyuz MS-09 and created by a drill [8].

## 1.2 Literature Review

### 1.2.1 Leak Detection Methods

Most research presented on leak detection makes use of ultrasonic acoustics. The most pervasive methods for this kind of detection in the past have been acoustic emission (AE), active ultrasonics or pulse-echo techniques, and vibro-acoustics. AE based methods include both surface-borne and air-borne ultrasonic acoustics. Vibro-acoustic leak detection is comprised of inducing a "swept sine excitation" in the audible acoustic spectrum and monitoring the ultrasonic response near locations prone to leaks such as seals. Detection is usually with microphones on or near the surface. Pulse-echo or pulse-receiver techniques use an active ultrasonic emitter inside of a structure and while a microphone scans across the exterior, primarily seals. This method may be applicable in normal conditions such as during manufacturing but can not be deployed in an extreme environment. Passive ultrasonic methods detect similarly, but as the name suggests does not generate the signal; rather, microphones listen for the natural noise generated by a

leak. Most means of detection using this method are hand-held devices that require users to traverse an area of interest and listen for leaks [11].

Surface borne AE methods use the material perturbation in the form of Lamb waves caused by leaks to localize leaks. Holland et al. use a set of 64 measurement points on a single disc of lead zirconate titanate (PZT) attached to a printed circuit board (PCB) for recording signals of surface vibrations. Cross-correlation and spatial Fourier transforms are used to determine vectors pointing from the array towards the source which in turn are used to triangulate the leak [16, 17]. It should be noted that according to Holland et al., "For a leak into a vacuum, this sound can propagate neither in the vacuum nor back up the Mach 1 free jet into the spacecraft, and therefore cannot be detected," [16]. This was later amended as "downstream leak dissipates into the vacuum of space, leading almost no leak noise inside the spacecraft pressure vessel" [17]. While leak noise inside the pressurized vehicle may be significantly lower than if in an atmosphere, the lack of direct contact with the surface may make installation and mobile use more viable.

More research has been done in other uncommon methods of leak detection and localization for use on the ISS. These methods include pressure change monitoring, optical observation, infrared (IR) imaging, and attitude sensing. Pressure change methods tend to be similar to what is currently implemented, in that drops of pressure measured by gauges are used as determination that a leak exists. MEMS Sensors used to monitor pressure change have been created and tested but were not available for the range and sensitivity desired for space use. While this is one of if not the most common method for detection, it offers little in the way of localization and not much research is underway. Optical observations encompasses the use of video or human observation to detect the presence of leaking fluorescent gases; the source of which can be localized in a straightforward matter. Though simple and promising environmental factors seemed to make detection impossible as no in-orbit test has been successful. Infrared testing uses IR lasers to scan areas either illuminating the gas for optical observation or observing the thermal emission. This has

been shown to be possible on the ground but requires new testing and device to detect the lost gases from a pressurized space vehicle. As an added detriment, it has not been proven possible to do so in a vacuum environment with gases coming from atmospheric pressure. Attitude sensing allows the onboard systems used to detect the minute movement behavior of the vehicle to also detect possible leaks. This is due to leaks acting like miniature thrusters and the basic physics principle of Newton’s third law. The difficulty lies in the need for extremely accurate and detailed knowledge of the vehicles layout and mass distribution which may be consistently changing [10].

More details on optical means using IR lasers can be seen in [21, 22], ultrasonic waves via AE in [20, 26, 12, 27], and dynamic pressure in [23, 24, 25]. A more recent attempt at ultrasonic leak detection can be seen in [13] where 2D localization uses a random array of ultrasonic microphones but uses a dictionary-like storage system of expected leaks to generate acoustic images of directional energy concentration. While the approach is of interest the use of likely leak locations is not applicable to MMOD impacts and other sources of random leak locations. Another recent work uses received signal strength (received signal strength (RSS)) and robotics to directional filter and scan a 2D area for noise generated by air leaks [14]. Both of these works currently assume higher signal to noise ratio (signal to noise ratio (SNR)) than can be expected in scenarios of small leaks. This work will focus on the use of air-borne ultrasonic sources using cross-correlation and angle of arrival (AOA) to generate estimates of source location in a 2D space.

### **1.2.2 Localization Methods**

Leak detection and localization with applications for structural health monitoring in aerospace and energy industries can be considered a general source detection and localization problem [20]. The generalized source detection and localization problem appears in broader engineering fields including wireless communication systems and target tracking [30, 31, 32]. Space structures and spacecrafts often face impacts from MMOD and



Figure 1.5. Inflatable lunar habitat model at University of Maine.

require localizing the impacts and checking for possible cracks and leaks. As inflatable space habitat concepts such as that seen in Figure 1.5 are being further developed, leak detection and localization become an integrated part of the design process requiring serious attention. However, low power level leak signals, non-linear relation of the sensor observation space and the leak state space, and possibly non-Gaussian observation noise are some of the challenges in source detection and localization problem.

The focus of this work is on automatic leak detection and localization in deployable pressurized space structures using surface-borne emitted ultrasonic signals in noisy or low power environments. Sensed ultrasonic signals are generally examined for the RSS and the AOA at the receivers, sensor arrays being the most common receiver [30]. In detecting small cracks and leaks [10], however, power of the leak signal is low and may not be detected for several time instances. Therefore, the receivers are unable to distinguish between a true leak signal and a false observation due to the relatively high level of background noise. Ultrasonic signals are also prone to reflections from other surfaces of the structure causing interference at the receivers. Existing techniques for leak detection and

localization using surface-borne acoustic signals [27] are based on triangulation techniques [16, 17, 18]. None of these techniques consider the uncertain origin of the sensed ultrasonic signals in noisy environments. The approach described in this work is based on the Bayesian inference model in which the leak localization is performed by searching the maximum a posteriori distribution function of the leak location (maximum a posteriori (MAP) criteria) through a tree-search structure. Although MAP algorithms have been used in other applications, utilizing one in the context of leak detection is novel.

The Bayesian filter in this model provides a general solution based on the MAP criteria [33]. For a linear-Gaussian state space model, the closed form solution of the Bayesian filter is found through the Kalman filter [35]. Due to computational efficiency of the Kalman filter, many algorithms have been developed based on this algorithm for nonlinear state space models [36, 37, 38, 39, 40]. However, all these techniques assume that the posterior density function of the system state vector is Gaussian which in general is not true. Additionally, these techniques require initial estimation of the leak state vector which is a challenge for the sensed ultrasonic signals with uncertain origin in noisy environments. Other existing algorithms for general nonlinear and non-Gaussian system state space models [41, 42, 43] require high demand of computational complexity which limits the real time applications of these algorithms. Existing sub-optimum Bayesian techniques such as the Extended Kalman filter [24] and Particle filter [23] are being used by leak detectors using information from gas pressure sensors and are suitable for leak detection in pipeline structures. Recently, particle filtering [44] and partial tree-search [45, 46] have been developed to approximate the Bayesian filter in a complexity efficient way. Using particle filtering technique, the posterior probability density function (probability density function (PDF)) of the leak state vector is approximated using a set of discrete particles with their associated probabilities or weights. The expected value of the approximated posterior PDF is used as the leak state estimation. In the tree-search technique, instead of

approximating the posterior PDF of the leak state, the algorithm searches for the MAP solution through an efficient tree search structure.

In this work, a tree-search sub-optimum Bayesian technique is developed and evaluated as a novel solution for automatic leak detection and localization. The proposed technique implements information of the air-borne emitted ultrasonic signals and addresses the challenge of signal uncertainty in noisy environments, which extends applications of the algorithm in leak detection and localization for inflatable space structure. The developed tree-search technique searches for the MAP solution of the state space model in the areas of the posterior distribution with significant mass. The algorithm can be interpreted in a way that approximates the posterior PDF with a set of Gaussian kernels [47, 48] generated through a tree search structure. The solution to the problem is the Gaussian kernel which generates the largest associated metric (weight) among the other kernels. To reduce the computational complexity, the number of Gaussian kernels examined in the proposed algorithm will be adaptively changed with more kernels being examined in the vicinity of areas that are more likely to contain the leak.

### **1.3 Thesis Organization**

The remainder of the thesis proposal is organized as follows. In Chapter 2, the proposed tree-search technique for source localization and detection using beamforming is explained along with an overview of the testbed, simulation and experimental results. A deployable system implementing data collection and preliminary leak detection is discussed in Chapter 3 along with analysis of in situ data from ISS is reviewed. The latest work on analysis of reflection effects on AOA error is explored in Chapter 4. Finally a review and discussion of future work is briefly discussed in Chapter 5.

## 1.4 Summary of Contributions

A relatively fast tree-search algorithm for leak detection and localization based on Bayesian inference model and approximated solution through a tree-search structure was developed. This is done by taking an area of interest and dividing it into large cells. Cells with high likelihood of containing a source are divided into smaller cells expanding the tree. This is done until the desired estimation precision is obtained or the leak is classified as not present. Simulations were verified by an experimental setup.

H. Roufarshbaf, J. Castro and A. Abedi, "Stochastic modeling of leak detection and localization using ultrasonic sensor array," IEEE International Conference on Wireless for Space and Extreme Environments, Baltimore, MD, 2013, pp. 1-1.

The developed method was expanded upon to compare with other frequently used localization methods. Extensive data were collected using microphone sensor arrays detecting air-borne ultrasonic sources. Source estimates based on cross-correlation methods from each sensor array are used as observations for the model. The proposed method was found to be better performing with faster convergence and lower latency than the other simulated methods.

H. Roufarshbaf, J. Castro, F. Schwaner and A. Abedi, "Sub-optimum fast Bayesian techniques for joint leak detection and localisation," in IET Wireless Sensor Systems, vol. 3, no. 3, pp. 239-246, September 2013.

A physical prototype of the physical components of a leak detection and localization system was designed and built for testing on-board the International Space Station. It would be designed to record ultrasonic noise and calculate source estimates as described in previous works. These estimates as well as the raw data collected would be transmitted to ground for post-processing. Data collected would be post-processed for spectrum and temporal analysis as well as to provide a rudimentary background signature.

C. Clark, L. Labonte, J. Castro, A. Abedi and V. Caccese, "Wireless leak detection using airborne ultrasonics and a fast-Bayesian tree search algorithm with technology



demonstration on the ISS," 2015 IEEE International Conference on Wireless for Space and Extreme Environments (WiSEE), Orlando, FL, 2015, pp. 1-5.

A. Abedi, V. Caccese, J. Castro, C. Clark, L. Labonte, H. Roufarshbaf, "Wireless Leak Detector for International Space Station (WiLD-ISS)," ISS R&D Conference, Boston, MA, July 2015.

## CHAPTER 2

### LEAK DETECTION USING BAYESIAN INFERENCE

#### 2.1 Background

##### 2.1.1 Problem Definition

The problem of detection and localization of an ultrasonic source using the observational values from  $\mathcal{N}$  sensor node locations is considered in this thesis proposal. The problem is modeled as a state space model where the desired parameters are the source location coordinates. These parameters are expressed in the form of a vector in Cartesian (x,y) coordinates. Each sensor node is scanned and observational data is collected by a central processing unit.

This is essentially a state or parameter estimation problem where observations are used to estimate the state or parameters of the model with the goal of error less than the additive noise. Solution methods to this type of problem tend to take a probabilistic, or more precisely a Bayesian, approach with the assumptions that observations are dependent on the state/parameters and independent of the noise. This may also requires the assumption that parameters are constant as in parameter estimation, but the prior PDF of the state may be assumed depending on the method. Given a sufficiently large number of observations, the prior PDF will have little effect on the solution. While more observations yield more accurate results, it is not always possible to wait for this large number of observations. As new observations are collected for filtering, a need to update the estimated state leads to using a recursive filter. This requires the state-independent additive noise to be white or have each noise component of an observation be independent of noise components of other observations, i.e additive white Guassian noise (AWGN)[29].

For the notation, the subindex  $k$  denotes the sensor scan index (time index) and the superscript  $n$  denotes the sensor array index. That is,  $\mathbf{w}_n^k$  would represent the  $\mathbf{w}$  vector

from the  $k^{\text{th}}$  time index of the  $n^{\text{th}}$  sensor array. The variation of the source parameters during  $K$  scans of the sensor arrays is assumed to be relatively slow since the leak does not travel. Detection and localization of moving sources through tracking algorithms [33] is a problem that has been covered as well but is outside the scope of this work.

The source state vector is sensed by sensor array  $n$  with probability  $P_D^n$  according to the observation model

$$\mathbf{z}_k^n = \mathcal{H}^n(\mathbf{x}) + \mathbf{w}_k^n, \quad (2.1)$$

where  $\mathbf{z}_k^n$  is the sensed source signal,  $\mathcal{H}^n$  is the transfer function from the source state space to the observation space, and  $\mathbf{w}_k^n$  is the observation noise vector with known statistics.  $P_D^n$  is the probability of correct detection and is based on the SNR of the source signal and the detection threshold of the sensor node. With smaller leaks, the SNR will be very low, and the signal will be hard to distinguish from the noise. If the detection threshold is set to a lower value to detect these smaller leaks, there will be more false alarms. The method of detection based on the threshold will be discussed further in section 2.2.2.2.

False observations are assumed to be independent from other observations and are uniformly distributed in the search area. The number of false measurements are modeled with a Poisson distributed random variable with parameter  $N_F$  and probability distribution function  $\mu_F()$  based on the Poisson theorem. Accordingly, the parameter  $N_F = \zeta V$  where  $\zeta$  is the density of false observations per volume unit and  $V$  is the volume of the area of interest. In this work, the area of interest is considered to be on a 2 dimensional plane covering the surface area of potential leak locations. Considering the false measurements, the observation matrix of sensor array  $n$ ,  $\mathbf{Z}_k^n = [\mathbf{z}_{k,1}^n, \dots, \mathbf{z}_{k,m_k^n}^n]$ , is formed from possibly sensed true source observation and the false observation. The value  $m_k^n$  is defined as the total number of observations from sensor array  $n$  in scan index  $k$ . Observations from all  $N$  sensor arrays in scan index  $k$  are denoted by the observation set  $\mathcal{Z}_k = \{\mathbf{Z}_k^1, \dots, \mathbf{Z}_k^N\}$ .

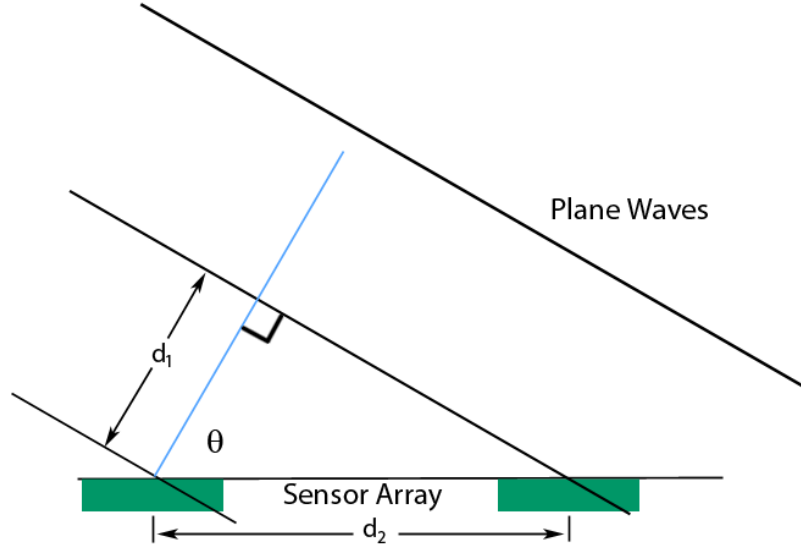


Figure 2.1. Setup for determining the angle of arrival also known as the bearing angle.

### 2.1.2 Source Approximation

In order for an algorithm to detect and localize leaks based on data collected using the setup is mentioned in 2.1.1, an approximation of the source must be made from each of the sensor arrays. There are several methods of practice for making these approximations as well as for taking these approximations and further focusing on the correct location. Detection is another key issue that can be determined from the sensor data before or after localization.

These are the most common means of approximating a source. The primary methods are RSS and AOA. The method of time difference of arrival (TDOA) using time of arrival (TOA) measurements is a common synchronized means of source localization. Each has benefits and drawbacks, but together are even more effective.

The process of finding the angle of arrival is to find the local TDOA among individual sensors of a single array. Given the time difference from one node and the known speed of the wave being detected, the extra distance the wave travels between to the second sensor node can be calculated. This distance is shown as  $d_2$  in Figure 2.1. It should be noted that

this calculation assumes the receiving sensors are far enough from the source that the incoming waves can be approximated as a planar wave. The value of  $d_1$  is known and equivalent to the distance between the sensors. The distance  $d_2$  is defined as

$$d_2 = v_a * (\Delta t), \quad (2.2)$$

where  $\Delta t$  is the time delay between signals and  $v_a$  is the velocity of the wave. The general trigonometric property of cosine used to find the angle is

$$\theta = \cos^{-1}(adj/hyp). \quad (2.3)$$

Combining (2.2), (2.3), and (2.3) and replacing the *adj* and *hyp* with  $d_2$  and  $d_1$ , respectively, yields

$$\theta = \cos^{-1} \left( \frac{v_a(\Delta t)}{d_1} \right). \quad (2.4)$$

For this work, the decision to use AOA to localize leaks is a logical one. Using AOA to generate localization data only requires two sensor arrays to approximate the source location. This is done in a similar fashion to the RSS method; the point where the graphical representations overlap is used as the approximation for the source. The graphical representations for AOA is just a line from the sensor array at the angle of arrival or bearing angle. Any more nodes provides extra data to better approximate the source location and improve performance.

The main reason the RSS method is not the primary method of localization is the unknown leak characteristics. In the event of a small leak, one can assume low RSS values and vice versa. While closer leaks will yield higher RSS values this does not take into consideration the leak's physical properties which may skew RSS when there are relatively distant arrays or be hard to differentiate with closer sensor arrays. Since, there can be a wide range of leak sizes and other characteristics, the RSS alone is not reliable enough to localize. This does not mean this data is unusable. By possibly scaling the values, this

method of localization can be used to improve the performance of the current algorithm. It could also be used to determine the size or severity of the leak.

While TDOA/TOA methods are fairly common, they are not used to localize the leak from the sensor arrays. This is due to the need for synchronization. While not impossible, this would have added complexity and difficulty to the localization system developed. Since no synchronization is done, there is less radio communication resulting in lower traffic and longer battery life for future wireless nodes. While not as significant of a reason, it should be noted that accurate RSS methods would also require additional communication between multiple nodes for localization.

## **2.2 The Proposed Leak Detection Method**

In this section, the method used for finding a leak source is presented. This includes the means of processing ultrasonic signals to a source approximation and an explanation of the method developed for detecting and locating a leak from these source approximations. There is a brief introduction to beamforming and how it is used in the context of source approximation. The discussion of the tree search method for detection and localization will be a mathematical development of the method starting with localization.

### **2.2.1 Reverse Beamforming**

In order to find the time difference of arrival (TDOA) at an individual sensor array, reverse beamforming is used. Beamforming is a method of increasing the amplitude of a combined signal from two or more sources by shifting the phase of the otherwise identical signals. Without the shift(s), the signals from multiple sources are likely to be out of phase at arrival. Waves are additive in that the representation for two waves can simply be added to obtain the total signal. Due to the additive property, the amplitude at the receiving node is likely to be at a point where the amplitude is lowered. In order to solve this

problem, a phase shift is implemented to ensure that the signal is in phase and therefore greater in amplitude than a single signal at the receiver.

In order to utilize beamforming, it is necessary to know where the receiving node is; if the location is known the proper phase shift can be applied. This work uses the process in reverse[34]. In order to find the direction of arrival, the phase shift between adjacent sensors is calculated using cross-correlation and then used to derive the bearing angle as mentioned in 2.1.2.

### 2.2.2 Tree Search

Generally, a Bayesian filter is used as an approach for sequentially approximating the posterior distribution function of the source state vector given the sensor observations. The goal of the design is to find values of the source state vector which maximizes the posterior PDF of the state given the observations

$$\hat{\mathbf{x}} = \arg \max_{\mathbf{x}} p(\mathbf{x} | \mathcal{Z}_1, \dots, \mathcal{Z}_k). \quad (2.5)$$

For a general source state space model, where the closed form of the Bayesian filter does not exist, calculation of the posterior PDF over all possible target states increases the computational complexity. In this section, a complexity efficient tree search technique is demonstrated in which the MAP solution is approximated only in the regions of high likelihood through navigating a tree.

Instead of estimating the posterior function as in a Bayesian filter, the algorithm follows paths of a tree to search for local maxima of the posterior function. Knowledge of the local maxima can be used as an approximation of the actual function. To utilize a tree search structure, the state space must be discretized and an appropriate metric proportional to the posterior PDF (2.5) must be defined to compare among the solution candidates inside the tree. The algorithm will navigate the state-space and find these candidates in the form of a source state vector. The candidate with the largest metric represents the solution to the MAP estimator and the source state vector equivalent of the leak location.

The initial state of the source known as the root of the tree is selected from the expected value of the assumed prior PDF of the source state (i.e. uniformly distributed in the area of interest). In other words, the area of interest is initially considered as a large cell that may contain a source. Each node of the tree denotes a subset of the source state space (i.e. a partition of the original area). A path is defined as the sequence of the nodes starting from the root of the tree and ending at a final node. Associated with each path of the tree is a metric proportional to the posterior probability mass that the source state is inside the subsets presented by the nodes of the path. A path of the tree is extended only if the associated metric is greater than a predefined threshold. With each extension of a tree path, the subset presented by the ending node is spanned into smaller subsets; this narrows the search boundaries for a local maxima search of the posterior function. This procedure continues until the desired resolution of the source state estimation is achieved. In this stage, all paths with the metrics greater than the predefined threshold show existence of a source.

Figure 2.2 shows an example of a tree-search in the form of a one-dimensional state space. In each iteration, the area of interest is divided into three sections. Initially, we assume that the second and the third cells (from left to right) are the highly likely cells. Then, the algorithm starts dividing these large cells into smaller cells and calculates the path metric of newly generated cells. In this simple example, we assume that after three iterations, the desired accuracy is achieved.

### 2.2.2.1 Path Metric

As mentioned, the search for the source location by path extensions is based on the state metric. To approximate the MAP solution, the metric of an estimated state should be proportional to the posterior probability mass of the state. If we denote the estimated state of path  $l$  in the search tree by  $\mathbf{x}(l)$  and its associated discrete cell by  $\mathbf{u}(l)$ , then the



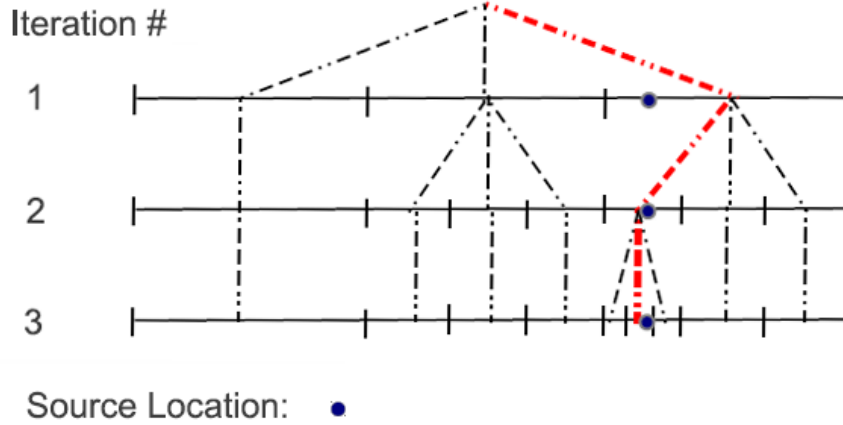


Figure 2.2. An example of partial tree-search technique for one dimensional source localization is presented [49].

state metric  $b(l)$  is defined by

$$\begin{aligned}
 b(l) &= p(\mathbf{x}(l) | \mathcal{Z}_1, \dots, \mathcal{Z}_K, \mathbf{u}(l)) \\
 &\propto p(\mathcal{Z}_1, \dots, \mathcal{Z}_K | \mathbf{x}(l), \mathbf{u}(l)) \\
 &= \prod_{k=1}^K p(\mathcal{Z}_k | \mathbf{x}(l), \mathbf{u}(l)).
 \end{aligned} \tag{2.6}$$

where the second line is derived by applying Bayes' theorem and dropping the common term  $p(\mathcal{Z}_1, \dots, \mathcal{Z}_K)$  from the denominator. For deriving the third line of (2.6), the observations of each receiver given the source state  $x(l)$  are assumed to be independent across different time scans. The observation set  $\mathcal{Z}_k$  may contain true observation of the source state vector and false observations.

Given the estimated source state  $x(l)$ , source generated observations across the receiving nodes are independent due to the assumed independence of the noise vector  $w_k^n$  (2.1) across the receiving nodes. False observations among different receivers, on the other hand, may not be independent since some of the false observations from different receivers may be generated from some common noise sources. For receiving nodes installed at far enough distances, it is reasonable to assume that the false observation across the receiving

nodes are also independent. This allows the following to be true:

$$p(\mathcal{Z}_k|\mathbf{x}(l), \mathbf{u}(l)) = \prod_{n=1}^N p(\mathbf{Z}_k^n|\mathbf{x}(l), \mathbf{u}(l)). \quad (2.7)$$

where the observation matrix  $\mathbf{Z}_k^n$  also contains observations from possible source signals as well as false observations. Due to uncertainty of the source signal in the observations of each receiver, calculation of the likelihood function  $p(\mathbf{Z}_k^n|\mathbf{x}(l), \mathbf{u}(l))$  requires data association.

Similar to probabilistic data association, the data association hypothesis  $\beta_{k,j}^n$  is defined as an event that the  $j^{\text{th}}$  observation vector in matrix  $\mathbf{Z}_k^n$  is generated by the source and other observations are false observations. The special case  $\beta_{k,0}^n$  denotes the case that all receiver observations are false observations. Using total probability theorem, the likelihood term  $p(\mathbf{Z}_k^n|\mathbf{x}(l), \mathbf{u}(l))$  is expanded over data association hypotheses as follows

$$p(\mathbf{Z}_k^n|\mathbf{x}(l), \mathbf{u}(l)) = \sum_{j=0}^{m_k^n} p(\beta_{k,j}^n) p(\mathbf{Z}_k^n|\beta_{k,j}^n, \mathbf{x}(l), \mathbf{u}(l)). \quad (2.8)$$

The probability of each association event is calculated using the statistical properties of the false observation. When the source signal is detected with probability of  $P_D$ ,  $m_k^n - 1$  false alarms have been generated with probability of  $\mu_F(m_k^n - 1)$ . It is assumed that, given the source is detected by the sensor array ( $j \neq 0$ ), observations are equi-probable to be assigned as the source observation. Similarly for the case that the source observation is not detected ( $j = 0$ ), the probability of each association event is calculated using

$$p(\beta_{k,j}^n) = \begin{cases} (1 - P_D)\mu_F(m_k^n) & j = 0 \\ P_D\mu_F(m_k^n - 1)\frac{1}{m_k^n} & j \neq 0 \end{cases} \quad (2.9)$$

The likelihood term  $p(\mathbf{Z}_k^n|\beta_{k,j}^n, \mathbf{x}(l), \mathbf{u}(l))$  is the product of the likelihood of the true source and the false alarms. Since false alarm locations are uniformly distributed in the area of

interest with the surface of  $S$ , the likelihood term is calculated using

$$p(\mathbf{Z}_k^n | \beta_{k,j}^n, \mathbf{x}(l), \mathbf{u}(l)) = \begin{cases} \frac{1}{S^{m_k^n}} & j = 0 \\ \frac{1}{S^{m_k^n-1}} p(\mathbf{z}_{k,j}^n | \mathbf{x}(l), \mathbf{u}(l)) & j \neq 0 \end{cases}, \quad (2.10)$$

Substituting (2.9) and (2.10) into (2.8), the likelihood term is given by

$$p(\mathbf{Z}_k^n | \mathbf{x}(l), \mathbf{u}(l)) = \frac{(1 - P_D) \mu_F(m_k^n)}{S^{m_k^n}} + \frac{P_D \mu_F(m_k^n - 1)}{m_k^n S^{m_k^n-1}} \sum_{j=1}^{m_k^n} p(\mathbf{z}_{k,j}^n | \mathbf{x}(l), \mathbf{u}(l)). \quad (2.11)$$

In calculation of the likelihood term  $p(\mathbf{z}_{k,j}^n | \mathbf{x}(l), \mathbf{u}(l))$ , the given condition  $\mathbf{u}(l)$  means that the true source state lies inside the cell  $\mathbf{u}(l)$  which is represented by the state  $\mathbf{x}(l)$ . More simply, the source is in the area represented by  $\mathbf{x}(l)$ . Since the likelihood term is dependent on the cell, discretization error must be taken into account when calculating the likelihood function. In the tree-search structure, the size of the discrete cells  $\mathbf{u}(l)$  varies among different paths of the tree. For small cells, discretization error can be ignored in comparison to the observation noise. However, for large cells, ignoring the discretization error may drastically reduce the likelihood term in (2.11) for the sources that are not close to the representative state of the cell.

The discretization error  $\tilde{\mathbf{x}}$  is modeled as a uniformly distributed random variable to compensate the difference between the true source state ( $\dot{\mathbf{x}}$ ) and the cell representative state vector  $\mathbf{x}(l)$

$$\tilde{\mathbf{x}}(l) = \dot{\mathbf{x}} - \mathbf{x}(l). \quad (2.12)$$

Considering the discretization error, the likelihood term  $p(\mathbf{z}_{k,j}^n | \mathbf{x}(l), \mathbf{u}(l))$  is given by

$$\begin{aligned} p(\mathbf{z}_{k,j}^n | \mathbf{x}(l), \mathbf{u}(l)) &= \int_{\tilde{\mathbf{x}}(l)} p(\tilde{\mathbf{x}}) p(\mathbf{z}_{k,j}^n | \mathbf{x}(l), \tilde{\mathbf{x}}(l), \mathbf{u}(l)) \\ &= \frac{1}{S_l} \int_{\dot{\mathbf{x}} \in \mathbf{u}(l)} p(\mathbf{z}_{k,j}^n | \dot{\mathbf{x}}), \end{aligned} \quad (2.13)$$

where  $S_l$  is the surface area of the cell  $\mathbf{u}_l$ . Note that the measure space for the first Lebesgue integral is over all possible state discretization error in the cell, and the second Lebesgue integral is over all possible true source states in the cell. Considering the observation model in (2.1), for a given true source state  $\dot{\mathbf{x}}$ ,  $p(\mathbf{z}_{k,j}^n|\dot{\mathbf{x}})$  follows the statistics of the observation noise. However, the integral does not have a closed form for a general nonlinear function  $\mathcal{H}()$ . Numerical analysis techniques such as Gauss-Hermite quadrature rules [37] can be applied for calculating this integral, but they increase the computational complexity. Our approach for approximating the likelihood integral is based on linearizing the observation model using Taylor series expansion of the observation function and approximating the distribution function of the sensor observations given that the source is uniformly distributed in the cell  $\mathbf{u}(l)$ . Substituting (2.12) in the observation model (2.1), the sensor observation is given by

$$\begin{aligned}\mathbf{z}_{k,j}^n &= \mathcal{H}(\mathbf{x}(l) + \tilde{\mathbf{x}}(l)) + \mathbf{w}_k^n \\ &\approx \mathbf{H}\mathbf{x}(l) + \mathbf{H}\tilde{\mathbf{x}}(l) + \mathbf{w}_k^n\end{aligned}\tag{2.14}$$

where  $\mathbf{H}$  denotes the linearized matrix of the observation function  $\mathcal{H}()$  and  $\mathbf{H}\mathbf{x}(l)$  is a constant term. The elements of the discretization error state vector  $\tilde{\mathbf{x}}(l)$  are uniformly distributed and are independent, the distribution of  $\mathbf{H}\tilde{\mathbf{x}}$  is the linear combinations of the uniformly distributed independent random variables. Inferring from the Central Limit Theorem, we approximate this distribution as Gaussian. Based on the distribution of the observation noise  $\mathbf{w}_k^n$ , the probability distribution function  $p(\mathbf{z}_{k,j}^n|\mathbf{x}(l), \mathbf{u}(l))$  in (2.11) is calculated. As an example, assuming Gaussian distributed observation noise with zero mean and covariance matrix of  $R$  denoted by  $\mathcal{N}(0, R)$ , then

$$p(\mathbf{z}_{k,j}^n|\mathbf{x}(l), \mathbf{u}(l)) \approx \mathcal{N}(\mathbf{H}\mathbf{x}(l), \Sigma_{\mathbf{H}\tilde{\mathbf{x}}(l)} + R),\tag{2.15}$$

where  $\Sigma_{\mathbf{H}\tilde{\mathbf{x}}(l)}$  is the covariance matrix of the random term  $\mathbf{H}\tilde{\mathbf{x}}(l)$ . The proposed tree search algorithm, considering approximation of the likelihood function with Gaussian distribution function, can be justified as a tree search technique for approximating the posterior

distribution function of the source location using the Gaussian Kernels [47, 48]. Each discrete cell can be considered as a Gaussian Kernel. The algorithm adaptively changes the number of Gaussian Kernels used for distribution approximation and uses more Kernels in the vicinity of the source by selecting smaller cells. To reduce the computational complexity, the algorithm uses less Kernels (larger cells) in the areas that are unlikely to contain a source.

#### 2.2.2.2 Detection

The threshold must be varied based on the thresholds is addressed in this section. In source detection and localization problem, the environmental noise continuously generates false alarms or false contacts. In addition to reducing the estimation accuracy of the source localization technique, the noisy contacts may cause the estimation algorithm to declare the existence of sources that do not really exist. Conventional sequential Bayesian filtering techniques such as Kalman filtering and particle filtering do not provide a tool for validating the estimated source location, hence an external algorithm must be applied to perform this task. However, one advantage of the tree search technique for source localization is that the validation of the source location is performed in combination with the localization. This also extends the applications of the algorithm to multiple source detection and localization.

Looking for local maxima of the posterior function, the tree-search algorithm extends a path and narrows the search subset whenever the metric of the path is above a predefined threshold. To calculate the predefined threshold, we consider the conventional statistical Neyman-Pearson test, and we relate this test to the path metric of the developed tree-search technique.

Defining  $\mathcal{H}_0$  and  $\mathcal{H}_1$  as the source present and the source absent hypotheses, respectively, the ratio of the observation likelihood functions under source present hypothesis and source absent hypothesis (Neyman-Pearson test) provides a validation tool

as follows

$$\begin{aligned}
\lambda(l) &= \log \frac{p(\mathcal{Z}_1, \dots, \mathcal{Z}_K | \mathbf{x}(l), \mathcal{H}_0)}{p(\mathcal{Z}_1, \dots, \mathcal{Z}_K | \mathbf{x}(l), \mathcal{H}_1)} \\
&= \sum_{k=1}^K \log \frac{p(\mathcal{Z}_k | \mathbf{x}(l), \mathcal{H}_0)}{p(\mathcal{Z}_k | \mathbf{x}(l), \mathcal{H}_1)} \\
&= \sum_{k=1}^K \sum_{n=1}^N \log \frac{p(\mathbf{Z}_k^n | \mathbf{x}(l), \mathcal{H}_0)}{p(\mathbf{Z}_k^n | \mathbf{x}(l), \mathcal{H}_1)}.
\end{aligned} \tag{2.16}$$

Calculation of  $p(\mathbf{Z}_k^n | \mathbf{x}(l), \mathcal{H}_0)$  is addressed in path metric calculation (2.11), while the second term  $p(\mathbf{Z}_k^n | \mathbf{x}(l), \mathcal{H}_1)$  is derived from the statistics of the false contacts considering that the false alarms are uniformly distributed and independent of the source state

$$p(\mathbf{Z}_k^n | \mathbf{x}(l), \mathcal{H}_1) = \frac{\mu_F(m_k^n)}{S^{m_k^n}}. \tag{2.17}$$

Denoting

$$\nu_k^n = \log \frac{p(\mathbf{Z}_k^n | \mathbf{x}(l), \mathcal{H}_0)}{p(\mathbf{Z}_k^n | \mathbf{x}(l), \mathcal{H}_1)}, \tag{2.18}$$

and substituting (2.17) and (2.11) in (2.16), then we have

$$\lambda(l) = \sum_{k=1}^K \sum_{n=1}^N \nu_k^n, \tag{2.19}$$

where

$$\nu_k^n = \log \left[ 1 + \frac{P_D}{N_F(1 - P_D)} \sum_{j=1}^{m_i^n} p(\mathbf{z}_{k,j}^n | \mathbf{x}(l), \mathbf{u}(l)) \right]. \tag{2.20}$$

Replacing  $\nu_k^n$  in (2.16), the validation metric for each path is calculated. Note that  $\nu_k^n$  is proportional to the likelihood function of the path metric that is calculated in (2.11).

Therefore, the validation metric is calculated from the path metric and does not increase the computational complexity of the proposed algorithm.

A path is extended in the proposed tree-search algorithm if its validation metric (proportional to the path metric) is greater than a predefined threshold  $\tau$ . This threshold is calculated by approximating the probability distribution function of the likelihood ratio

function and considering the probability of detecting the source in a cell  $P_{SD}$  and probability of false alarm declaration  $P_{FA}$  using

$$\mathbf{P}_{SD} = \int_{\lambda(l) > \tau} dp_{\lambda(l)|\mathcal{H}_0} \quad (2.21)$$

$$\mathbf{P}_{FA} = \int_{\lambda(l) > \tau} dp_{\lambda(l)|\mathcal{H}_1}, \quad (2.22)$$

where  $p_{\lambda(l)|\mathcal{H}_0}$  is the validation metric probability distribution function when the source exists in the cell represented by  $\mathbf{x}(l)$  and  $p_{\lambda(l)|\mathcal{H}_1}$  is when the source is not inside the cell. The probability distribution function of the likelihood ratio values has been well studied in the literature [50, 51]. Using the extreme value theory (extreme value theory (EVT)), the local maxima is approximated with Gaussian distribution if the source exists ( $\mathcal{H}_0$ ) and approximated with Gumbel distribution[51] ( $\mathcal{H}_1$ ) if the source is not in the area of interest. Using the same technique as in [50], the threshold for the likelihood ratio test can be calculated for the simulations in this work.

## 2.3 Experimental Setup

The first objectives was a proof of concept which required setting up a testbed to simulate leaks for detection and localization. The setup for the testbed went through a few iterations with different hardware and methods of data acquisition. The testbed included a rudimentary sensor system for detection, a method of simulating a leak, a form of data acquisition, and a manner of computation.

### 2.3.1 Sensor Array

The MEMS sensors chosen measured 3.76 mm wide, 4.74 mm long, and 1.4 mm tall. Built by Knowles Acoustic, the SPM0404U5 sensors are surface mount devices meant for PCBs. This required the design and printing of a simple PCB to allow connections for data acquisition.

In order to localize leaks, it would still be necessary to have multiple sensors to find the AOA. The design would have the MEMS sensors arranged in a line. This array would then

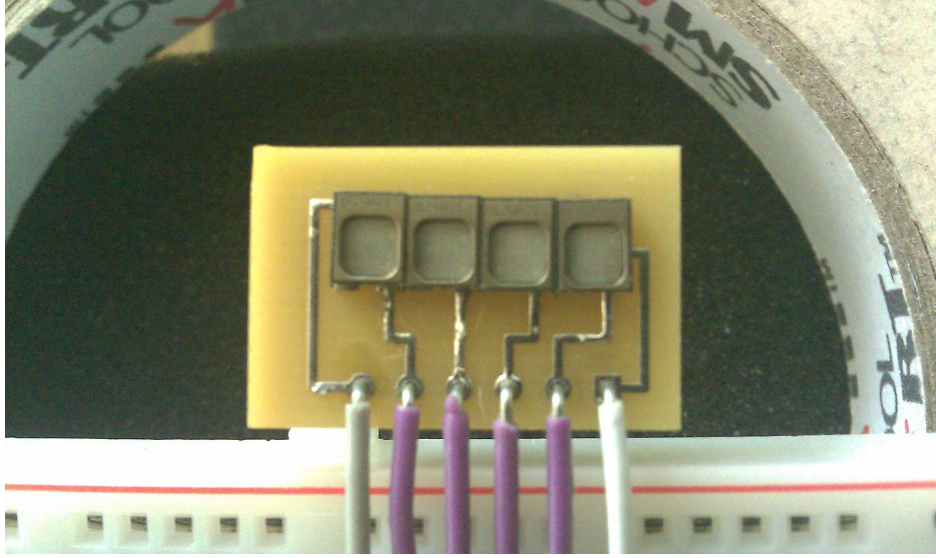


Figure 2.3. The linear array of four MEMS ultrasonic sensors used for leak detection.

be used to determine the AOA based on the TDOA. This array can be seen in Figure 2.3. For reference, Table 2.1 shows a comparison between these sensors and those used for simulated leaks.

	SPM0404U5	MaxSonar-UT
Operating Frequency	40-50 kHz	38-42 kHz
Device Type	MEMS	Piezoelectric
Directionality	Omnidirectional	3dB drop at 15° from reference
Power	Active (1.5-3.6 v)	Passive (Drive: 20 v RMS)
Sensitivity	-42 dB	-60 dB
Max. SPL	115 dB	117dB
Purpose	Microphone	Transducer

Table 2.1. Comparison of the two ultrasonic components used in experiments.

### 2.3.2 Simulated Leak Source

In order to test the ability to detect and localize leaks, a source would be needed to generate the ultrasonic noise. For this purpose, piezoelectric transducers were used for their ability to take an electrical signal and generate the necessary acoustics. A function generator is used to create a 40 kHz sine wave - a signal within range of both piezoelectric



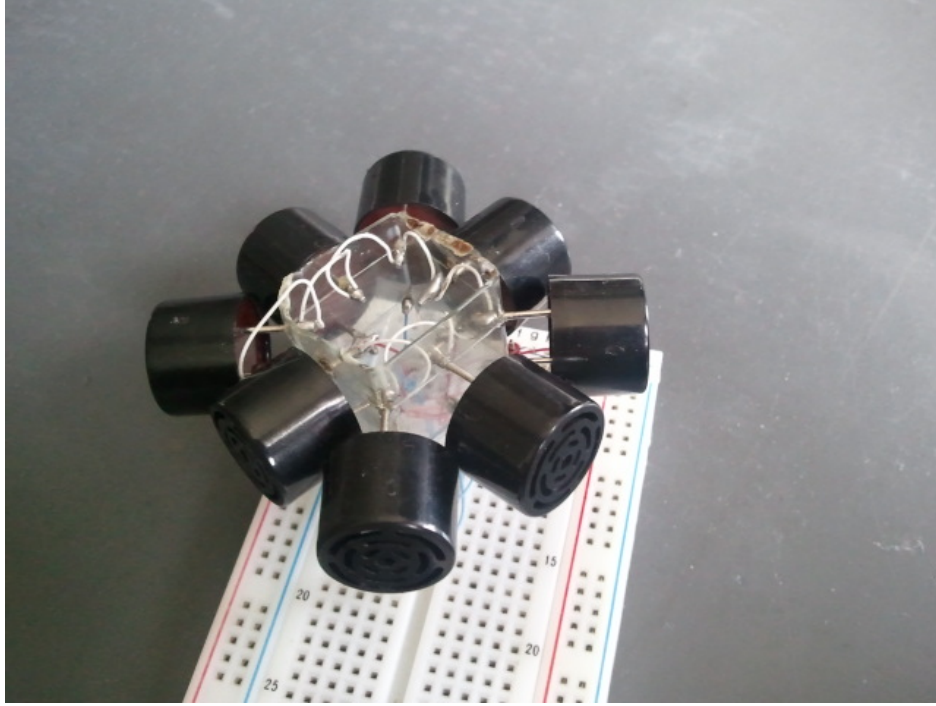


Figure 2.4. Prototype of a circular array of ultrasonic transducers.

and MEMS sensors. The generated signal is sent directly to the transducer producing a 40 kHz acoustic wave in air. It is this signal combined with the ambient environmental noise that is sampled by the MEMS sensors.

The piezoelectric device of choice was the MaxSonar-UT built by Mbotix. These sensors were piezoelectric sensors that were capable of detecting ultrasonic acoustic emissions within a 30° range. They were designed to work in the range of 38-42 kHz with a sensitivity of -60 dB. Since these were transducers, they were also capable of taking a signal within range and producing that signal as an acoustic signal up to 117 dB. The maximum voltage range for these passive sensors was 20 V. They measured 16.4 mm in diameter and were 12.2 mm tall.

Since the piezoelectric transducers are directional, multiple sensors are necessary to generate the signal in all directions to replicate a leak. Use of the circular array such as that seen in Figure 2.4 lead to small dead zones where the signal would not reach the sensors except by reflection due to the relatively small physical workspace. Another option

was to have one transducer but rotate it in a circle to cover the same area. Due to this factor and simplicity of testing, a single transducer was rotated to simulate an omnidirectional source. However, due to the manual placement of the source, human error prevents the source from remaining in the exact location. Such error contributes to the total error of the system and should be accounted accordingly. As mentioned this would also reduce the reflection component of the received signal possibly reducing error. The power range of the transducers allows one to test a wide range of SNR values for the testing of clear and weak signals.

A concern for practical purposes is the use of a 40 KHz signal rather than noise. Since a leak can generate noise at a wide range of frequencies, it might seem like realism is lost in this testbed. While leaks produce much noise, the only range of interest is the 38-42 kHz region where most devices are made to work. This is also the region where the leak produces the best ratio of leak noise to ambient noise. The system functions the same when the entire bandwidth of the sensors (as opposed to a narrower 40 kHz band) is used by the source.

### **2.3.3 Data Acquisition**

A set of Tektronix MSO2014 digital oscilloscopes such as that in Figure 2.5 were used to acquire the same data. These oscilloscopes had a sampling rate of 1 GS/s per channel for 4 channels. Data were saved to a flash drive and later imported by a MATLAB script for post-processing.

## **2.4 Laboratory Setup**

The final setup used for the complete tests were composed of four parts. The first is the simulated leak source composed of a MaxSonar-UT sensor connected to a signal generator. The signal generator creates a 40 kHz sine wave with a peak-to-peak voltage of 1 V. The output is a 40 kHz acoustic signal that represents the leak. This transducer is placed at a



Figure 2.5. Tektronix MSO2014 oscilloscope used for more detailed data acquisition.

point in a  $62'' \times 62''$  square and rotated such that the signal reaches all sensor arrays. The second part is the collection of sensor arrays. There are three sensor arrays located at coordinates  $(0,0)$ ,  $(62,0)$ , and  $(0,62)$ . Each one of the arrays is connected to the power supply set at 3VDC. The third part is the means of data acquisition. The individual sensors are each connected to a channel on an oscilloscope which saves 1 second of data to a flash drive. Finally, the last part is the MATLAB environment. The data is then imported into the MATLAB environment where the data is processed to calculate the approximated source locations from the sensor arrays and run the algorithm. This setup can be seen in Figure 2.6 and Figure 2.7.

#### 2.4.1 Simulations

The simulation scenario considers the challenge of sensor observations uncertainty in high levels of the background noise which produces numerous false observations at the receivers. We assume that each receiver is able to measure the bearing angle of the

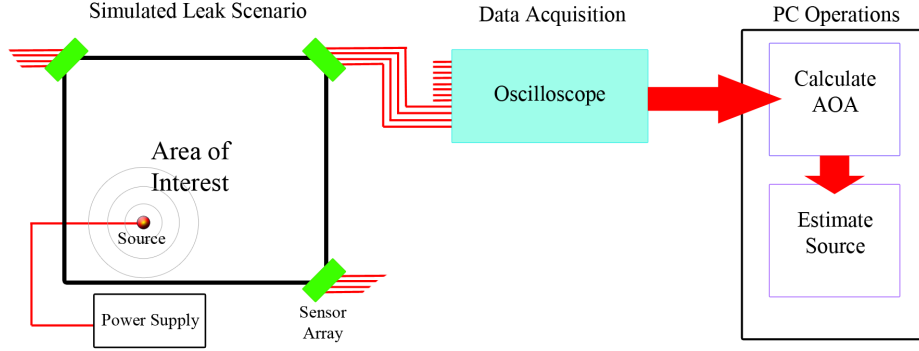


Figure 2.6. Generalized setup for experiments.

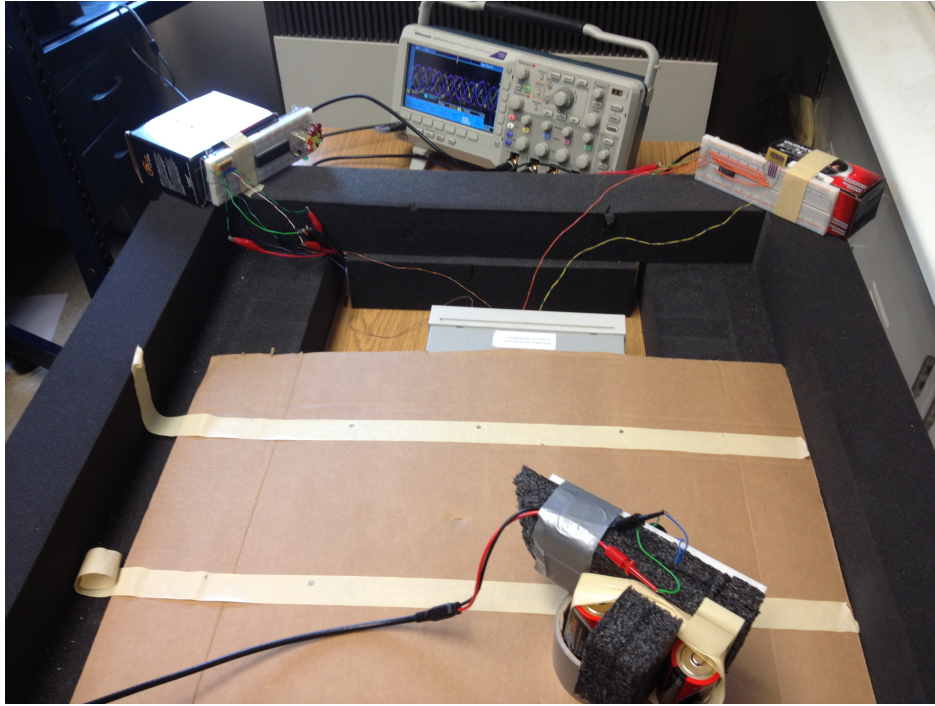


Figure 2.7. Completed setup for the data that was acquired

incoming signal using a linear array of the sensors. The range of the detected signal is assumed to be calculated from time difference of arrival among the receivers.

The simulated scenario considers four sensor arrays (receivers) located at  $(0,0)$ ,  $(10,0)$ ,  $(0,10)$ , and  $(10,10)$  in a flat two-dimensional Cartesian coordinate system with each unit denoting 1 meter (m). One source is randomly generated in the region of interest that is

surrounded by these four receivers. The source state vector is defined in two dimensional Cartesian coordinate system  $[x \ y]^T$ , and the receiver observation (in Polar coordinate system) is related to the source state using the following observation model function

$$\mathcal{H}(\mathbf{x}) = \begin{bmatrix} \sqrt{x^2 + y^2} \\ \tan^{-1}(y/x) \end{bmatrix}. \quad (2.23)$$

In the simulations, it is assumed that the false alarm rate  $N_F$  is given for location estimation. The simulated tree-search algorithm uses observations from 20 independent scans of each receiver. In path extension of the tree search algorithm, each state (subset of the source state space) is divided into four smaller states, and the center point of each small cell is selected as a discrete state. The estimated source location is declared when the dimension of the subset containing the source is smaller than  $1\text{cm} \times 1\text{cm}$ . The maximum number of sustained paths in the tree is set to 64, and if the tree gets larger, the paths with smaller metrics are eliminated from the tree.

Figure 2.8 shows a realization of the simulation scenario in 10 independent scans from each sensors. The observation contacts for 10 scans of the receivers including source observations and false alarms are shown with dots. A source generated signal is detected by a receiver with the probability  $P_D = 0.8$  and the average number of false alarms per receiver is set to  $N_F = 2$ . The standard deviation (std) for the source range is set to 0.4m and for the angle of arrival (bearing) is set to  $2^\circ$ .

The performance of the algorithm is measured through root mean square error of the source location estimation versus number of scans from the receivers. As the number of scans from the receivers increases, we expect that the algorithm converges to the true source location. To evaluate the mean square error of the estimated source location, 50 independent realizations of the source and sensor observations were simulated. Figure 2.9 and Figure 2.10 show the root mean square error (RMSE) of the algorithm vs number of receiver scans for different values of the false alarm rates and the standard deviation (STDEV) of the observation noise. For these plots, the probability of detecting

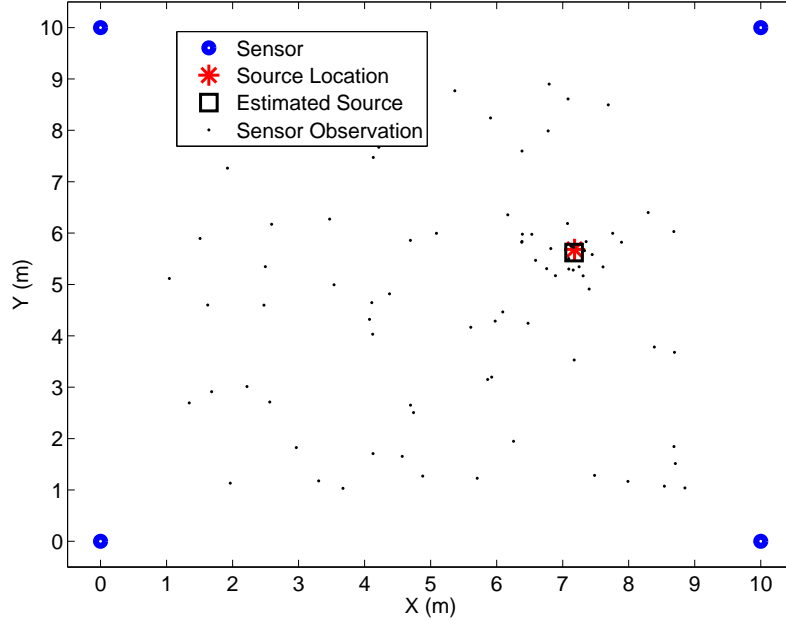


Figure 2.8. A realization of the simulated scenario; the true source location, the estimated source location using the proposed tree-search, and observations including contacts and false alarms from four sensor scans.

the true source signal is set to  $P_D = 0.8$ . In Figure 2.9, the STDEV of the observation noise is fixed to  $2^\circ$  for the bearing angle and 0.4m for the range, but the false alarm rate varies from 2 – 16 average false alarms per receiver. We see that, increased false alarm rate up to 16 increases the number of required scans for the source estimation from 2 scans to 5, but does not effectively change the RMSE of the algorithm. In Figure 2.10, the average false alarm rate is fixed to 16 but the STDEV of the observation noise is changing from  $2^\circ$  to  $6^\circ$  for the bearing angle and from 0.4m to 1.5m for the range. We can see that the number of required scans for source localization and the value of the RMSE increases when the observation noise power increases.

Figure 2.11 shows the performance comparison of the proposed algorithm with that of the particle filtering technique [23] in terms of mean square error of the source estimation. The particle filter algorithm is modified to be implemented with ultrasonic signals using the likelihood function calculated in (2.11). This technique uses 2048 particles, and the

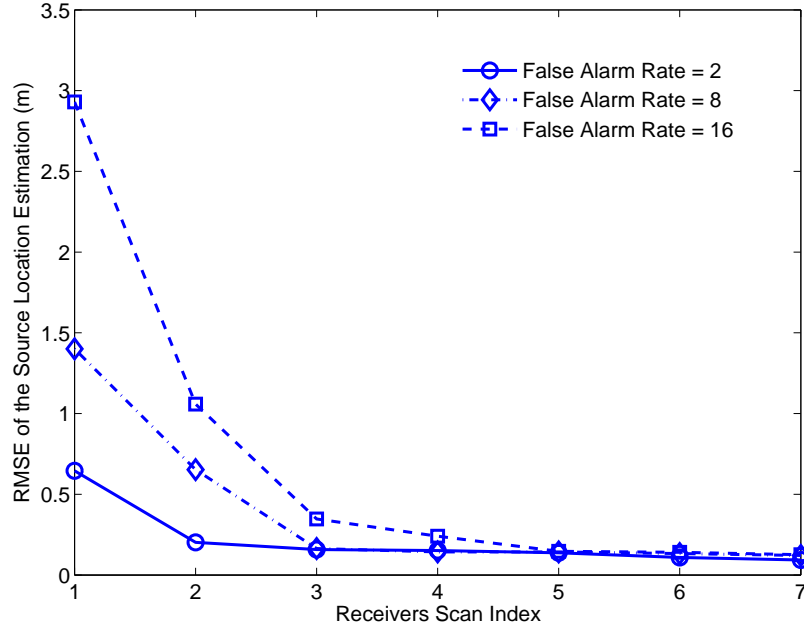


Figure 2.9. Effect of the false alarm rate on root mean square error (RMSE) of the estimated source location.

re-sampling step is performed when the effective number of particles are less than 500. The update of the particle weights is proportional to the path metric 2.6 in the proposed technique for fair comparisons. Any other assumption for the particle filtering technique can also be applied in the path metric of the proposed tree-search technique. Two scenarios have been simulated; in the first scenario, the probability of target detection is set to 0.8 while in the second one, it is set to 0.6. The average number of false alarm detections for each sensor is 2. Low probability of source signal detection and high false alarm rate is a challenging condition that the tree-search algorithm converges faster and stays in lower error surface than the particle filter algorithm. Note that in the proposed tree-search algorithm, the maximum number of sustained paths is set to 512 and if the algorithm extends all the paths to all subsequent states, it must calculate the metric for  $4 \times 512$  new states where the 4 denotes the number of subsequent states from each existing state. The PF algorithm uses 2048 particles and in each iteration, it recalculates 2048 particle weights

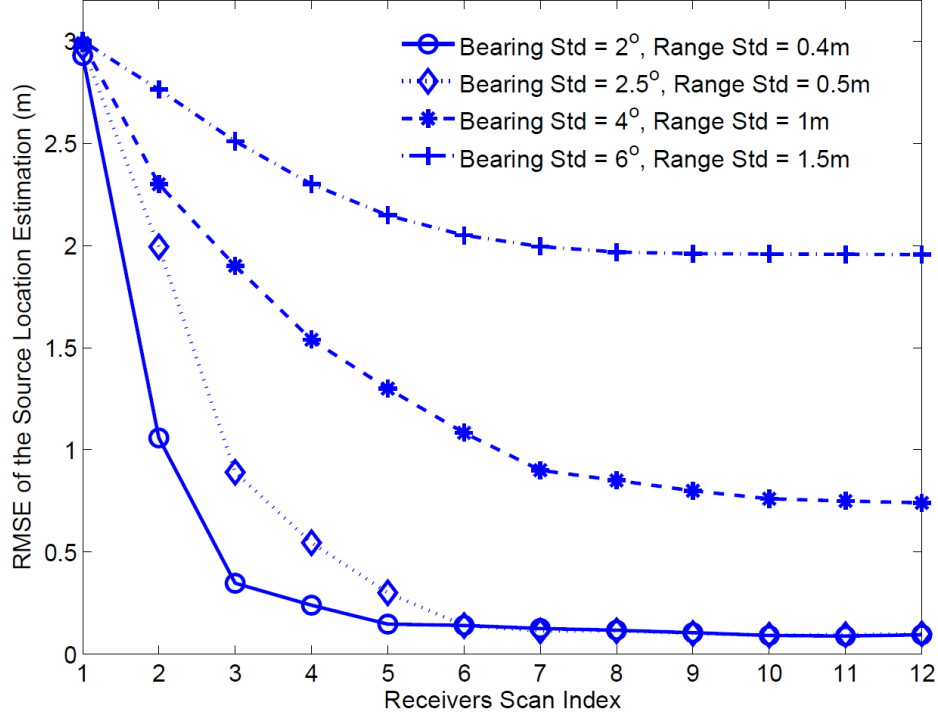


Figure 2.10. Effect of observation noise on root mean square error (RMSE) of the estimated source location.

in each iteration. Our simulation shows that in the proposed tree-search technique, usually less than 25% of the existing paths are extended and the algorithm is roughly four times faster than the particle filtering technique.

The performance advantage of the tree search algorithm with respect to the particle filtering is the ability of the tree search tracker to keep looking at areas where the true source signal may not be observed in first scans. In environments with high false alarm rate, the particle filtering generates more particles around areas with dense false alarms which may lead to losing the particles that are representing the source in the re-sampling procedure. In the proposed algorithm, we only develop few paths around high density false alarm areas (with higher path metric) and will always look back to the undeveloped paths of the tree if it can revise the estimation when it finds that the undeveloped paths are more likely. The other difference that increases the accuracy of the proposed algorithm with respect to the particle filtering is that the particle filtering estimates the posterior



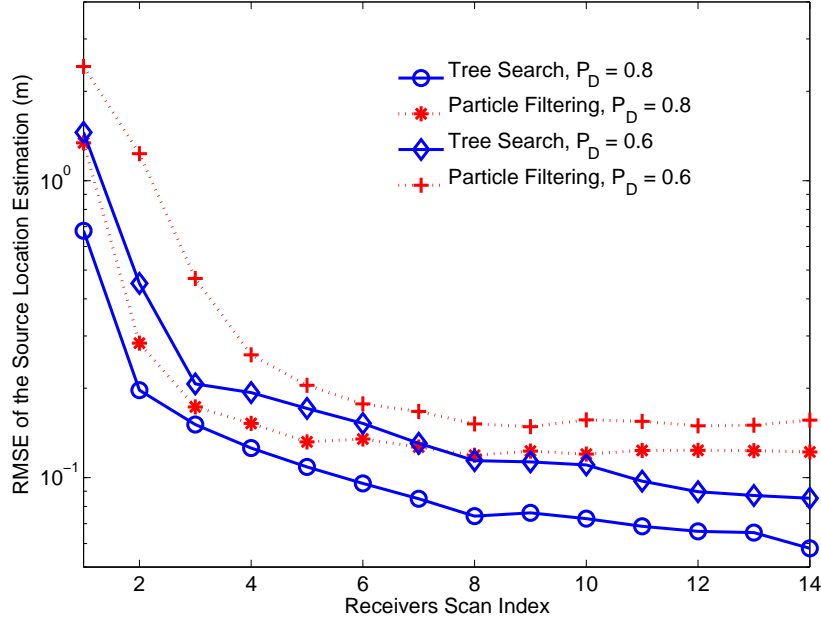


Figure 2.11. Performance comparison of the proposed techniques with different probability of target detection and comparison with the particle filtering technique.

distribution and the source state estimation is the expected value of the estimation. The proposed algorithm looks for the local maxima of the posterior distribution through the tree and the estimation is based on the local maxima that has the highest metric among the others. Therefore, there is no averaging in the estimation as in the particle filtering.

## 2.5 Experiments

In the experimental scenario, the bearing angle of the incoming signal is the only measurement, and the challenge is the high level of observation noise and the measurement bias due to human error in the experimental data acquisition.

Three ultrasonic sensor arrays (receivers) located at  $(0, 0)$ ,  $(62, 0)$ , and  $(0, 62)$  in a Cartesian coordinate where each unit denotes 1 inch (in) were used to monitor a  $62'' \times 62''$  square area in the two-dimensional Cartesian coordinate system. Each array contains three ultrasonic sensors located in a linear array and the distance between the sensors is 4mm.

The simple beamforming technique mentioned in 2.2.1 is utilized to estimate the angle of arrival of the incoming signals which has a nonlinear relation to the source state. One source is randomly generated in the region of interest. Using the setup summarized from 2.4, we approximate the observation noise variance using 100 independent experiments resulting in the approximation of  $5^\circ$ . The measured true source bearing angle that is used to verify the estimated location is assumed to be Gaussian distributed with zero mean and variance of  $5^\circ$  as well.

The RMSE of the physical experiment can be seen in Figure 2.12 represented by the blue components. To check the validity of the selected parameters for the experimental results, we have simulated the leak detector algorithm with three receivers located at the same locations as in the experiments. The STDEV of the bearing angle is selected as  $5^\circ$ . The performance results of this simulated scenario is plotted alongside with experimental results in Figure 2.12. The experimental results show that the root mean square error of the leak location estimation has a surface error of 4 inches. This is primarily due to the experimental human error in measuring the true source location in the experiments. Overall, the close match between simulation and experimental results verifies the effectiveness of the proposed leak detection and localization method.

## 2.6 Summary of Contributions

The problem of source detection and localization can be addressed by non-Gaussian systems. However, the current methods for non-Gaussian systems are very complex and not suitable for real time analysis by small sensor devices. In order to solve the general detection and localization problem, a low complexity tree-search technique was developed. This method accomplishes both detection and localization goals using observations collected from an ultrasonic sensor network. The posterior PDF of the source state is approximated only in the regions with high likelihood. The algorithm reduces computational complexity of a general Bayesian filtering solution.

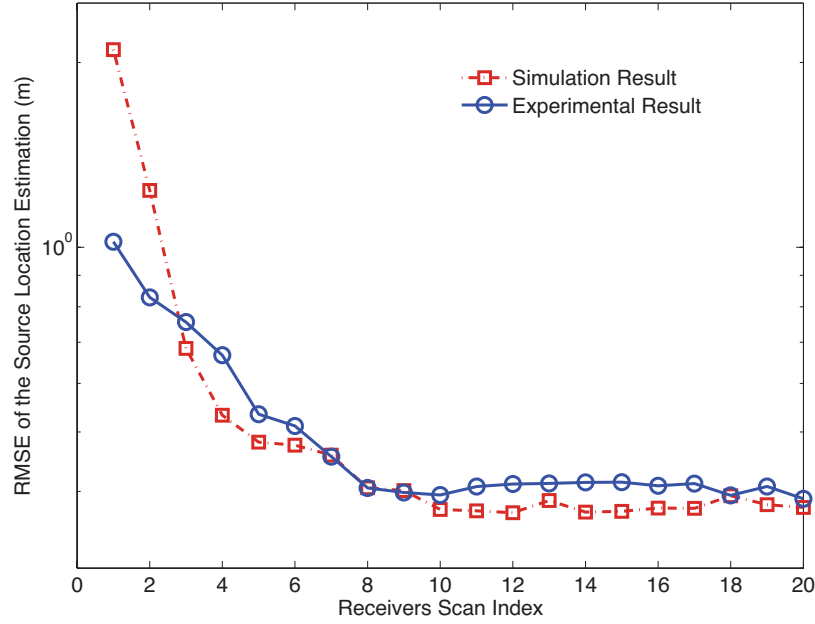


Figure 2.12. Comparing results from lab experiments with that of the simulated algorithm.

Applying an adopted version of the tree-search algorithm to the ultrasonic leak detection and localization problem is the novel part of this work. Compared to current methods using ultrasonic emissions from leaks, this work takes the low sound pressure of smaller leaks into consideration to address the difficulty in determining the presence of small leaks in high levels of background noise. The developed Bayesian filter is capable of handling the non-linear relation between the leak state and observation state spaces using Gaussian kernels. The use of Gaussian kernels is justified by the Gaussian distribution function of the likelihood term used to find a path metric. This requires the use of Gaussian distributed noise which may not always be accurate. The adaptive use of kernels allows for lower complexity of the algorithm compared to other popular methods such as the particle filter and maximum likelihood probabilistic data association.

The tree search algorithm managed to localize leaks up to 50% closer to the simulated leak than the particle filter using the same probability of observation. Extending higher probable paths translates into fewer numbers of particles to update which in turn leads to

faster results. As noted in the simulation results, Section (2.4.1), the tree-search algorithm performed up to 4 times faster than the particle filter with a set number of particles. The experimental results followed the simulations fairly well even when considering human error. The experimental results did not exceed 1.5 cm farther from the source than the simulations with regard to the RMSE floor. These promising performance results from simulations and laboratory experiments suggest extension of the algorithm to various fields.

## CHAPTER 3

### INTERNATIONAL SPACE STATION PAYLOAD

As a background, the International Space Station is primarily a laboratory in LEO that serves as an environment to perform experiments in microgravity and vacuum of space. It also serves as an orbital observatory for Earth and beyond. Originally started in 1998, the structure is assembled from individual modules developed by five space agencies and completed in 2011 with the last flight of the Space Shuttle Program. While technically completed, the ISS still undergoes occasional module additions. One of the original purposes of the ISS was to act as a multipurpose station for future exploration and expedition to our moon and other planets in the solar system. Purposes included serving as a location to develop, build, and test components, vehicles, and more for transport to the Moon. While these missions fell to the way side in favor of laboratory duties, there are still goals of returning to the Moon and eventually manned missions to Mars.

The Space Launch System (SLS) is set to be the most powerful rocket yet with the express purpose of allowing the largest payload yet - more than double that of the Space

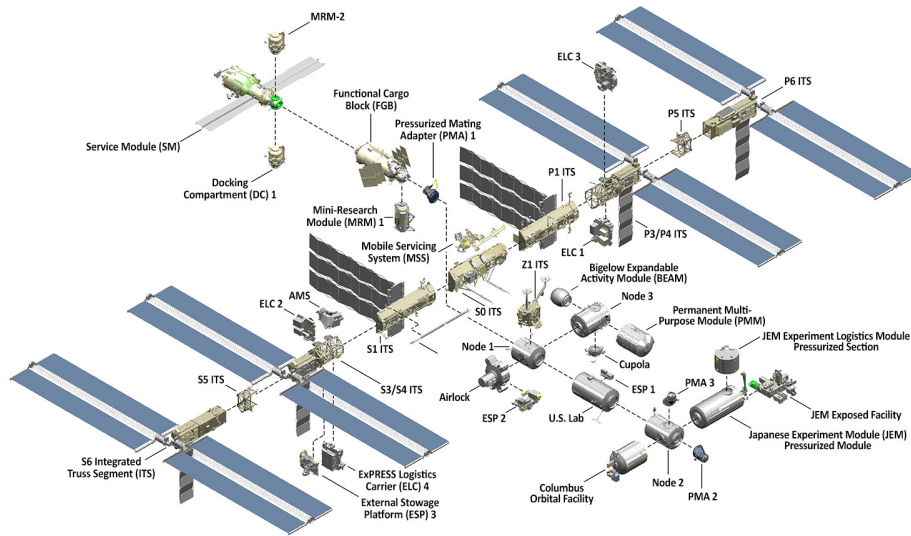


Figure 3.1. An exploded view of the ISS as of 2019 [53].

Shuttle. It will serve as a means for transporting crew and supplies for larger missions including lunar, mars, and other deep space locations. These types of missions, especially a crewed mission to Mars, will require some means of habitation for the crew. With greater distance from Earth and associated longer travel time, evacuation of a damaged habitat is not feasible. Therefore protection of said habitat is paramount. While the ISS crew are capable of evacuating back to ground in a few hours, the need for habitat protection is a high priority. For this reason and its purpose as a testbed the ISS makes for the best location to test a leak detection and localization system.

In order to test the leak detection algorithm discussed in Section 2.2, a self contained system based on the testbed described in Section 2.3 was designed and built for use on the ISS. The complete operational configuration for the prototype dubbed Wireless Leak Detector (WLD) system can be examined in Figure 3.2. Sections 3.1-3.6 will discuss the necessary changes and pre-flight testing that need to be mentioned before discussing deployment and analysis. More details about the design and testing process can be gathered from the Master's thesis of Mr. Clark, the main contributor in the construction of the prototypes. [58]. If successful, valuable data on ultrasonics in microgravity environments can be collected and used to further improve the system design. While the design was based on the previously discussed testbed, much of the design was modified for use aboard the station. This chapter will primarily discuss those changes and then focus on analysis of the results.

### **3.1 Sensor Array**

One of the minor changes from testbed is the sensor model. While still employing MEMS ultrasonic microphones, the new sensors are Knowles SPH0642HT5H-1's SiSonic Microphones. These sensors have a wider band of sound ranging from about 100 Hz to 50 kHz with peak at 30 kHz with slightly lower sensitivity of  $-38 \frac{dBV}{Pa}$ . The wider audio range may allows us to listen to more of the environment than the original sensors that had a

narrow bandwidth of 4 kHz centered around 40 kHz. Another modification was the use of only two sensors spaced per array approximately 3.8 mm apart but increasing the number of arrays to three on the same plane. This may be due to the ADC used but it also provides three angle of arrival calculations with more distant starting point which should provide better accuracy. As a side-note, the delay between any pair of adjacent pair of sensors on the original 3 sensor arrays would be extremely similar. This would provide no extra data when used in practical scenarios where resolution may be limited. The designed sensor arrays can be seen in Figure 3.3.

### 3.2 Data Collection

In order to be a deployable system, it is necessary for data acquisition and analysis or computation to be accomplished by the same device. While the testbed used a high sampling rate oscilloscope and PC for acquisition and analysis, respectively, these would be far too large and power consuming for wireless implementation. To replace the CPU an Arduino Due microprocessor board is used in conjunction with an external ADC board with higher sampling rate than the Due.

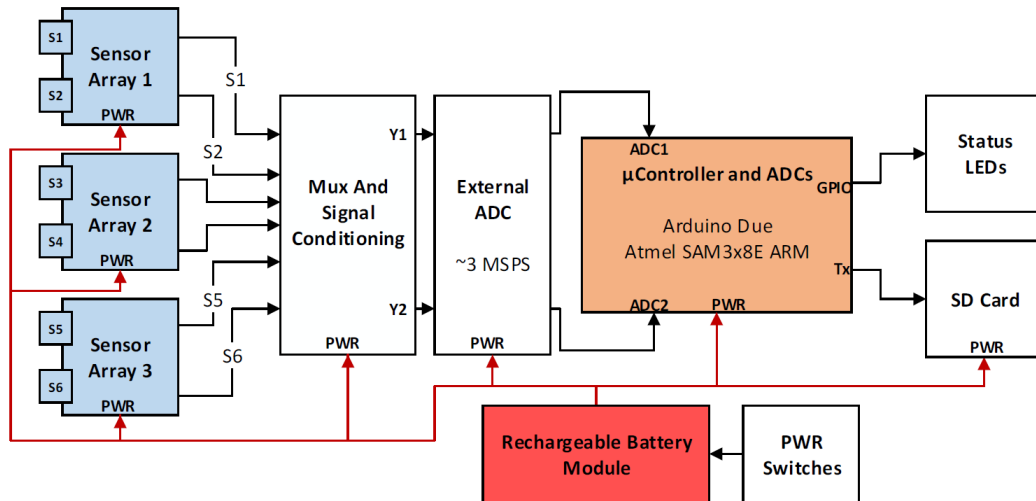


Figure 3.2. Block diagram of the WLD system.

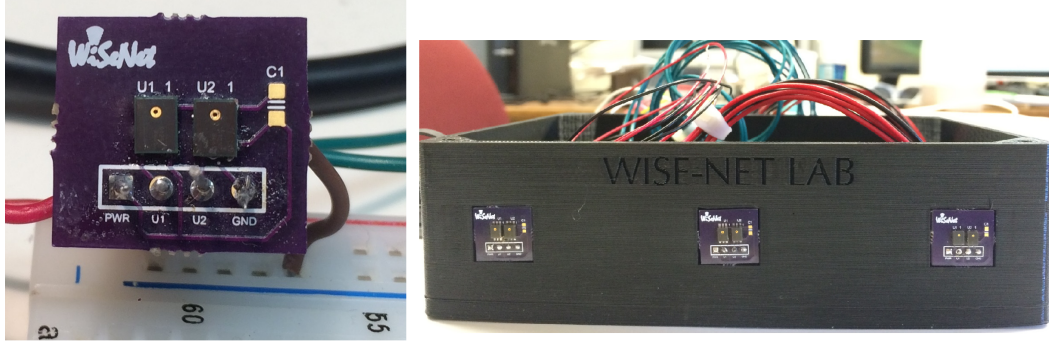


Figure 3.3. Deployed setup of ultrasonic sensor arrays.

### 3.2.1 Analog to Digital Converter

The ADC selected was an Analog Devices AD9201 capable of dual-channel sampling at 20 MSa/s with 10-bit resolution. While the ADC's sampling rate would allow very clear of the signal compared to the Due's on board ADCs, the sampling rate is still limited by the speed of the CPU. Given the clock settings and max speed of the Arduino Due, the max sampling rate of the coupled units is approximately 3.842 MSa/s. This reduces the potential samples per cycle for a 40 kHz signal from 500 to approximately 96 which should still provide a relatively good representation of the incoming signal range. Between the sensors and the ADC are two other systems, namely the multiplexer and analog filter. Neither set of circuitry affects the max sampling rate since the bottleneck is the CPU board. The multiplexer allows the device to focus on a single array at a time since the ADC is dual-channel. The filtering originally being done in the software was opted to be partially replaced with physical filters. This bandpass filter, which can be seen in Figure 3.4 along with amplifier, has cutoff frequencies of 20 and 60 kHz with adjustable gain up to 20 dB to deal with a wide range of leak and noise ratios.

### 3.2.2 Processing Unit

The Arduino line of microcontrollers is a commonly used platform for prototyping and experimentation due to relatively low cost and simplified interfacing with hardware via



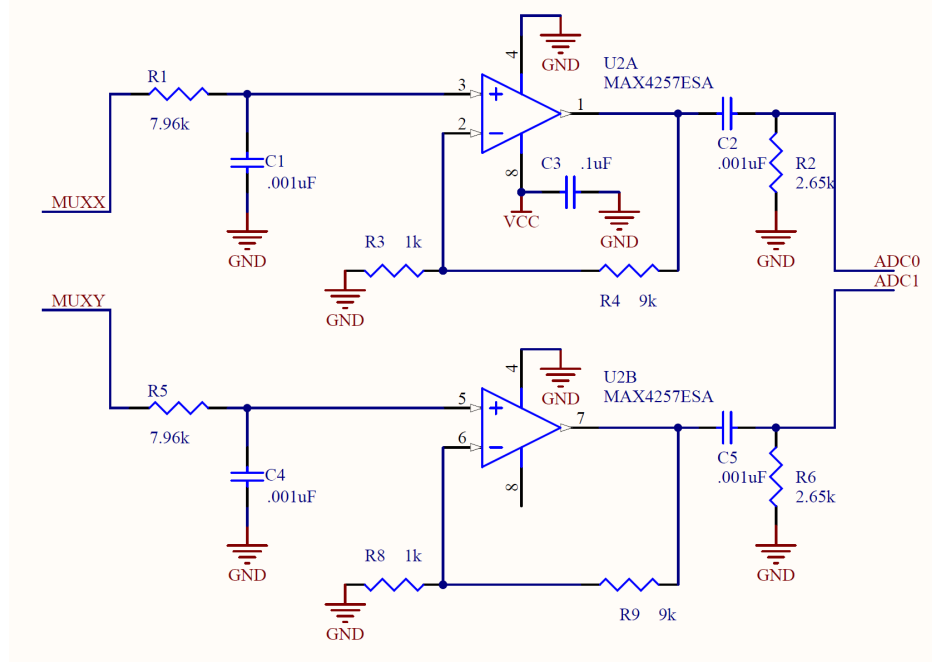


Figure 3.4. Schematic for bandpass filtering and amplification .

extensive libraries from both first and third party. The Due was selected purely for its speed. Most Arduinos are Atmel ATmega based microcontrollers but the Due is equipped with an ARM microcontroller. The Cortex M3 ARM expends more energy but for much more processing power and speed allowing sampling speeds greater than what would be available on lower level devices. The AT91SAM3X8E ARM microcontroller is a 32 bit chip operating at 3.3 V and up to 800 mA with a base clock speed of 84 MHz. It also has 512 kB of flash and native USB port that may be used for data transfer in the future.

### 3.3 Assembly

The sensors array, CPU board, and power supply are mounted to a custom designed enclosure seen in Figure 3.5. Also included in the enclosure design are interfaces for USB charging, an SD card slot for data storage on SD and SDHC cards, and power switches for simple startup and shutdown. The power supply used is a 9000 mAh Jackery GIANT+ rechargeable Lithium Polymer battery module. Given an average current draw of 330 mA

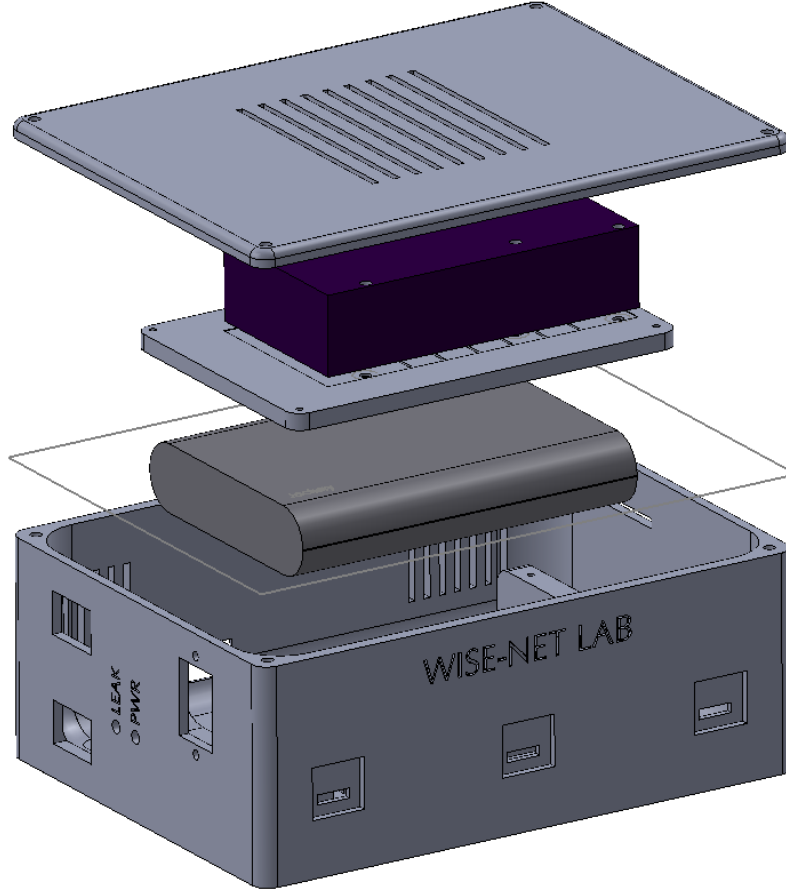


Figure 3.5. Custom designed and printed enclosure [58].

for the system at a board voltage of 5 V, the estimated lifespan of the device without charging is almost 28 hours. Recharge time from extremely low charge levels is estimated to be about 9.5 hours. All data collection hardware and connectors are located on a custom built PCB seen in Figure 3.6.

### 3.4 Laboratory Testing

Like in the previous work seen in Chapter 2 the prototype was verified to work as designed. Rather than the three sensor array setup to cover a square area seen in Section 2.4, the single box with three collinear sensor arrays attempts to localize simulated leaks

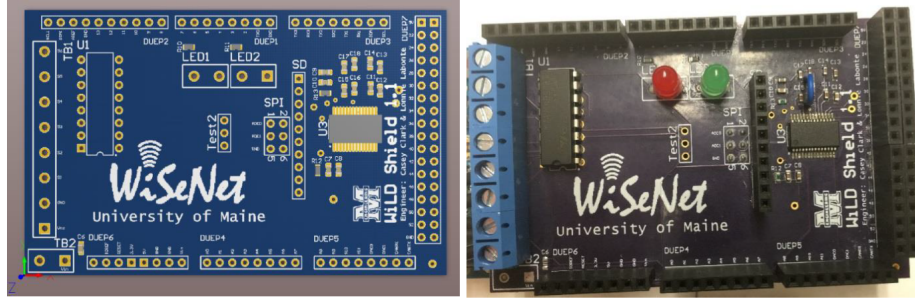


Figure 3.6. Custom designed PCB.

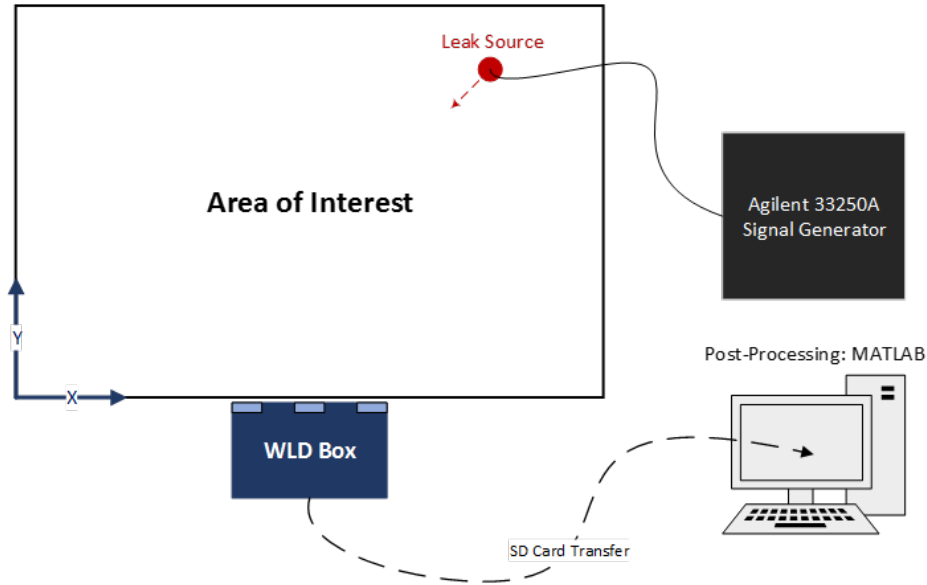


Figure 3.7. Area of interest for testing deployed design [58].

points in an area of interest seen in Figure 3.7. Code on the device was designed to take a large number of samples and calculate the AOA for each set of samples. This data, both the time samples and AOA estimates, are saved to SD card for the localization method analysis on external PC. As before, a transducer powered by a function generator is used to simulate a source using a 40 kHz signal. Another addition to this setup is the use of a custom pseudo-anechoic chamber seen in Figure 3.8 in an attempt to reduce noise and interference for more effective localization tests. Figure 3.9 reveals that while there is some attenuation in lower frequencies, there is approximately a 1-3 dB gain in the desired band.

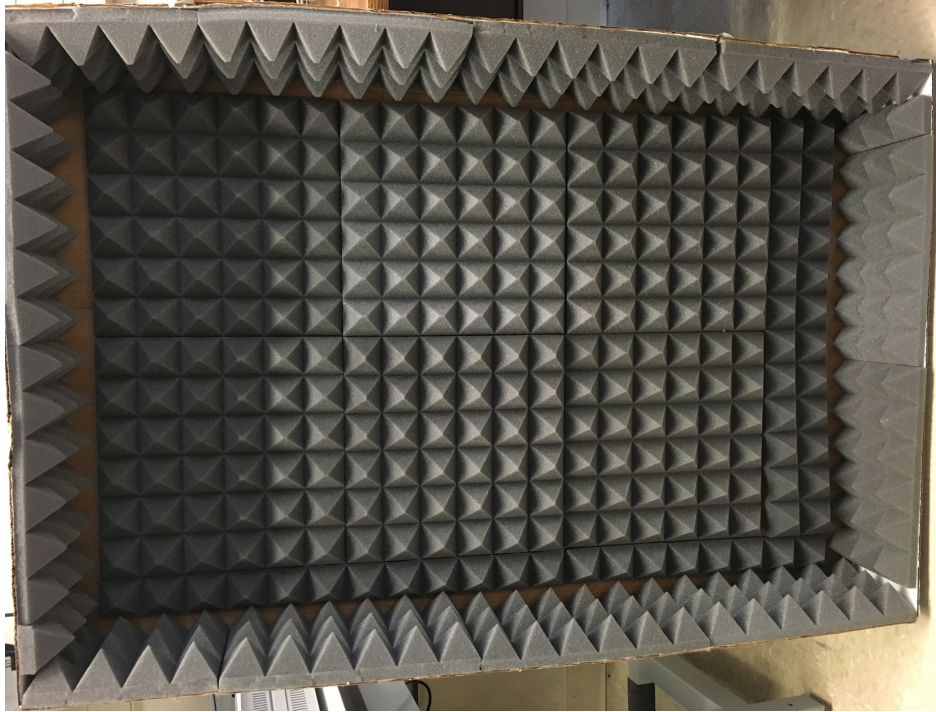


Figure 3.8. Custom pseudo-anechoic chamber used in testing.

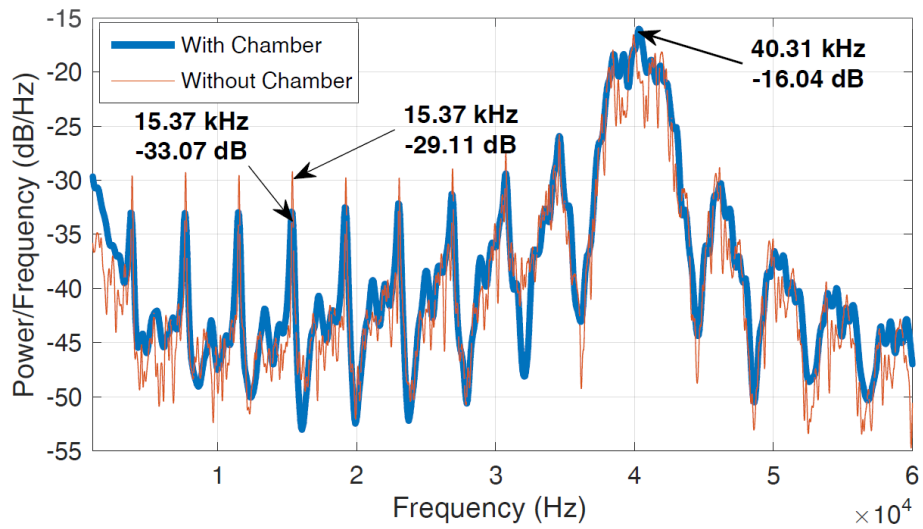


Figure 3.9. PSD of 40 kHz signal and ambient noise with and without anechoic chamber [58].

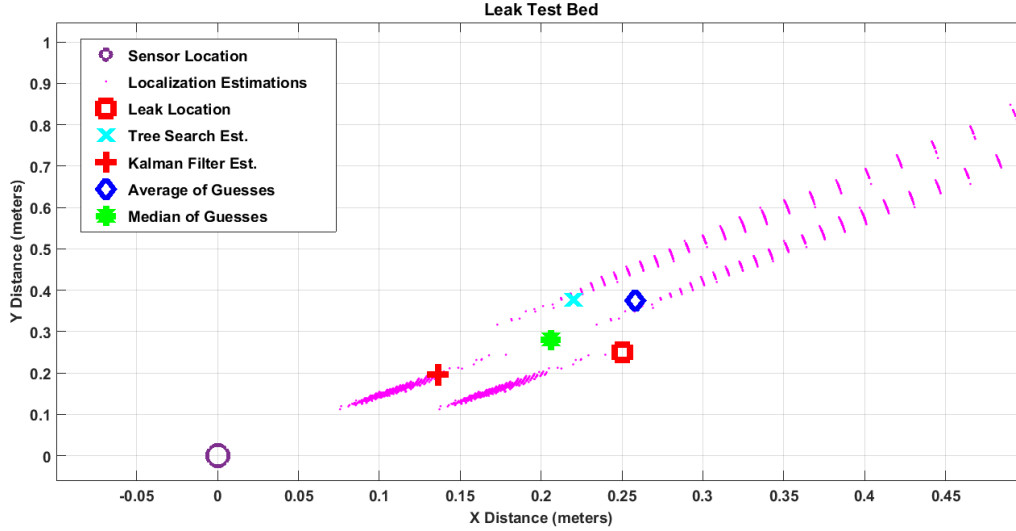


Figure 3.10. Lab-test results with leak source at .25 x .25 m.

### 3.5 Prototype Results

Several hours worth of samples from a set of points were collected and processed on board to find AOA estimates for each sensor pair. Most tests were done without the pseudo-anechoic chamber. The location estimates were then calculated and stored with AOA and raw data to an SD card. The data were then processed on an external computer to be run through both the tree search method and a Kalman filter. An example of leak test results can be seen in Figure 3.10 and all set location results can be seen in Table 3.1. Further an analysis of the relationship between distance from the source to the sensors and the error distance can be seen in Figure 3.11. As expected, the error increases as the distance from the sensors increases.

### 3.6 Field Test at JSC Mock ISS Module

Functional testing of the payload prototype was conducted in April 2016 at Johnson Space Center's mockups of US modules Nodes 1 and 2. These mockups are built on a 1:1

Table 3.1. Measured accuracy of prototype during lab based testing.

Source (m)	Sound Chamber?	Source Signal	Tree-Search Error	Kalman Error
.10 x .20	No	40 kHz 3 V	.122 m	.141 m
.25 x .25	No	40 kHz 3 V	.104 m	.107 m
.16 x .15	No	40 kHz 5 V	.082 m	.100 m
.20 x .20	No	40 kHz 5 V	.110 m	.101 m
.20 x .30	Yes	39 kHz 5 V	.100 m	.116 m
.30 x .20	Yes	40 kHz 3 V	.111 m	.69 m
.30 x .40	No	42 kHz 3 V	.215 m	.132 m
.20 x .20	No	42 kHz 3 V	.215 m	.108 m

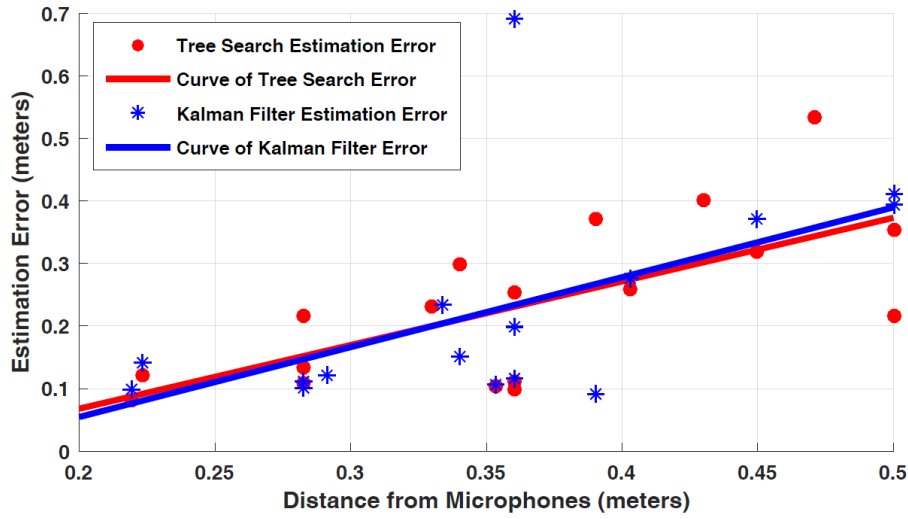


Figure 3.11. Error of Kalman filter and tree-search versus source distance [58].

scale of actual deployed nodes, however, they are a simple structural shape representation. As such, the materials used for construction are vastly different, and much of the instrumentation is not present. This lack of an accurate representation is expected to cause some discrepancies of WLD results in the mockups versus the ISS.

A single WLD unit was temporarily mounted in specific orientations at each of the three locations using Velcro strips previously decided in a Topology Study. These orientations and locations would mimic those of deployment for the scheduled ACTs seen in Section 3.7.1.1. At each of the three locations, the unit collected and stored acoustics measurements in 10 minute intervals. The first interval included a baseline test with no

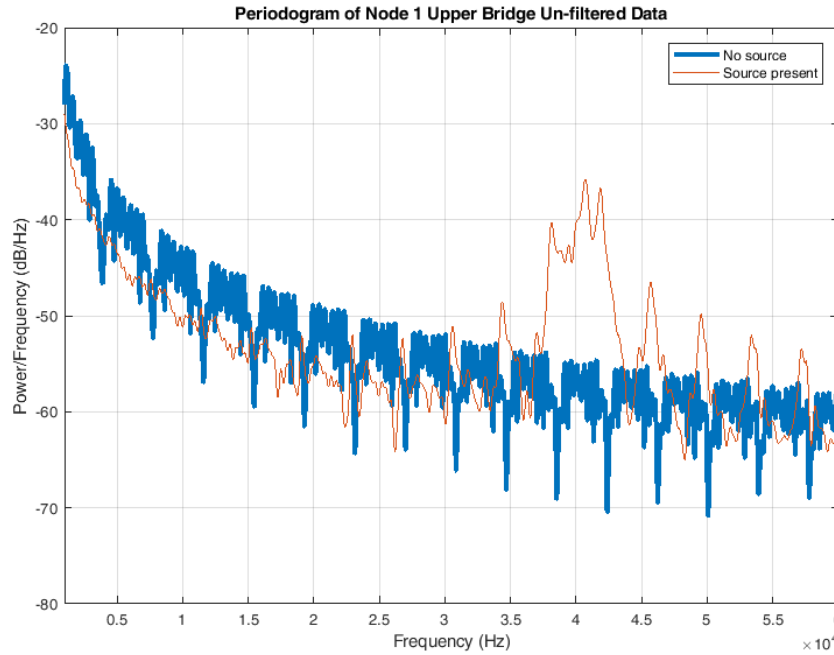


Figure 3.12. Power spectral density of received signal in mockups [58].

simulated source and acts as a background noise measurement. Two more intervals were recorded with the source generated using the transducers described in Section 2.3.2 at two separate locations. Post-processing was performed using MATLAB and includes power spectral density analysis, and comparison of filtered and unfiltered data. It is clearly seen that the source is observed by the payload in Figure 3.12 with an approximate 15 dB peak over background. The bandpass filter’s effects can be seen in Figure 3.13.

### 3.7 ISS Testing and Analysis

On December 9, 2016 three prototypes built for testing on-board the ISS were launched aboard a HTV-6 that docked with the ISS on December 13. From January 23 to January 26, 2017 the three devices were setup at three different locations for three separate tests. Data was transmitted to ground for analysis with 48 hours of deployment. This chapter will cover the locations chosen for testing, the setup of the tests, and the actual analysis of



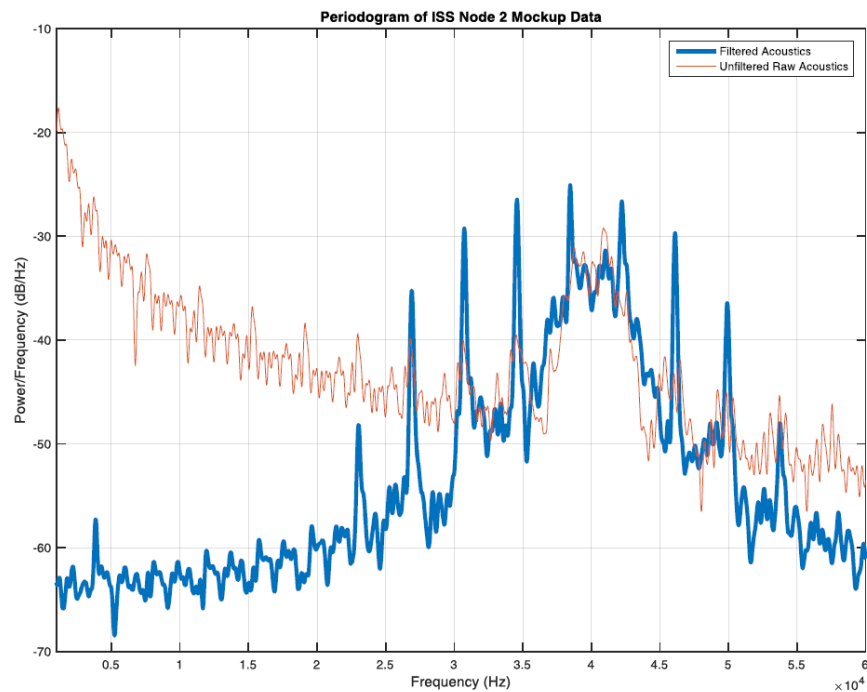


Figure 3.13. Comparison of filtered and unfiltered received signals with source present [58].

data. Analysis will include the localization results, general frequency spectrum observations, and spectrogram observations.



Figure 3.14. HTV-6 a.k.a. Kounotori 6 released from the ISS [54].



### 3.7.1 ISS Test Setup

To test the prototype a set of locations were chosen that may allow the detection of leaks or open events. **While deployment on the exterior wall would have been the preferred location, this was not feasible due to the amount of resources required to do so. This resulted in a deployed orientation where each box was "aimed" at a potential source location. The prototypes were setup independently with one for each location. Each prototype box was oriented such that the box would be close enough in proximity and the sensors directed toward their respective location.** For a given test, each prototype would be turned on for a set amount of time. Once the test was over, the prototypes would be removed from their positions, recharged, and await the next test.

#### 3.7.1.1 Deployment Locations

Three locations were chosen that may best provide leak data for the prototypes. These locations are all near hatches that may be opened at some point during regular operation on-board the ISS. Schedules of activity is well documented and mostly planned in advance so it is possible to associate events related to these hatches with data collected. The three locations include:

1. US Node 1 Zenith Airlock Footbridge (see Fig. 3.15)
2. US Node 1 Nadir Airlock Footbridge (see Fig. 3.17)
3. US Node 2 Nadir Columbus Footbridge (see Fig. 3.16)

#### 3.7.1.2 Test Setup

Deployment was separated into two tests or ACTs with the prototypes each deployed to one of the listed locations. After the first ACT the devices were recharged and then redeployed for the second ACT. An unscheduled third ACT was also conducted in an attempt to capture the HTV-6 Departure. Table 3.2 is a record of deployment for all ACTs.



Figure 3.15. Payload deployed on Node 1 Zenith Airlock footbridge.



Figure 3.16. Payload deployed on Node 1 Nadir Airlock footbridge.



Figure 3.17. Payload deployed on Node 2 Nadir Columbus footbridge. (Note the reversed placement for ACT1.)

Table 3.2. ACT deployment of Payloads.

Location	ACT1	ACT2	ACT3
Node 2 Nadir Columbus Footbridge	Box 2	Box 1	N/A
Node 1 Zenith Airlock Footbridge	Box 3	Box 3	N/A
Node 1 Nadir Airlock Footbridge	Box 1	Box 2	Box 2

### 3.7.2 Data Analysis

Data in the form of both source estimates and raw samples were retrieved via down-links after each test. Raw data was run through the same procedure as the device executes on a PC to confirm proper operation of the prototype. Source estimates were processed through the tree-search algorithm to narrow in on possible leak locations. Since there was no readily accessible pool of previous data it is hard to set any kind of threshold for the algorithm. A general study of the data was also conducted to compare testing done on the mockup and possibly gain some information on the environmental acoustics.

It should be noted that there was a physical issue with one of three prototypes sent that was most likely caused by a shorting of the sensors. This lead to no usable data at its locations during all ACTs including the third ACT of which it was the only device deployed. The short would most likely have occurred between testing and shipping.

#### 3.7.2.1 Localization Results

The possible leak locations of each test and working box combination can be seen in the following four figures. **Due to the deployment location not being on the surface and the linear orientation of the sensor arrays, each estimate refers to a line of possible locations out-of-plane.** Since there is no known leaks in the area of interest and the noise level is unknown, the estimates provided by these analyses can not currently be confirmed accurate. Without knowledge of existent leaks and a base noise level, a

threshold for the algorithm can not be set accurately and is left at a very low level. This data may be used as a noise profile for future deployments.

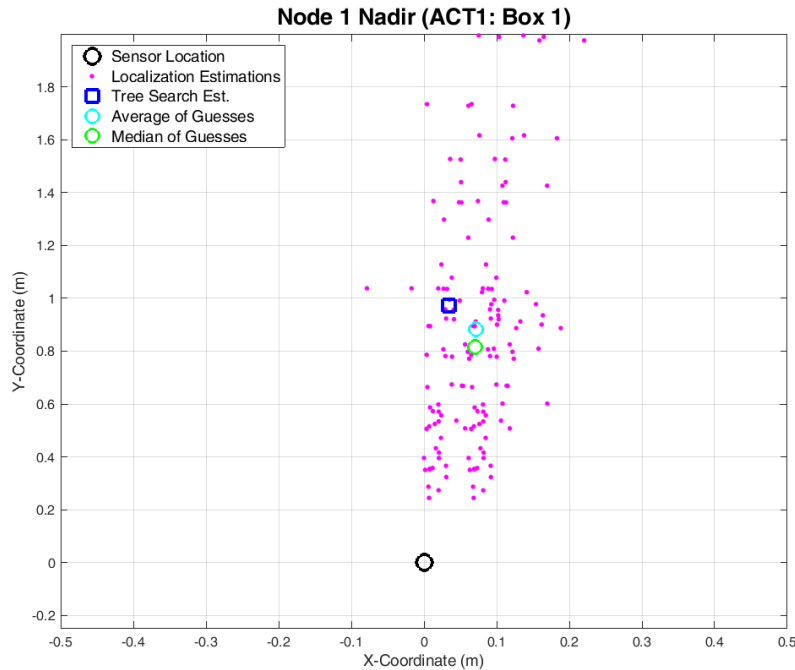


Figure 3.18. Raw guesses and calculated estimates for Node 1 Nadir location.

There is only one set of estimations that occur in the same location due to the failure of Box 2. This is for Node 1 Zenith footbridge. Comparing these estimates seen in Figure 3.20 and Figure 3.21, there is consistency in the angular direction within  $2^\circ$ .

Due to a lack of access to an accurate schematic of the nodes used as testing locations, it is currently not possible to map the calculated leak estimates to actual three dimensional locations. The use of public mockups and/or designs along with collected photographs will have to suffice. The fact that the overwhelming majority of localization estimates are in the first quadrant of the x-y plane is of interest. The directionality of the boxes was towards areas likely to source leaks which may account for the relatively small deviation from the y-axis. While overlaying this data on accurate maps has not been done, the dimensions can be approximated from images of the deployment locations. Based on the

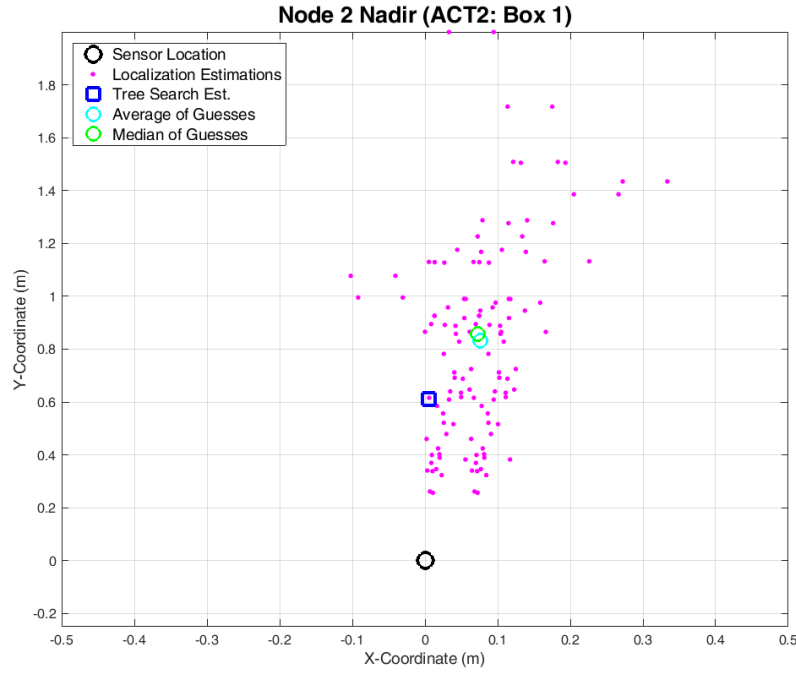


Figure 3.19. Raw guesses and calculated estimates for Node 2 Nadir location.

relative distance from the sensor the approximation, the estimated source location would exceed the boundaries of the structure. This may be due to a reflection of the detected leak's location, or there is no leak and the location is the result of the algorithm's low threshold. Overlaying a complete and accurate map with the estimates may yield a definitive result and is set for future work

### 3.7.3 Frequency Analysis

For "naked-eye observations" of the data among tests and working boxes, it is difficult to see any noticeable difference among plots with the exception of some overall amplitudes. As such, plots will only be shown for one box-test combination to reduce presentation of unnecessary figures. The power spectral density (PSD) of raw data for Box 1 during ACT 2 over the entire time can be seen in the Figure 3.7.3. Figure 3.23 shows the average of PSDs over individual runs. The most prominent points are the 550 kHz and harmonic

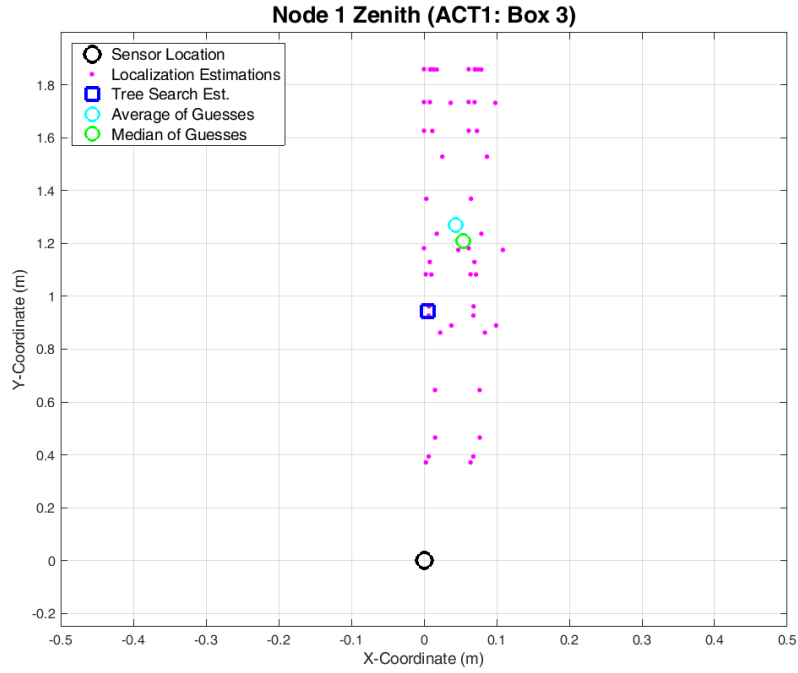


Figure 3.20. Raw guesses and calculated estimates for Test 1 at Node 1 Zenith location.

frequencies, though it is currently unknown what the source of this frequency is. Previous analysis and tests in the mockup have focused on frequencies in the range of 40 kHz using software filtered data. Figure 3.24 shows a zoom of the entire data focusing on the range of 0 - 60 kHz. A comparison to the mockup test data is shown in Figure 3.25 showing fairly similar curves after filtering.

Finally, an analysis of the surface-borne acoustics [15] conducted in 2014 was used as a base for comparison with gathered data. Figure 3.26 and Figure 3.27 show the previous analysis spectrogram and that of the data obtained during ACT 1 and ACT 2, respectively. While data from surface-borne and air-borne acoustics can not be compared in an equivalent manner, some insight into already present noise sources may be gained. For comparison, surface-borne background noise has already been collected by Madaras in [15]. While access to the raw data could not be obtained, the spectrograms presented there will serve as a substitute. There is considerable noise present during the surface-borne test in

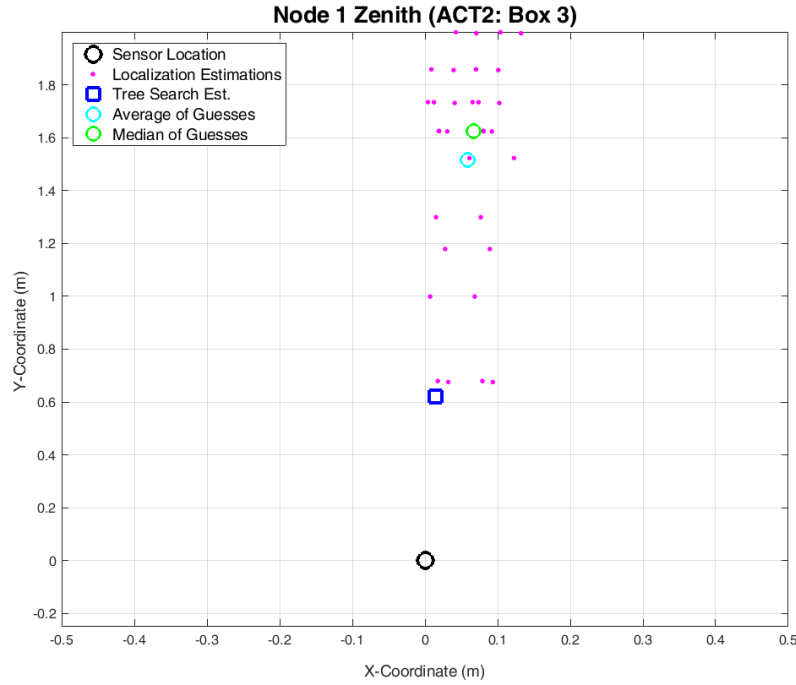


Figure 3.21. Raw guesses and calculated estimates for Test 2 at Node 1 Zenith location.

the region of 5-15 kHz, whereas the air-borne shows only a small portion of noise below 5Hz. The cause of this discrepancy has not been verified. There are three significant factors of which one or any combination of them may be the cause. First, the difference in acoustic attenuation is most likely a strong contributor dependent of course on the materials in use. While higher frequencies are expected to attenuate faster than lower ones, the better propagation in air should allow for the noise observed in the surface-borne run to also be visible in the air-borne test. It may be that the difference of location in which the tests were conducted led to source(s) not present during the air-borne test. Lastly, sensors used may have had significantly different sensitivity-frequency curves. Verifying the source of this discrepancies is left as future work.

### 3.8 Summary of Contribution

A complete flight-ready prototype of leak localization hardware was designed, built, and tested both in laboratory and on a mock-up. The main hardware included a set of sensor arrays with a wider frequency range than that of the proof of concept experiments described in Section 2.3, ADC circuitry for acoustic data collection, and a processing unit tasked with generating possible source locations based on raw data and managing storage of guesses and raw data. The prototype has been designed to operate continually for at least 24 hours enabling the collection of a wide range of expected situational noise environments. The device was first tested in a laboratory environment to verify proper function. Later testing at the mock-up location showed expected operation in an environment more representative of the deployment location. This working prototype served as the next step in implementing a true wireless automated leak detection system.

Two of the three flight-ready prototypes were successfully deployed in their respective locations on Node 1 and Node 2 of the ISS. Data from the working prototypes were properly recorded and transmitted back to ground for post-processing. Frequency and spatial analysis showed consistency among all tests with mock-up preflight tests without a simulated leak. Results from applying the tree-search algorithm show either the detection of a reflection of the leak source or the nonexistence of any source. If a leak was not recorded, the raw data could provide a base for expected background noise and further help in setting a threshold value for the algorithm in future deployments.



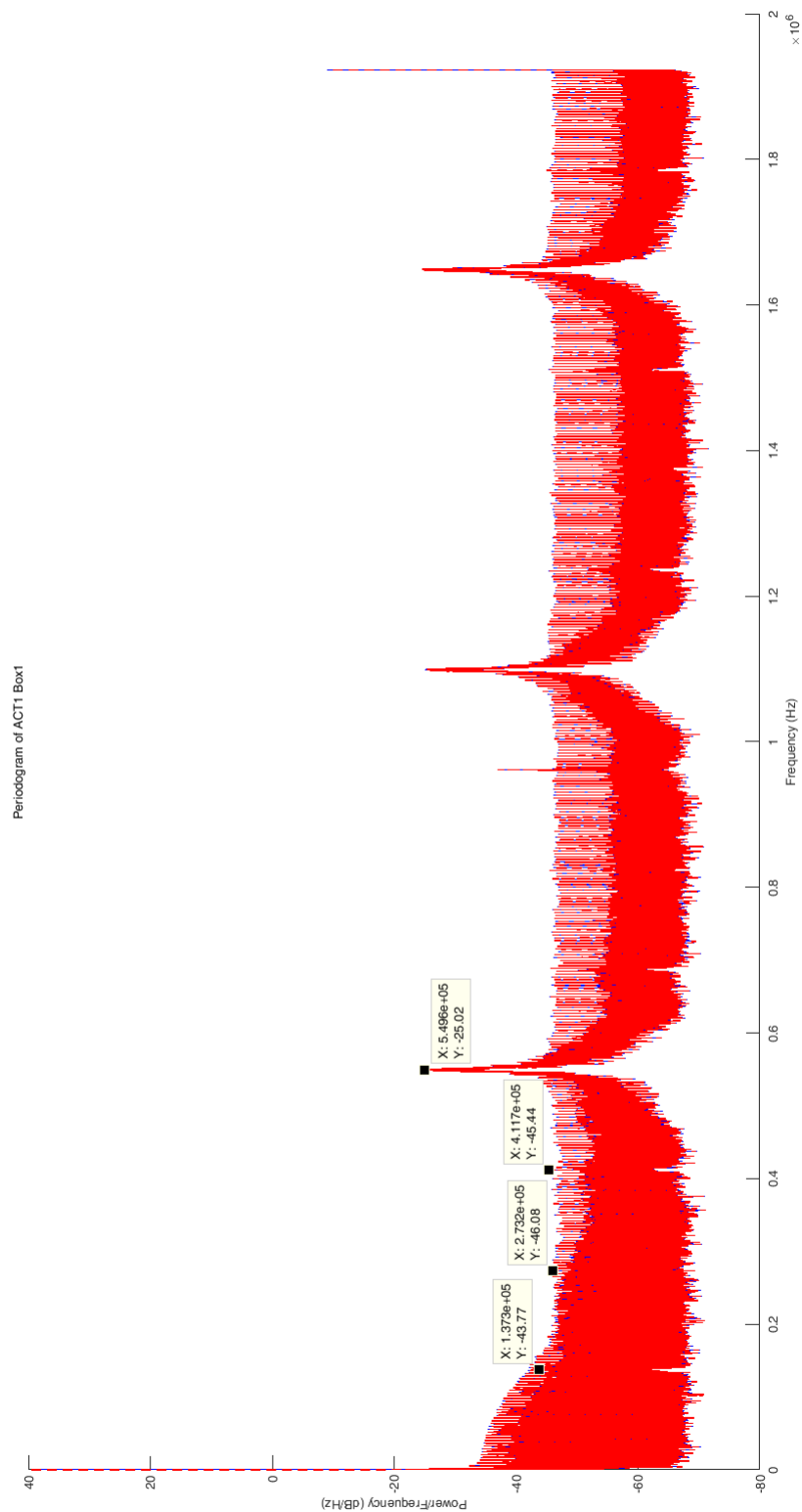


Figure 3.22. PSD of raw data for Box1 during ACT1 representative of both functioning boxes and tests.

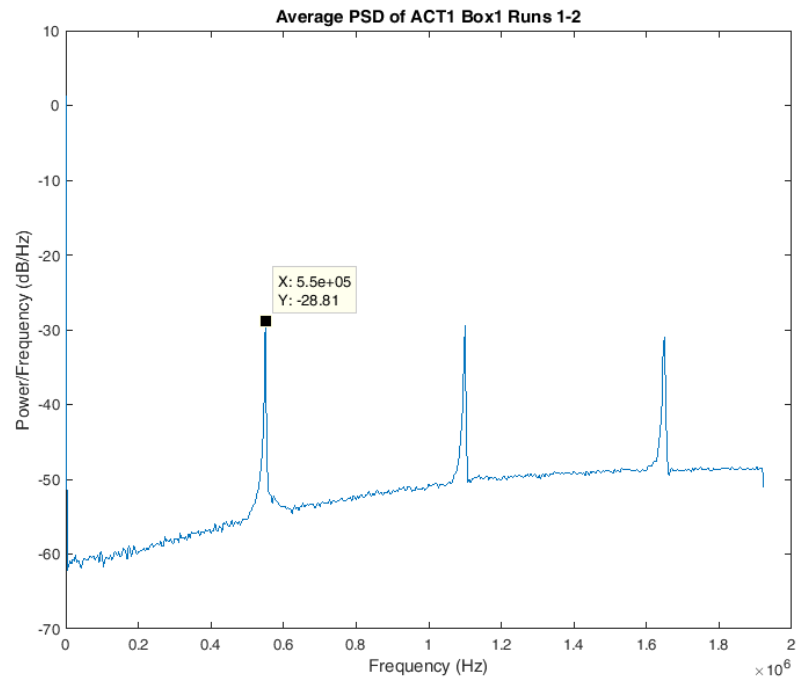


Figure 3.23. Average PSD across runs using data from Box1 during ACT1.

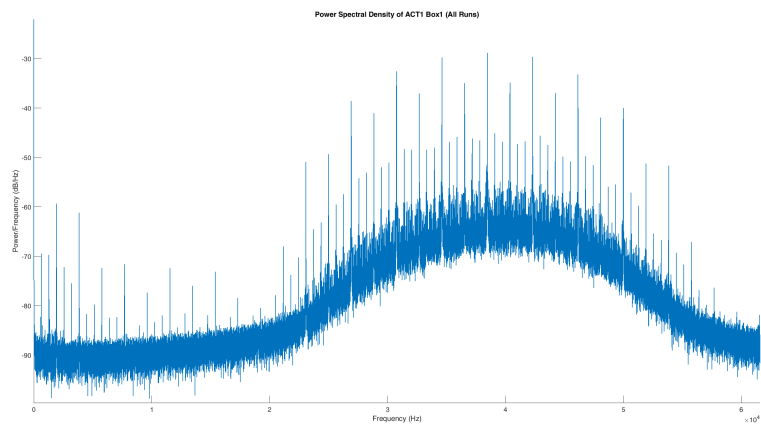


Figure 3.24. Zoomed 40 kHz focus of filtered data from Box1 during ACT1.

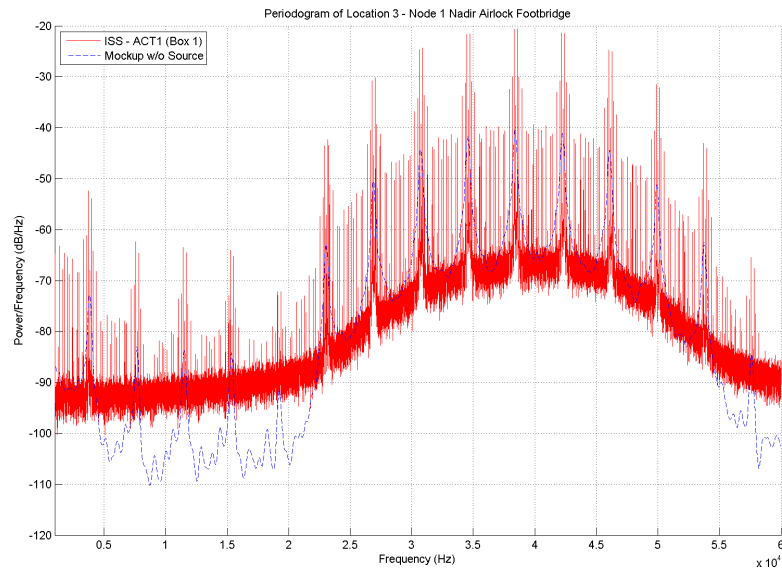


Figure 3.25. Comparison of filtered PSD between data from Box1 during ACT1 and relative mockup location.

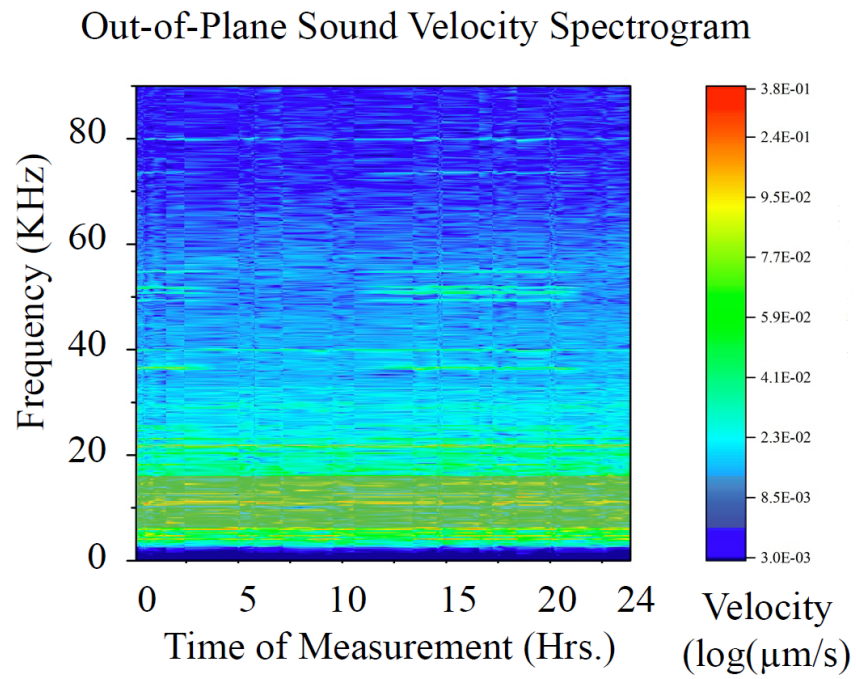


Figure 3.26. Spectrogram from surface-borne acoustic analysis.

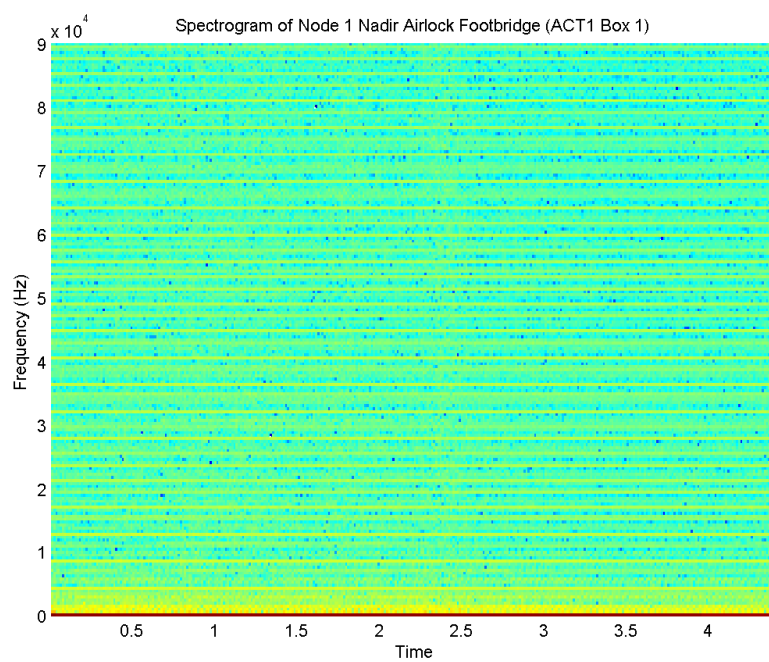


Figure 3.27. Spectrogram of the air-borne acoustics from ACT 1 and ACT 2.

## CHAPTER 4

### REFLECTION SIMULATION

One of the major contributors to location estimation inaccuracy is the presence of interference, specifically from reflections of source signals on surfaces in proximity to the leak source and detection system. In order to validate the need for compensation from this source of error, an analysis of the effects it has on the system is conducted with research covering the different parameters' effects.

An example of a possible scenario can be seen in Figure 4.1 where the source and receiver locations represented by the blue and red circles, respectively, are between two parallel surfaces. While this scenario would lead to essentially infinite reflections the figure only shows the first three signal path types. The first is line of sight (LOS) denoted as  $x_0$ , the second is the single reflect point denoted by  $x_1$  and  $x_2$ , and the third denoted as  $x_3$  is one of the possible paths that reflects off both surfaces once each.

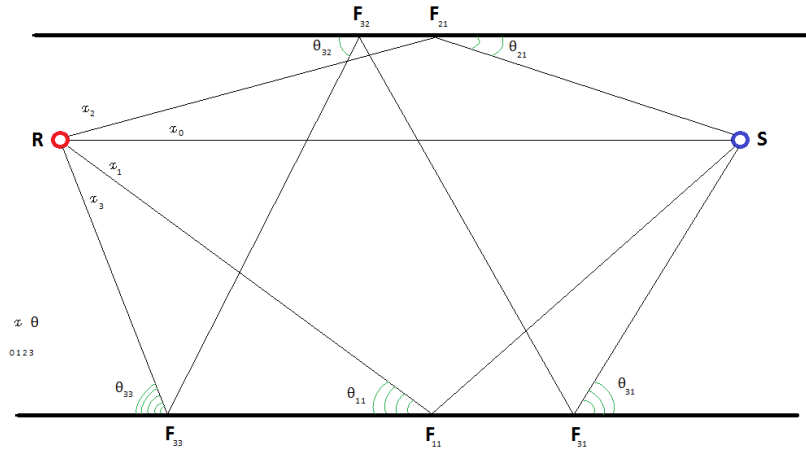


Figure 4.1. Example reflection scenario.

Due to differences between path distances, the strength of reflected signals received can be significantly lower due to the inverse square law corresponding to

omni-directional/spherical propagation. The type of surface that the signals are reflecting off of may also attenuate the signal depending on its reflection coefficient. The surface's coefficient may also have an imaginary component that introduces phase effects to the signal.

As a formal definition of the scenario, let  $\bar{S}(t)$  be the signal emitted by the source in the time domain, and let each of the signals received previously mentioned be denoted by  $x_j$  where  $x_0$  specifically refers to the LOS signal. The received signal will simply be

$$\bar{R}(t) = \sum_{j=1}^n x_j \quad (4.1)$$

where  $x_j$  can further be expressed as

$$x_j = G_j * \bar{S}(t - t_j) + w_j. \quad (4.2)$$

Here  $G_j$  and  $t_j$  are the gain or attenuation and the time or phase shift associated with the  $j^{th}$  path. Also, the additive noise is denoted by  $w_j$ .

Given the total distance the path travels denoted by  $d_j$  and the attenuation due to the reflection off the  $k^{th}$  surface on the  $j^{th}$  path denoted by  $A_{j,k}$ , the gain for path  $j$  is defined as

$$G_j = \frac{1}{4\pi d_j^2} \alpha(d_j) \left( \prod_{k=1}^m |A_{j,k}| \right). \quad (4.3)$$

Another term included is the acoustic attenuation labeled as  $\alpha$ , which is dependent on more than just the path distance as implied by this equation. This is a simple case of using the approximate attenuation rate given the source frequency and conditions similar to those near sea level. In the same manner, the time shift can be expressed as

$$t_j = \frac{d_j - d_0}{c} + f \sum_{k=1}^m \angle A_{j,k} \quad (4.4)$$

where  $f$  is the signal frequency, and  $c$  is the speed of sound (assumed to be similar to that near sea level at 1 atm). As a note, the method for finding the delay due to the phase shift

relies on the frequency of the signal and will have a more complex effect on a real signal with a range of frequency components. Derivations can be seen in Appendix A.

The specific scenario that will be explored is described as follows. A sensor array will be simulated using the prototype dimensions aligned on a 2 dimensional space. The source will be represented as a point-source emitting an omni-directional 40 kHz signal. Since the largest effects of interference are the focus, simulations will involve only the first reflection off a single surface interfering with the LOS signal. Points of interest are on the relation between AOA error and the relative distance of a surface to the receiver and between error and reflection coefficient.

#### 4.1 Simulation Method

To observe the effects of reflections, a MATLAB script capable of simple two dimensional simulation was created. Using this simulation of earliest reflections, the approximate error from largest effects of interference in a simple setup can be studied. This setup uses a simulated source similar to that used in physical testing of the hardware. The receivers are equivalent in spacing to the microphone arrays used in the deployed prototypes.

Two dimensional analysis is comprised of setting the receivers and source at given locations and then including a surface that can be represented using a simple equation. Runs of different sensor locations and distances between receivers and surface are done to cover a wide range of angles. Figure 4.2 shows a small example of what the setup looks like with the horizontal lines representing the different surfaces, the black x's showing test locations for the source, and finally the red x's to show the receiver locations. Note that the receiving array's location does not move and the individual receivers are as close as they were physically deployed so they appear as a single x.

The received signals are used as input for computations similar to deployed initial simulations to calculate just the source's bearing angle and then compared to the true

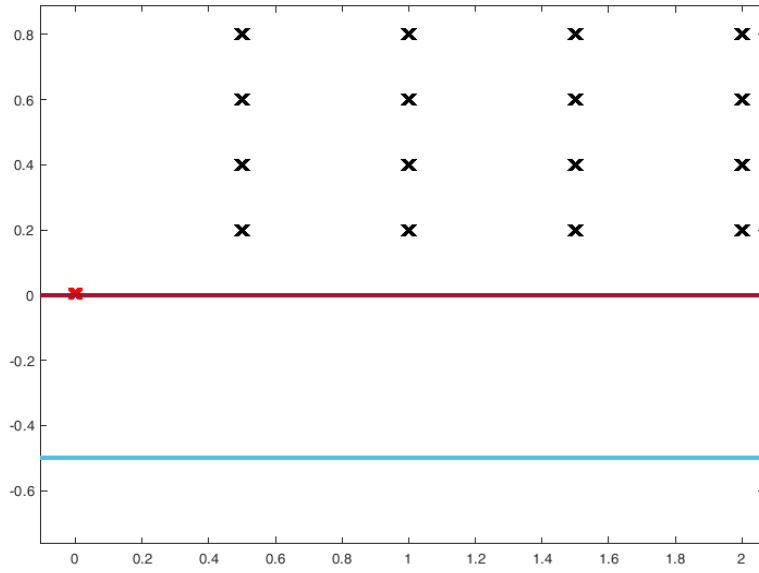


Figure 4.2. Sample setup for reflection simulations.

AOA. This will be the measure of accuracy for further analysis. Due to the wide range of angular error that may occur, a limit or threshold is set such that plots show meaningful data. The usual threshold is  $5^\circ$  unless otherwise noted. This is to mirror the bearing angle used in previous localization simulations. The general process of the script can be seen in Figure 4.3.



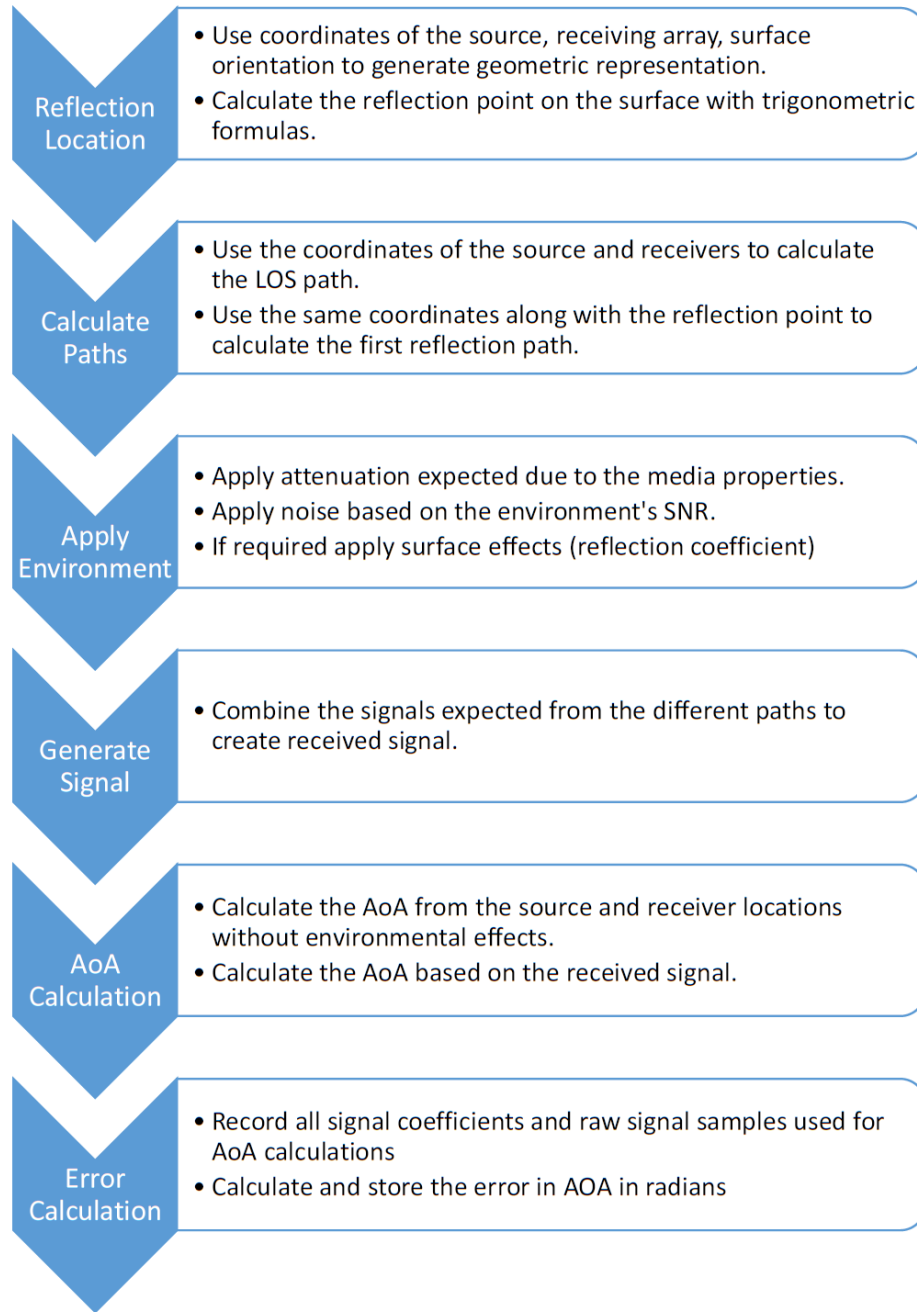


Figure 4.3. Brief overview of the processes used in the simulation method.

For these simulations, the following assumptions are made or enforced. The receivers are truly omni-directional; the receiver's angular sensitivity can be set but has not been fully implemented. All acoustics are traveling through a medium similar to air at sea level.

There is no frequency shifting of any kind though implementable if desired. Each scenario will have its own set of parameters in addition to those listed above. For example, in the spatial analysis, the surfaces are perfect acoustic reflectors to simulate the worst case scenarios though specific reflection coefficients will be analyzed in a later scenario.

The range of input data used for simulation are as follows. The receivers are centered on the origin and in a vertical orientation. Source locations are modeled in the first quadrant and surfaces are effectively in the fourth quadrant. Surfaces are set as horizontal lines to simplify calculations while representing common real-life obstacles. The area of interest represented by the source locations is an area of  $2 \text{ m}^2$  with the center at (1,1). The horizontal distance from the receivers to the surface ranges from 0.1 m to 3 m.

#### 4.1.1 Path Finding

For these simulations it is necessary to find paths that the source signal will travel to the receiver. Given the source and receiver locations, it is straight forward to calculate the direct LOS path. Given a surface, it is possible to use trigonometry to find the reflected path. The derivation of the algorithm for finding a reflection point on a surface in a single surface scenario can be seen in Appendix B. This method assumes no scattering or frequency shifting effects on the part of the reflection surface. Furthermore, the surfaces are assumed to be completely smooth with a uniform reflection coefficient.

As a general overview for a single surface, the algorithm will use locations of the source, a receiver, and the surface to calculate additional points on the surface that will create two tangent triangles. The critical point where the triangles connect defined as the reflection point for the path is calculated using simple trigonometric properties. Once this point is calculated it's straightforward to find the path distance and time delay.

## 4.2 Spatial Simulation

For the introductory analysis, the focus is on the surface's relative distance from the source. To focus on the distance, SNR is kept relatively high and the reflection coefficient is maximized. Specifically, the SNR is set to 10 dB and the reflection coefficient is set to a value of 1 to maximize the reflections' effect on error. The full analysis will be over the area of interest described with a resolution of 1 mm<sup>2</sup>. Surface distances will be over the given range in increments of 10 cm starting 10 cm from the receivers.

### 4.2.1 Spatial Simulation Results

Figure 4.4 show the worst simulated scenario, a surface within 10 centimeters of the receivers. This set of parameters results in the reflected signal attenuating very little and providing significant power to the received signal. As such the only AOAs detected accurately within the threshold are those where the surfaces result in reflections relatively in-phase with the LOS signal akin to being on a Fresnel zone. The simulated points under threshold make up over 30% of the data for this surface distance. Figure 4.5 is closer to a realistic scenario with the surface being 1.5 m vertically distanced from the receivers. Error over the threshold makes up approximately 14% of the area simulated. The error under threshold seems to tend toward about 12.5% as seen in Figure 4.6. A graph of error over the threshold across simulated distances can be seen to show the same in Figure 4.7. This is likely the best scenario that is probably encountered in deployment of hardware.

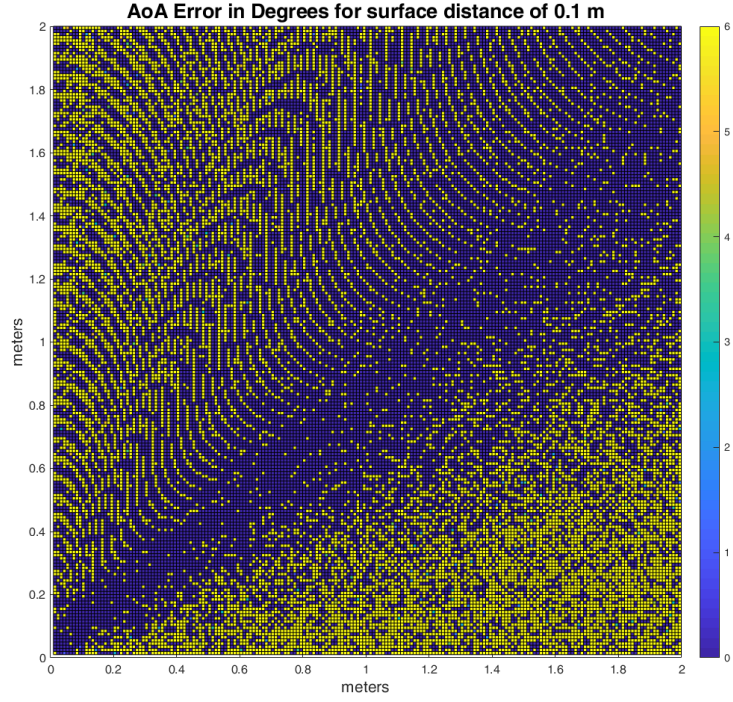


Figure 4.4. AOA error in area of interest for surface distance of 0.1 m.

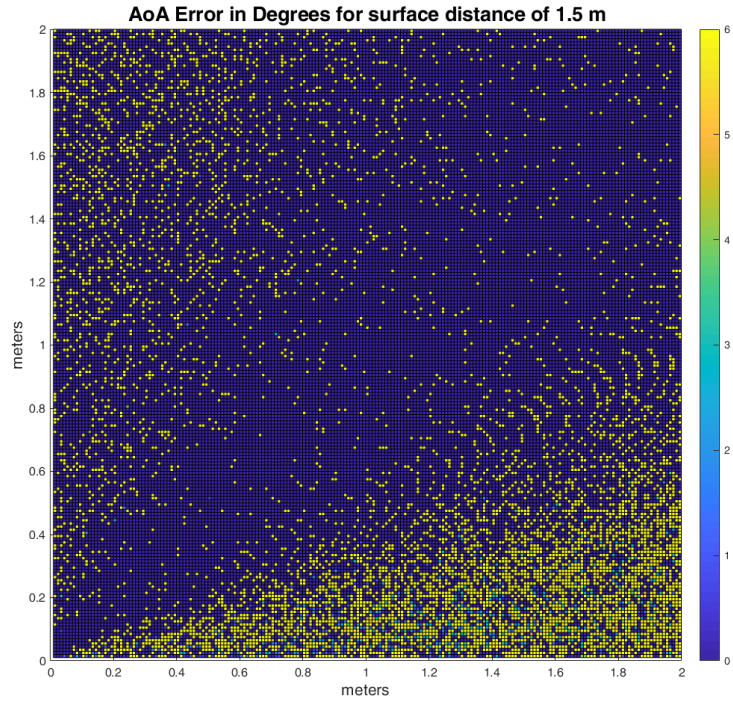


Figure 4.5. AOA error in area of interest for surface distance of 1.5 m.

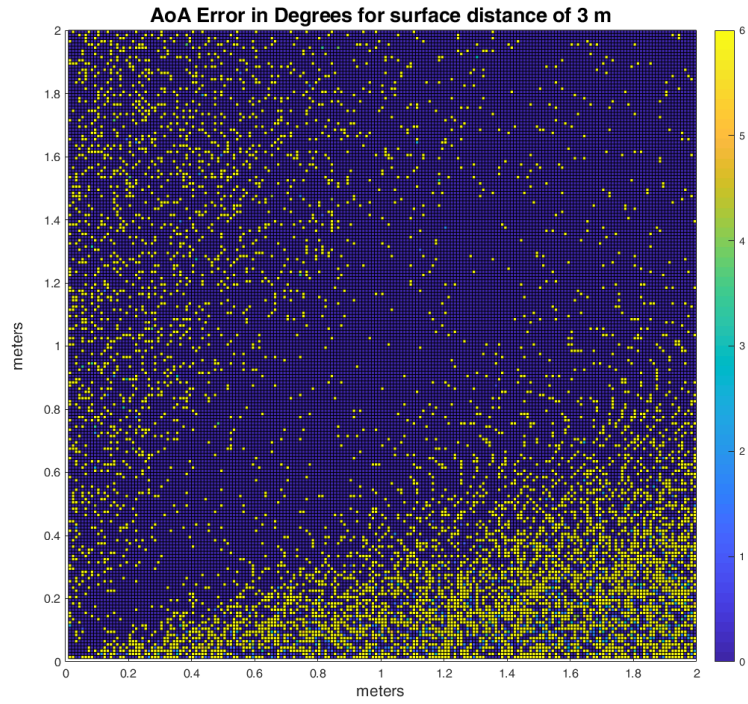


Figure 4.6. AOA error in area of interest for surface distance of 3.0 m.

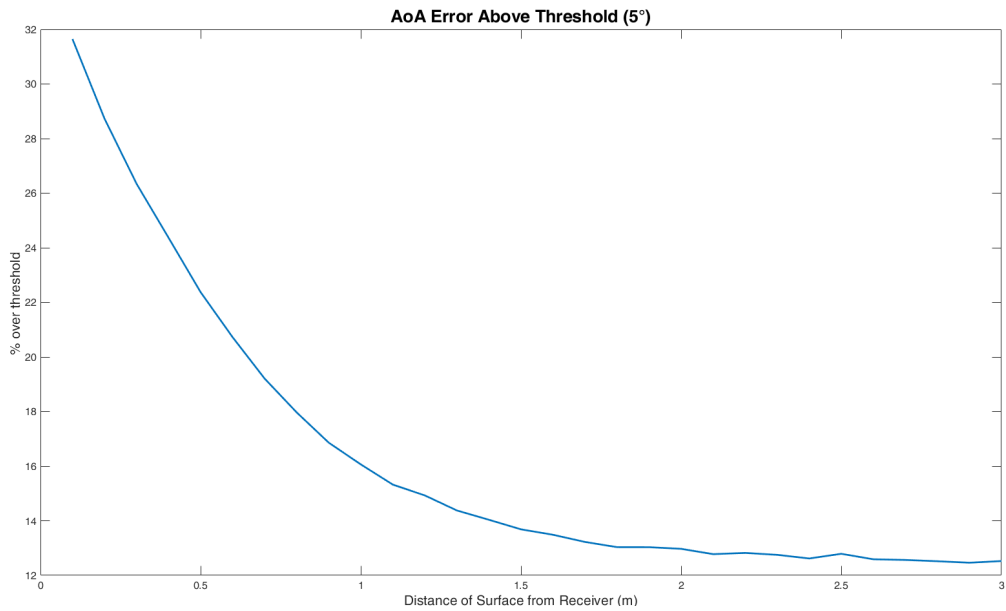


Figure 4.7. AOA error over threshold across surface distances.

While expected error of 32% of the interest space is already significant, this is only the effect of earliest reflections. It should also be noted that the area of interest simulated includes locations beyond the suggested range of the prototype previously discussed and future prototypes.

### 4.3 SNR Sensitivity

To determine how sensitive the method is to noise, an analysis across a range of SNR is performed. For the first scenario, the surface is removed to get the raw effect of SNR on the AOA error. This analysis has a reduced resolution of 5mm for the area of interest. The range of SNR values are from 0 - 10 dB to cover poor to extremely good signal strength.

The second scenario show how SNR affects the error when a surface is present. For this scenario, the same SNR range is used, but the reflection coefficient is left at complete reflection. The area of interest has the same resolution, and the surface distance has the same range.

#### 4.3.1 SNR Sensitivity Results

The SNR has a strong effect on the accuracy of the AOA calculation as seen in Figure 4.8. At 10 dB the error over threshold is as high as 13% and up to 28% at 0 dB. Error does not fall below 5% until over 20 dB which is an unlikely level of scenario. The presence of a reflecting surface is predicted to only increase the error rate.

The first graph of Figure 4.9 show the combined effect of the SNR and a completely reflecting surface at varying distances. Each line represents a different SNR value. As the SNR increases, the error rate falls, but the rate at which it falls is of interest. At every distance there is some level of diminishing returns when it comes to the decrease in error compared to the required increase in SNR. This can be seen most clearly in the close quarter surfaces where the surface affects accuracy to a greater degree. The second graph makes this a bit clearer to see as several changes in error rate at distance over SNR is

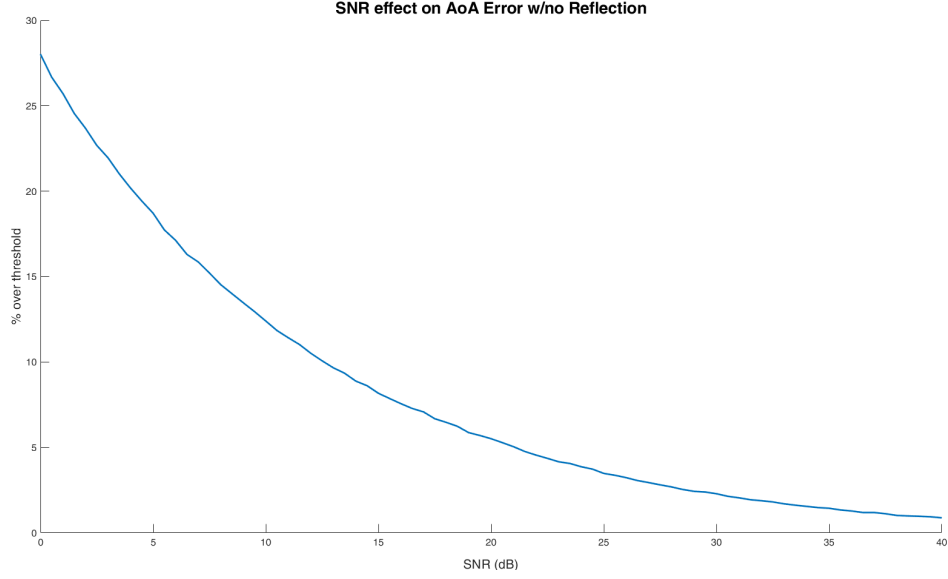


Figure 4.8. Rate of exceeding threshold relative to SNR without a reflecting surface.

shown. The efficacy of reducing the reflection coefficient decreases as the distance from the surface decreases. This is likely due to the natural attenuation of longer paths increasingly lowering the power of the reflected signal. Note that for surface beyond 1m in distance, the error rate improvement is in a similar range from 1-2% as SNR decreases.

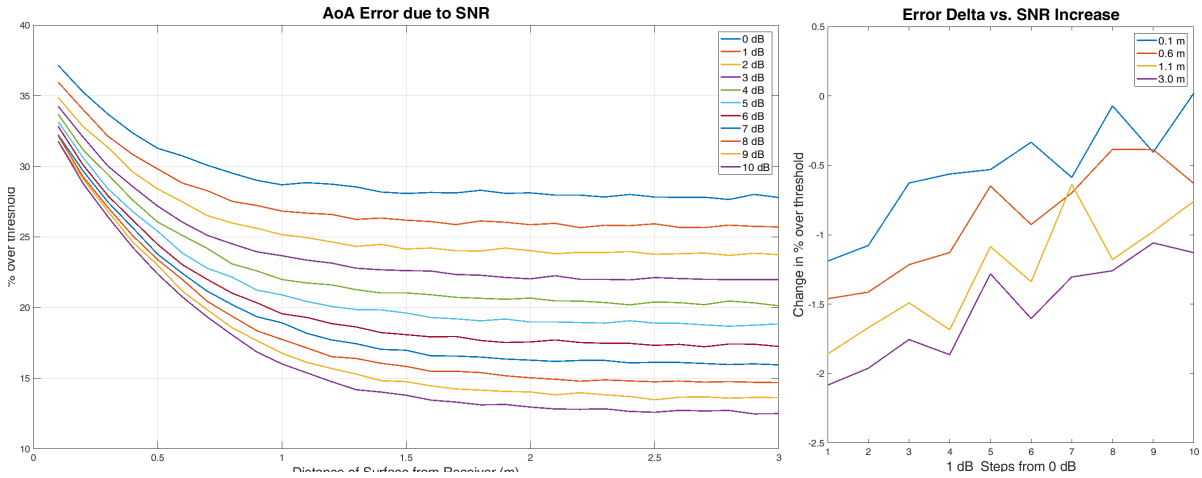


Figure 4.9. Rate of exceeding threshold relative to SNR with a surface reflection coefficient of 1.



## 4.4 Reflection Coefficient

The ability to alter the acoustic reflection coefficient of surfaces leads to an interest in that coefficient's effect on the AOA error. A range of coefficients, both real and complex, are chosen along and within the unit circle to cover most types of surfaces. The SNR was left at 10 dB to focus more on the reflection interference. The ranges of the surface distances and the area of interest remain the same but the resolution is smaller to lower simulation time. For the surface distance, the resolution is 10 cm, and for the area of interest, it is 10 mm.

### 4.4.1 Reflection Coefficient Results

Figure 4.10 shows an array of simulated complex coefficients for a single distance of 0.1m from the receiver and with 100 dB SNR. As we can see from this figure, magnitudes of the reflection coefficient seem to affect the error rate a great deal more than the phases.

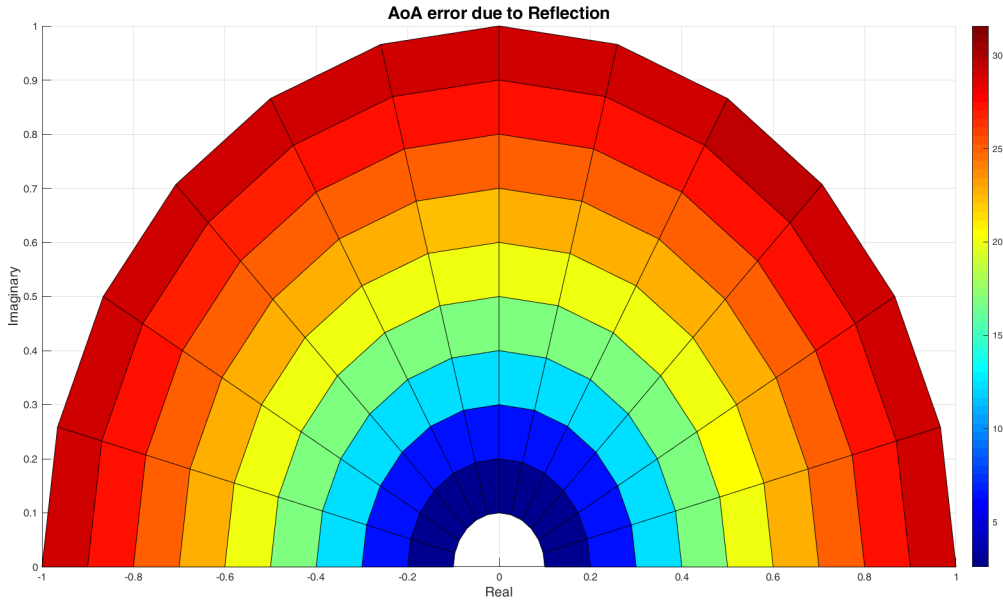


Figure 4.10. Rate of exceeding threshold relative to the reflection coefficient.

A snapshot of a single magnitude with multiple phases over the range of distances shown in Figure 4.11 illustrates this seeming independence from the surface distance as



well. There is no true independence, but the effect of phase is negligible regardless of the surface distance or the magnitude of the reflection coefficient as shown in Figure 4.12. This is to be expected since the phase component will shift all the reflections by the same amount. Since the simulated signal is a simple sinusoidal wave, the phase shift is simply cyclic and phase shifts moving points out of the threshold level are counter balanced by an equivalent or near-equivalent number of points moved under said threshold. A more complex and realistic signal may yield different results.

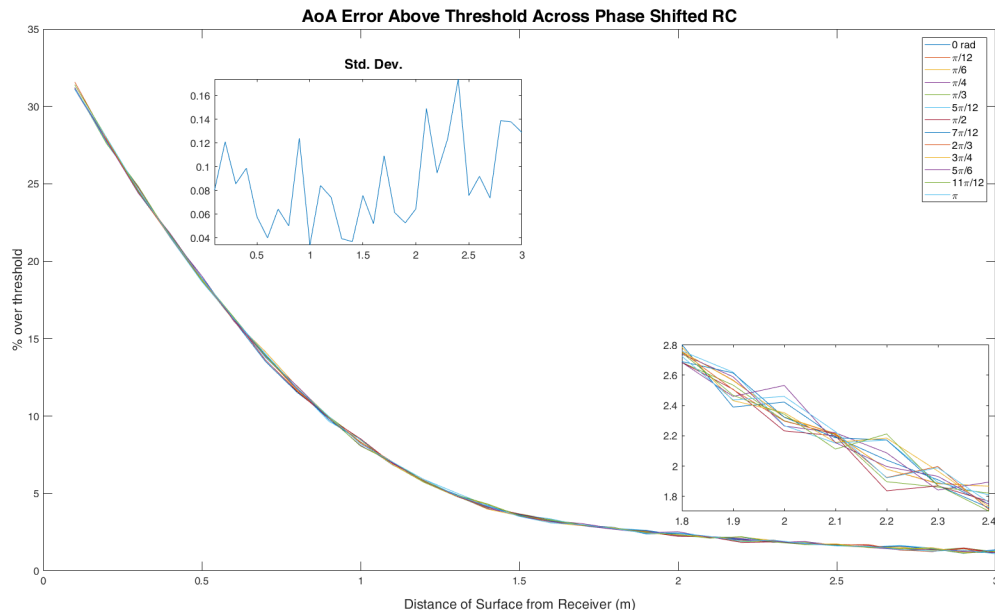


Figure 4.11. Error rate for single simulation with equal magnitude and variable phase.

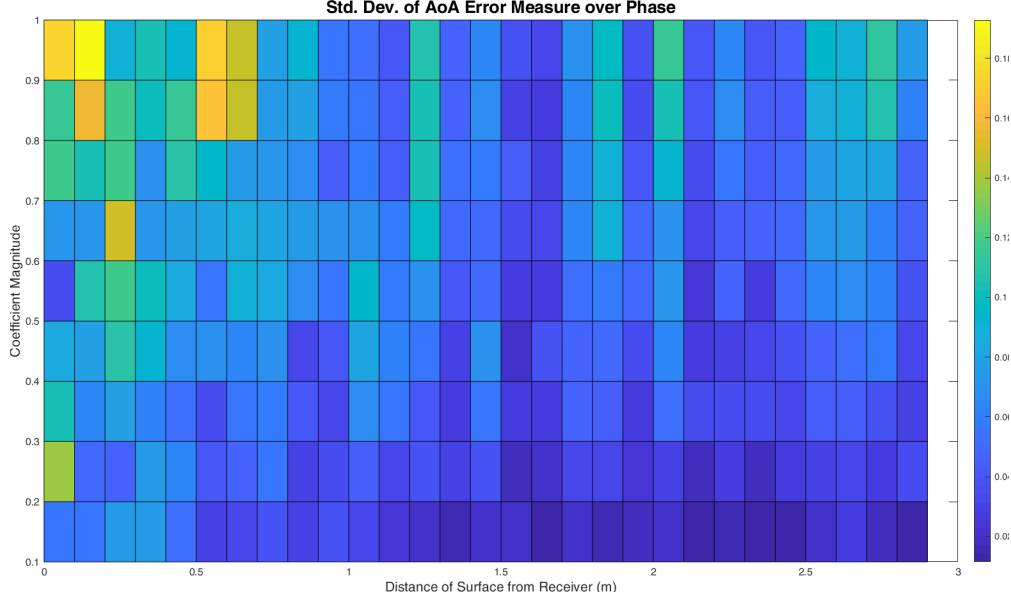


Figure 4.12. Standard deviation of error rate relative to the phase shift component of reflection coefficient.

Due to the minuscule effects of the phase component, study was focused on the just the magnitude of the reflection coefficient. The error rate across phases for a given magnitude are averaged to produce the magnitude data. These error rate averages can be seen in the first part of Figure 4.13 where the second part illustrates the change in error rate as the magnitude is increased at several distances. Like in the SNR analysis, the one meter mark seems to be an approximate threshold for accuracy. Surface distances greater than 1.1m yield less than approximately 1% error reduction per coefficient decrease of 0.1 magnitude. Under this distance, changes in the surface's reflection coefficient magnitude will result in greater decreases of the AOA error rate; up to 5-6% change in error rate is possible.

#### 4.5 Reflection Analysis Conclusions

The following three parameters and their effects on AOA error were examined: reflecting surface distance, SNR, and reflection coefficient. Based on simulated results, the strongest contributors to error are the SNR and distance from the reflection surface.

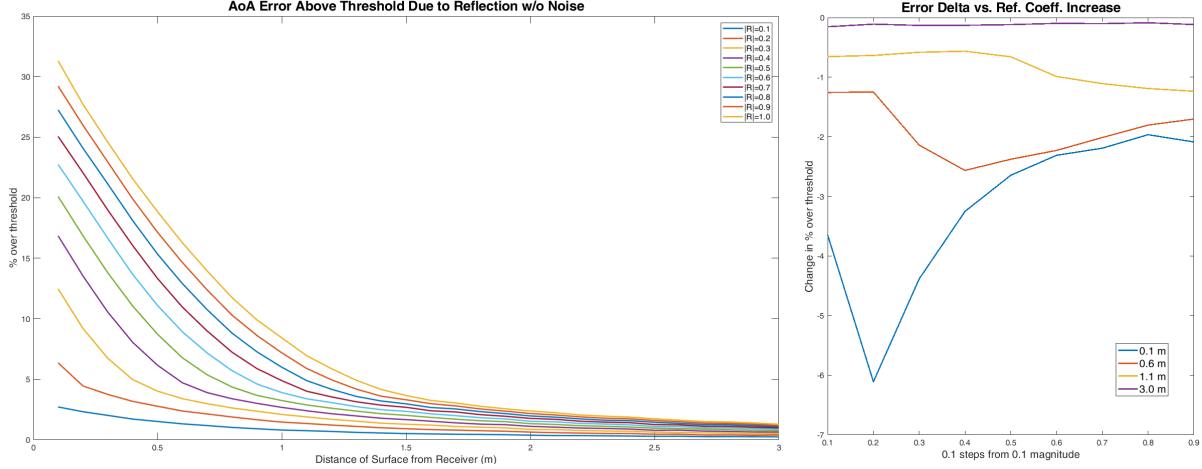


Figure 4.13. Rate of exceeding threshold relative to the reflection coefficient magnitude.

Overall, the distance has a strong correlation to error relative to the reflection coefficient and the SNR. Recall the characteristics described in Figure 4.9 and Figure 4.13. For the reflection coefficient, it is easy to confirm that at a certain distance the returns of decreasing coefficient magnitudes are greatly diminished, especially when the surface is greater than 1m away. As for the SNR, the error rate does not have a large reduction when the surface is too close to the sensor array i.e. less than 1m.

When considering the application of this data to the design of a system which the prototype hardware described in Chapter 3 may serve as a base, there are limitations in what can be adjusted. Since the strength of a source signal is not known in advance, the only way to increase SNR is to drop the noise ceiling. This would have to be considered during the design phase of the pressurized structure rather than after construction and deployment. While the SNR is not a parameter that can normally be adjusted, the distance may be increased by proper planning of sensor deployment locations. Manipulation of the surface reflections may also be implemented during construction or possibly after. Based on the surface reflection coefficient results, it could be argued that adjusting the coefficient for surfaces beyond 1-1.5m is not very effective. From the SNR analysis, the larger error reduction rates are restricted to reflecting surface distances beyond approximately 1m.

The model described in Chapter 2 is designed to function in higher error scenarios due to factors such as low SNR and multi-path by reflections. However, there may be scenarios where such processing is not an option, such as ultra-low power solutions where on-board processing is not feasible and perhaps few guesses can be generated. This section of early research can be used as the beginning of guidelines for deployment of many ultrasonic systems. While the plots presented are based on a threshold of 5, the raw data can easily be filtered to generate different guidelines for other restrictions. In general, the method developed can easily be applied to similar acoustic scenarios.

## CHAPTER 5

### CONCLUSION AND FUTURE WORK

#### 5.1 Conclusions

A low complexity tree-search technique was developed as a novel solution for both detection and localization goals using observations collected from an ultrasonic sensor network. A low complexity tree-search technique was developed as a novel solution for both detection and localization goals using observations collected from an ultrasonic sensor network. The posterior PDF of the source state is approximated only in the regions with high likelihood reducing computational complexity of a general Bayesian filtering solution. This method takes the low sound pressure of smaller leaks in high levels of background noise into consideration to address the difficulty in determining the presence such small leaks. The developed Bayesian filter handles the non-linear relation between the leak and observation state spaces using Gaussian kernels, which is justified by the Gaussian distribution function of the likelihood term used to find a path metric. The adaptive use of kernels allows for a less complex algorithm compared to other popular methods such as the particle filter and maximum likelihood probabilistic data association.

The tree-search algorithm managed to localize leaks up to 50% closer to simulated leaks than the particle filter using the same probability of observation. Extending higher probable paths translates into fewer numbers of particles to update leading to faster results. The algorithm also performed up to 4 times faster than the particle filter with a set number of particles. The experimental results compared with the simulations fairly well and did not exceed 1.5 cm further from the source than simulations.

A prototype of leak localization hardware was designed and built for the express purpose of testing the novel solution in application aboard the ISS, an appropriate pressurized space structure. The hardware included a set of new ultrasonic microphone

arrays that served as the sensing component of a sensor network necessary for the localization algorithm. The electronics platform chosen and PCB design served to properly collect acoustic audio in the ultrasonic range. The prototype was designed to record source estimates and raw data to external media for post-processing. It was also designed to operate continually for at least 24 hours enabling the collection of a wide range of expected situational noise environments. Testing prior to deployment confirmed the prototype's capabilities in both the lab setting and in an environment reflecting that of a node on the ISS.

From the flight-ready prototypes that were successfully transported to the ISS and deployed in their respective locations, data were properly recorded and transmitted back to ground for post-processing. Frequency and spatial analysis showed consistency among all tests with mock-up preflight tests without a simulated leak. These results show that the presence of a leak was unlikely based on the estimates, algorithm output, and the potential corresponding locations in the node. While no leak seems to have been recorded, the raw data provides a base for expected background noise and may help in setting a threshold value for the algorithm in future deployments.

A method of simulating leaks in various conditions and calculating AOA error was developed allowing for exploration on the effects of various physical parameters. For this work, the focus was on reflecting surfaces. Study of reflection scenarios effects on the AOA error showed strong contributions from the SNR, reflecting surface location, and reflection coefficient. All of these parameters can have a strong effect on the error individually, but when combined they provide insight on possible realistic scenarios. Of these parameters explored, distance from the surface showed promise for defining regions of effects. Given the condition parameters for measuring AOA error, results from the simulations show a boundary near 1m can be declared to differentiate low and high impact of SNR and reflection coefficient with respect to the surface distance from receivers. While plots, figures, and this boundary declaration are generated based on the 5° threshold

implemented, the methodology and simulation software can be applied to other thresholds. Additional physical parameters can also easily be added to the methods.

## 5.2 Future Work

A proper mapping of the leak estimates on an accurate model of the nodes is a necessary step in the localization analysis to verify the source existence and location. Additionally, verification of the discrepancy between air-borne and surface-borne frequency responses needs to be completed as well as origination and future elimination of the 550 kHz peaks. While the prototype hardware was verified to be flight-ready, the lack of certainty in the existence of a leak during deployment warrants another round of in-situ testing. As a first step, a testbed utilizing more realistic leak signatures from an actual pressurized structure would be a worthwhile endeavor for confirmation of proper operation. Further improvements include moving the post-processing for localization to the device, interconnectivity between the devices as a means of creating a single system, and implementing a more power efficient unit. Ideally, the tree-search algorithm should be implemented on the nodes to generate a single output – either the location of a leak or indicator of no leak. Allowing the communication between devices allows for the presence of a complete system that could simplify installation or deployment and create a single stream of output rather than one for each device. This will introduce the possible limitations of throughput and will require further analysis of the potential impact on the performance. A more power efficient prototype would allow for longer testing and in the future limit the amount of maintenance necessary for a full deployment.

For the reflection analysis work, the next steps are to add the effects of additional surfaces and moving to a 3-dimensional method. This would allow for possible modeling of a deployment location to predict the expected error and fine-tune the system. This transition to the third dimension could also be reflected in the prototype with a movement to a 2-dimensional sensor array allowing 3D localization - perhaps a circular array. While

the single test signal served as a start, real leak signals are necessary to better simulate the scenarios leading to more reliable results. Such an improvement to the algorithm would be the use of radiation patterns expected from a source point on multiple surface topologies. Also, the pure tone serving as the current test signal should be replaced with signals similar to those generated by real physical leaks. These may be done concurrently with the realistic testbed setup previously mentioned. If financially viable and time efficient, the use of finite element analysis could be a further step toward accuracy in acoustic system modeling.



## REFERENCES

- [1] Hyde, J., Christiansen, E., Lear, D., Kerr, J., Lyons, F., Herrin, J., Ryan, S.,  
'Investigation of Shuttle Radiator Micro-Meteoroid Orbital Debris (MMOD) Damage',  
50th AIAA/ASME/ASCE/AHS/ASC Structures, Structural Dynamics, and Materials  
Conference, Palm Springs, California, USA, May 2009.
- [2] Committee for the Assessment of NASA's Orbital Debris Programs; National Research  
Council, *Limiting Future Collision Risk to Spacecraft, An Assessment of NASA's  
Meteoroid and Orbital Debris Programs*, The National Academies Press, 2011.
- [3] Lear, D., Hyde, J., Christiansen, E., Herrin, J., Lyons, F., 'STS-118 Radiator Impact  
Damage', *Orbital Debris Quarterly News*, 12, (1), January 2008.
- [4] @NASASpaceflight (Chris Bergin). "ISS Leak summary." Twitter, Sep.3, 2018, 1:50  
p.m., <https://twitter.com/NASASpaceflight/status/1036672731809566720>
- [5] Liou, J.C., Kieffer, M., Drew, A., Sweet, A., 'The 2019 U.S. Government Orbital  
Debris Mitigation Standard Practices'. *Orbital Debris Quarterly News*, 24, (1),  
February 2020.
- [6] Anatoly, Z., 'Mir Cosmonauts Plug Leak', in *Space.com News*, April, 20, 2000,  
[http://www.space.com/news/spacestation/mir\\_leak\\_000420.html](http://www.space.com/news/spacestation/mir_leak_000420.html).
- [7] ISS015-E-10854, 6 June 2007,  
<http://www.spaceref.com/news/viewsr.html?pid=24439>.
- [8] NASA Space Station Blog, August 2018,  
<https://blogs.nasa.gov/spacestation/2018/08/>.
- [9] Associated Press, 'Russia: Hole drilled from inside Int'l Space Station capsule',  
*APNews*, Dec. 24, 2018, <https://apnews.com/87cb3a5a3f1740eda47a0a1811f96033>.

- [10] Wilson, W.C., Coffey, N.C., and Madaras, E.I., 'Leak detection and location technology assessment for aerospace applications', NASA/TM-2008-215347, 2008.
- [11] C. Moon, W. C. Brown, S. Mellen, E. Frenz, D. J. Pickering, 'Ultrasound Techniques for Leak Detection', Tech. Rep., May 2009.
- [12] Michaels, J.E., and Michaels, T.E., 'Detection of structural damage from the local temporal coherence of diffuse ultrasonic signals', IEEE Transactions on Ultrasonics, Ferroelectrics, and Frequency Control, 2005, 52, (10), pp. 1769-1782.
- [13] J. Steckel and H. Peremans, 'Ultrasound-based Air Leak Detection using a Random Microphone Array and Sparse Representations', SENSORS, 2014 IEEE, Valencia, 2014, pp. 1026-1029.
- [14] T. Guenther and A. Kroll, 'Automated Detection of Compressed Air Leaks Using a Scanning Ultrasonic Sensor System', 2016 IEEE Sensors Applications Symposium (SAS), Catania, 2016, pp. 1-6.
- [15] E. Madaras, Studies of Structure Borne Ultrasonic Noise on the ISS, NASA Presentation, April 2015.
- [16] Holland, S.D., Roberts, R., Chimenti, D.E., and Strei, M., 'Two-sensor ultrasonic spacecraft leak detection using structure-borne noise', Acoustics Research Letters Online, 2005, 6, (2), pp. 63-68.
- [17] Holland, S.D., Roberts, R., Chimenti, D.E., and Song, J.H., 'An ultrasonic array sensor for spacecraft leak direction finding', Ultrasonics, 2006, 45, pp. 121-126.
- [18] Champaigne, K.D., and Sumners, J., 'Wireless impact and leak detection and location systems for the ISS and shuttle wing leading edge', Proc. of the IEEE Aerospace Conference, Big Sky, MT, USA, March 2005, pp. 1-8.

- [19] Champaigne, K.D., 'Low-power Electronics for Distributed Impact Detection and Piezoelectric Sensor Applications', Aerospace Conference, 2007, pp.1-8.
- [20] Lynch, J.P., and Loh, K.J., 'A summary review of wireless sensors and sensor networks for structural health monitoring', The Shock and Vibration Digest, 2006, 38, (2), pp. 91-128.
- [21] Pride, R., Hodgkinson, J., Padgett, M., Van Well, B., Strzoda, R., Murray, S., Ljungberg, S., 'Implementation of optical technologies for portable gas leak detection', Proc. Int. Gas Research Conference, IGRC, Vancouver, Canada, November 2004.
- [22] Gibson, G., Van Well, B., Hodgkinson, J., Pride, R., Strzoda, R., Murry, S., Bishton, S., and Padgett, M., 'Imaging of methane gas using a scanning, open-path laser system', New Journal of Physics, 2006, 8, (2), 26.
- [23] Liu, M., Zang, S., and Zhou, D., 'Fast leak detection and location of gas pipelines based on an adaptive particle filter', International Journal of Applied Mathematics and Computer Science, 2005, 15, (4), pp. 541-550.
- [24] Weimer J., Sinopoli, B., and Korgh, B.H., 'Multiple source detection and localization in advection-diffusion processes using wireless sensor networks', Proc. of the 30th IEEE Real-Time Systems Symposium, Washington, DC, USA, December 2005, pp. 333-342.
- [25] Lin, W., and Zhang, X., 'A novel approach for dynamic pressure transducer based pipeline leak detection', The Sixth World Congress on Intelligent Control and Automation, Dalian, China, October 2006, 2, pp. 5299-5303.
- [26] Mi, B., Michaels, J.E., and Michaels, T.E., 'An ultrasonic method for dynamic monitoring of fatigue crack initiation and growth', Journal of the Acoustical Society of America, 2006, 119, (1), pp. 74-85.

- [27] Pollock, A.A., and Hsu S.S., 'Leak detection using acoustic emission', Journal of Acoustic Emission, 1982, 1, (4), pp. 237-243.
- [28] Studor, G., 'Ultrasonic Detectors in Space', CTRL Reprint, 2002.
- [29] Sorenson, H. W., 'Parameter and State Estimation: Introduction and Interrelation'. IFAC Proceedings Volumes, 1982, 15, (4), pp. 85-89.
- [30] Torrieri, D.J., 'Statistical theory of passive location systems', IEEE Transaction on Aerospace and Electronic Systems, 1984, 20, (2), pp. 183-198.
- [31] Patwari, N., Hero, A.O., Perkins, M., Correal, N.S., and O'Dea, R.J., 'Relative location estimation in wireless sensor networks', IEEE Transaction on Signal Processing, 2003, 51, (8), pp. 2137-2148.
- [32] Le, L.B., and Hossain, E., 'Resource allocation for spectrum underlay in cognitive radio networks', IEEE Transaction on Wireless Communications, 2008, 7, (12), pp. 5306-5315.
- [33] Stone, L.D., Corwin, T.L., and Barlow, C.A., *Bayesian Multiple Target Tracking*, (Artech House, 1999).
- [34] Jacobsen, F., Juhl, P.M., *Fundamentals of General Linear Acoustics*. United Kingdom: Wiley, 2013.
- [35] Kalman, R.E., 'A new approach to linear filtering and prediction problems', Trans. ASME J. Basic Eng., 1960, 82, pp. 34-45.
- [36] Ristic, B., Arulampalam, S., Gordon, N., *Beyond the Kalman Filter: Particle Filters for Tracking Applications*, (Artech House, 2004).
- [37] Arasaratnam, I., and Haykin, S., 'Cubature Kalman filters', IEEE Transactions on Automatic Control, 2009, 54, (6), pp. 1254-1269.

- [38] Grewal, M.S., and Andrews, A.P., *Kalman Filtering: Theory and Practice*, (Prentice Hall, 1993).
- [39] Norgaard, M., Poulsen, N.K., and Ravn, O., 'New developments in state estimation of nonlinear systems', *Automatica*, 2000, 36, (11), pp. 1627-1638.
- [40] Julier, S.J., and Uhlmann, J.K., 'Unscented filtering and nonlinear estimation', *Proceedings of the IEEE*, 2004, 92, (3), pp. 401-422.
- [41] Bucy, R.S., and Senne, K.D., 'Digital synthesis of nonlinear filters', *Automatica*, 1971, 7, (3), pp. 287-298.
- [42] Blanding, W.R., Willett, P.K., and Bar-Shalom, Y., 'Multiple target tracking using maximum likelihood probabilistic data association', *Proc. of of the 2007 IEEE Aerospace Conference*, Big Sky, MT, USA, March 2007, pp. 1-12.
- [43] Simandl, M., Kralovec, J. ,and Soderstrom, T., 'Advanced point-mass method for nonlinear state estimation', *Automatica*, 2006, 42, (7), pp. 1133-1145.
- [44] Djuric, P.M., Kotecha, J.H., Zhang, J., Huang, Y., Ghirmai, T., Bugallo, M.F., and Miguez, J., 'Particle filtering', *IEEE Signal Processing Magazine*, 2003, 20, (5), pp. 19-38.
- [45] Nelson, J.K., and Roufarshbaf, H., 'A tree search approach to target tracking in clutter', *Proc. of the 12th Int. Conference on Information Fusion (FUSION)*, Seattle, WA, USA, July 2009.
- [46] Roufarshbaf, H., 'A tree search approach to detection and estimation with application to communication and tracking', *PhD thesis*, George Mason University, 2011.
- [47] Ito, K., and Xiong, K., 'Gaussian filters for nonlinear filtering problems', *IEEE Transactions on Automatic Control*, 2000, 45, (5), pp. 910-927.

- [48] Mazyza, V., and Schmidt, G., 'On approximate approximations using Gaussian kernels', IMA Journal of Numerical Analysis, 1996, 16, (1), pp. 13-29.
- [49] Roufarshbaf, H., Castro, J., Schwaner, F., Abedi, A., 'Sub-optimum Fast Bayesian Techniques for Joint Leak Detection and Localization', IET Wireless Sensor Systems Journal, To appear.
- [50] Blanding, W.R., Willett, P.K., and, Bar-Shalom, Y., 'Offline and real-time methods for ML-PDA track validation', IEEE Transactions on Signal Processing, 2007, 55, (5), pp. 1994-2006.
- [51] Gumbel, E.J., *Statistics of Extremes*, (New York: Columbia Univ. Press, 1958).
- [52] Bar-Shalom, Y., Fortmann, T.E., and Scheffe, M., 'Sonar Tracking of Multiple Targets Using Joint Probabilistic Data Association', IEEE Journal of Oceanic Engineering, 1983, 8, (3), pp. 173-184.
- [53] National Aeronautics and Space Administration, 'Reference Guide to the International Space Station,' Utilization Edition, September 2015.
- [54] Garcia, M., 'Japanese HTV-6 Released from Station', *NASA.gov*, January 30, 2107.  
[Online]. Available:  
<https://www.nasa.gov/image-feature/japanese-htv-6-released-from-station>. [Accessed: January 2020].
- [55] "ETHOS Life Support System Display," *International Space Station LIVE!*, Nov. 25, 2015. [Online]. Available: <https://isslive.com/displays/ethosDisplay1.html>. [Accessed: January 2019].
- [56] C. Clark, L. Labonte, J. Castro, A. Abedi and V. Caccese, "Wireless leak detection using airborne ultrasonics and a fast-Bayesian tree search algorithm with technology

- demonstration on the ISS," 2015 IEEE International Conference on Wireless for Space and Extreme Environments (WiSEE), Orlando, FL, 2015, pp. 1-5.
- [57] A. Abedi, V. Caccese, J. Castro, C. Clark, L. Labonte, H. Roufarshbaf, "Wireless Leak Detector for International Space Station (WiLD-ISS)," ISS R&D Conference, Boston, MA, July 2015.
- [58] Clark, C, 'Wireless Leak Detection Using Airborne Ultrasonics with Technology Demonstration on the International Space Station', Master's thesis, University of Maine, 2016.
- [59] Cheeke, J.D.N., *Fundamentals and Applications of Ultrasonic Waves*, Second Edition. Boca Raton, FL: CRC Press, 2002.
- [60] Kinsler, L.E. and Austin, R.F., *Fundamentals of Acoustics*, Fourth Edition. New York: Wiley, 2000.
- [61] Çengel, Y.A. and Cimbala, J.M., *Fluid mechanics: Fundamentals and applications*, Fourth Edition. Boston: McGraw-Hill, 2018.

## APPENDIX A

### DERIVATION OF FORMAL DEFINITION

As in the main text, let  $\bar{S}(t)$  be the signal emitted by the source in the time domain, and let each of the signals received be denoted by  $x_j$  where  $x_0$  specifically refers to the LoS signal. The received signal will simply be

$$\bar{R}(t) = x_0 + x_1 + x_2 + \dots + x_n = \sum_{j=1}^n x_j \quad (\text{A.1})$$

where  $x_j$  can further be expressed as

$$x_j = G_j * \bar{S}(t - t_j) + w_j. \quad (\text{A.2})$$

Here  $G_j$  is the gain or attenuation,  $t_j$  is the time or phase shift associated with the  $j^{th}$  path, and additive noise is denoted by  $w_j$ .

Let  $m$  represent the number of reflection points that are included on the  $j^{th}$  path. Then let  $k$  represent the  $k^{th}$  path segment such that  $d_{j,k}$  represents the distance from the  $k^{th}$  reflection point to the  $(k+1)^{th}$ . For the  $k = m$  component, the path is from the  $m^{th}$  reflection point to the receiver, and for  $k = 0$ , the component is from the source to the first reflection point. In the special case of the LOS where  $m = 0$ , the only component is plainly from the source to receiver.

Following the path from source to receiver location, the sources of attenuation are displayed in Equation A.3. Each component but the last is comprised of the acoustic attenuation in air where the factor is represented by  $\alpha$ , the loss due to spherical propagation expressed as distance ratios, and the magnitude of the reflection coefficient  $A_{j,k}$  of that surface. Clearly, the last component does not have the reflection coefficient since the path segment ends at the receiver.

$$\begin{aligned} G_j = & e^{-\alpha d_{j,0}} \frac{1}{4\pi d_{j,0}^2} |A_{j,0}| * e^{-\alpha d_{j,1}} \frac{d_{j,0}^2}{(d_{j,1} + d_{j,0})^2} |A_{j,1}| * \dots \\ & * e^{-\alpha d_{j,m}} \frac{(d_{j,1} + \dots + d_{j,m-2})^2}{(d_{j,1} + \dots + d_{j,m-1})^2} |A_{j,m-1}| * e^{-\alpha d_{j,m}} \frac{(d_{j,1} + \dots + d_{j,m-1})^2}{(d_{j,1} + \dots + d_{j,m})^2} \end{aligned} \quad (\text{A.3})$$



Due to the simple multiplicity for total gain, the products can be grouped into the components mirroring the three sources of attenuation. For simplification the occurrences of sums from  $d_{j,0} \dots d_{j,m}$  will be replaced with  $d_j$  which is equivalent to the total distance of the  $j^{th}$  path. This simplification is expressed as

$$G_j = \frac{1}{4\pi d_{j,1}^2} \left( \prod_{k=1}^{m+1} e^{-\alpha d_{j,k}} \right) \left( \prod_{k=1}^m |A_{j,k}| \right) \frac{d_{j,1}^2}{(d_{j,1} + d_{j,2} + \dots + d_{j,m+1})} \quad (\text{A.4})$$

where

$$\prod_{k=1}^{m+1} e^{-\alpha d_{j,k}} = \exp \left( -\alpha \underbrace{\sum_{k=1}^{m+1} d_{j,k}}_{d_j} \right). \quad (\text{A.5})$$

Since only a simple signal is being modeled, the components of temporal shift is composed of only the phase shifts from reflection coefficients and the delay from the longer path. The surface coefficient effects are represented by the sum of each phase component. The delay from the different path length is simply that change in distance divided by the speed of sound in the medium represented by  $c$ .

$$t_j = \frac{d_j - d_0}{c} + \sum_{k=1}^m \angle A_{j,k} \quad (\text{A.6})$$

## A.1 Attenuation Factor

The attenuation factor defined previously as  $\alpha$  is calculated from Stokes's law of attenuation [60, 59]. The formula used is

$$\alpha = \frac{\omega^2}{2\rho_0 c^3} \left( \frac{4}{3}\eta + \eta_B \right). \quad (\text{A.7})$$

Here  $\omega$  is the angular frequency of the signal,  $\rho_0$  is the media density, and  $c$  is the speed of sound in air. The variables  $\eta$  and  $\eta_B$  refer to the shear and bulk viscosity, respectively. For simulations done in Chapter 4, values for  $\rho_0$  and  $c$  were calculated from the conditions found on the ISS via the Environmental and Thermal Operating Systems [55]. The viscosity parameters were estimated from air properties found in [61].

## APPENDIX B

### PATHFINDING ALGORITHM

Figure B.1 shows an example scenario that references the terms to be used in the derivation of the pathfinding algorithm for a single surface reflection.

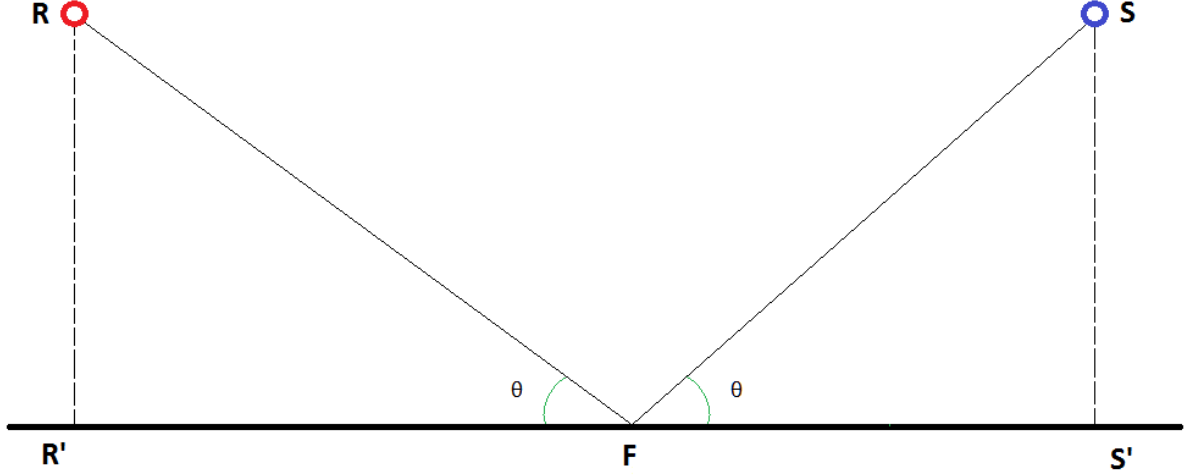


Figure B.1. Example reflection scenario with labels.

Let  $R$  and  $S$  represent the coordinates of a receiving sensor and the point source, respectively. These coordinates can be separated into their  $x$  and  $y$  components in a fashion such as  $R$  being composed of  $x_r$  and  $y_r$ .

$$R = (x_r, y_r), \tag{B.1a}$$

$$S = (x_s, y_s). \tag{B.1b}$$

Given a simple, infinitely long surface  $L$  that can be expressed by an equation such as

$$L_i = m_i x + b_i, \tag{B.2}$$

there are two points on  $L$  corresponding to the source and receiver that can be used to create two lines both perpendicular to the surface and parallel to each other. It is assumed

that the surface does not act as a barrier between the source and receiver as this would be a situation where refraction must be taken into account. Given no barrier condition and an infinite surface, there is only one point that the signal serve as a reflection point, and it is referred to as

$$F = (x_f, y_f). \quad (\text{B.3})$$

The reflected path will have the same angle  $\theta$  on both sides of the reflection point. Let  $R'$  and  $S'$  be defined as

$$R' = (x_{r'}, y_{r'}), \quad (\text{B.4a})$$

$$S' = (x_{s'}, y_{s'}) \quad (\text{B.4b})$$

and represent points where lines perpendicular to  $L$  intersects points  $R$  and  $S$ , respectively. This essentially forms two triangles  $\triangle SFS'$  and  $\triangle RFR'$  with the shared angle  $\theta$  and side lengths equivalent to  $\Delta(SS')$  and  $\Delta(RR')$ . To simplify expressions, the short hand form of the distance between any point  $A$  and  $B$  will be

$$\Delta(AB) = \sqrt{(x_A - x_B)^2 + (y_A - y_B)^2}. \quad (\text{B.5})$$

In addition, the known distances  $D(RR')$  and  $D(SS')$  will be further simplified to  $\Delta R$  and  $\Delta S$ , respectively.

Due to the similarity of angle  $\theta$  there is a relation between the triangles with reference to the reflection point. Expanding the distances forms including  $F$  and using the relation between the  $x_f$  and  $y_f$  defined by the surface's equation allows for the solving of only one variable. This can be seen in Equations B.6 - B.10 below.

$$\tan(\theta) = \frac{\Delta(RR')}{\Delta(FR')} = \frac{\Delta(SS')}{\Delta(FS')} \quad (\text{B.6})$$

$$\Delta R \cdot \Delta(FS') = \Delta S \cdot \Delta(FR') \quad (\text{B.7})$$

$$\Delta R^2 \cdot \Delta(FS')^2 = \Delta S^2 \cdot \Delta(FR')^2 \quad (\text{B.8})$$

$$\Delta R^2[(x_f - x_{s'})^2 + (y_f - y_{s'})^2] = \Delta S^2[(x_f - x_{r'})^2 + (y_f - y_{r'})^2] \quad (\text{B.9})$$

$$\Delta R^2[(x_f - x_{s'})^2 + (mx_f + b - y_{s'})^2] = \Delta S^2[(x_f - x_{r'})^2 + (mx_f + b - y_{r'})^2] \quad (\text{B.10})$$

Algebraic manipulation leads to a standard form of a quadratic equation as seen in Equations B.11 and B.12 below.

$$\begin{aligned} \Delta R^2[x_f^2(1 + m^2) + x_f(2mb - 2my_{s'} - 2x_{s'}) \underbrace{-2by_{s'} + b^2 + x_{s'}^2 + y_{s'}^2}_{C_1}] = \\ \Delta S^2[x_f^2(1 + m^2) + x_f(2mb - 2my_{r'} - 2x_{r'}) \underbrace{-2by_{r'} + b^2 + x_{r'}^2 + y_{r'}^2}_{C_2}] \end{aligned} \quad (\text{B.11})$$

$$\begin{aligned} x_f^2 \underbrace{[(\Delta R^2 - \Delta S^2)(1 + m^2)]}_a + \\ x_f \underbrace{2[\Delta R^2(mb - my_{s'} - x_{s'}) - \Delta S^2(mb - my_{r'} - x_{r'})]}_b + \\ \underbrace{[C_1 - C_2]}_c = 0 \end{aligned} \quad (\text{B.12})$$

This can be solved using the standard quadratic formula with bounds defined by source and receiver locations .

$$x_f = \frac{-b \pm \sqrt{b^2 - 4ac}}{2a} \left| R \notin \overline{FS}, S \notin \overline{FR} \right. \quad (\text{B.13})$$

Once  $x_f$  or  $y_f$  is found, the other component can be calculated using the Equation B.2. The reflected path distance can then be calculated from the two components from  $S \rightarrow F$  and  $F \rightarrow R$ .

$$d_f = \Delta(SF) + \Delta(FR) \quad (\text{B.14})$$

## **BIOGRAPHY OF THE AUTHOR**

Joel Matthew Castro is a candidate for the Doctor of Philosophy degree in Electrical and Computer Engineering from the University of Maine in May 2020.